ABSTRACT

Title of Document: SPECTROSCOPIC ENHANCEMENT FROM NOBLE METALLIC NANOPARTICLES

SHU-JU TSAI, Doctor of Philosophy, 2011

Directed By: Professor Raymond J. Phaneuf,
Department of Material Science and Engineering

Resonant coupling of localized surface plasmon resonances (LSPRs) in noble metallic nanostructures to incident radiation and the related subject of localized behavior of electromagnetic waves are currently of great interest due to their potential application to sensors, biochemical assays, optical transmission, and photovoltaic devices.

My thesis research is made up of two related parts. In part one I examined enhanced fluorescence in dye molecules in proximity to Ag nanostructures. In part two I studied the effect of Au nanostructure arrays on the performance of poly(3-hexylthiophene-2,5-diyl) : [6,6]-phenyl-C61-butyric acid methyl ester (P3HT:PCBM) bulk heterojunction (BHJ) organic solar cells (OSCs). Nanostructures were fabricated by two different methods: e-beam lithography (top down) and spray pyrolysis (bottom up). Using e-beam lithography, we produced

arrays of nanostructures with well defined shapes, sizes, and spacings. By systematically varying these topographical parameters, we measured their effect on nanometer-sized metallic structure-enhanced fluorescence (nMEF) and on absorption and external quantum efficiency (EQE) in OSC devices as a function of optical wavelength.

In analyzing experimental results, we carried out numerical simulations of the local electric field under incident light, across plasmonic resonances. The comparison between the calculated local field squared and measured fluorescence/EQE provides physical insight on the configuration- dependence of these two processes. Our results indicate that local field enhancement near nanostructures is dominant in nMEF, and that the local field is strongly affected by the substrate and device architectures. For the OSCs, both measurements and calculations show that absorbance within the active layer is enhanced only in a narrow band of wavelengths (~640-720 nm) where the active layer is not very absorbing for our prototype nanopillar-patterned devices. The peak enhancement for 180 nm wide Au nanopillars was approximately 60% at 675nm. The corresponding resonance involves both localized surface plasmon excitation and multiple reflections/diffraction within the cavity formed by the electrodes. Finally, we explore the role of the size of the nanostructures in such a device on the optical absorption in the OSC active layer. We find that small Au nanopillars produce strong internal absorption resulting in Joule heating, and suppressing the desired enhancement in EQE in OSC devices.

SPECTROSCOPIC ENHANCEMENT FROM NOBLE METTALIC NANOPARTICLES

By

SHU-JU TSAI

Dissertation submitted to the Faculty of the Graduate School of the
University of Maryland, College Park, in partial fulfillment
of the requirements for the degree of
Doctor of Philosophy
2011

Advisory Committee:

Professor Raymond J. Phaneuf, Chair
Professor John Melngailis
Professor Lourdes G. Salamanca-Riba
Professor Michael R. Zachariah
Professor Mohammad Al-Sheikhly

Acknowledgements

I would like to express my gratitude to my advisor Prof. Raymond J. Phaneuf for his fully support in completing this thesis. I gratefully thank Dr. Hung-Chih Kan for valuable guidance. I appreciate the support from our cooperators, Prof. Michael R. Zachariah and Dr. De-Hao Tsai for spray pyrolysis-synthesis of silver nanoparticles; J. Simpson and H. D. Drew for carrying out optical transmission measurements for our silver nanorod arrays. I also thank our cooperators, Dr. Warren Herman, Dr. Danilo Romero, and Dr. Mihaela Ballarotto, for helpful comments and for giving me the opportunity to use their facilities to fabricate and for characterize BHJ OPC devices. Thanks to Dr. Ben Palmer for allowing me access to the e-beam lithography system used in fabricating most of the nanostructures studied in this thesis. Thanks Dr. Daniel R. Hines for using his facilities, Nitrogen filled glovebox, and Dr. Michael Dreyer for assistance in Kelvin Probe Microscopy measurements. Particularly thanks to Dr. Dong Hun Park for providing me access and assistance in using a variable angle ellipsometry system and a spectrophotometer, and to Dr. Victor Yun for fabrication of shadow masks and assistance in testing my vacuum chamber. Thanks to John Sugrue and George Dearstine for fabricate the parts used in solar cell project. Thanks to Russell for assistance in substrate dicing and Aluminum polishing and Laurence C. Olver, Steven Brown, Patrick Sean, Warren Berk, George de la Vergne, and Scott Horst for helping me in the cleanroom. I am very grateful to my teammates, Dr. Tim Corrigan, Dr. Julia J. Heetderks, Dr. Shu-Hauh Guo, Dominic Britti, and Chih-Feng Wang, for helping me in lab and valuable discussing.

Table of Contents

Chapter 1: Introduction

1.1 Motivation

The size-dependent optical[1], catalytic[2], electronic[3], and magnetic[4], properties of nanoparticles, have driven research in many of fields of material science. One of the most active areas of nanoscience is based on nanoparticles enhanced spectroscopies, including surface enhanced Raman Scattering (SERS)[5], enhanced fluorescence,[6] and enhanced light absorption efficiency [7] with applications in chemosensors,[8] biosensors,[9] and photovoltaic devices, [10] respectively. The enhanced spectroscopies are based on resonant coupling between light and plasmons in noble metallic nanoparticles and possibility of tuning this resonance to coincide with that for excitation of nearby molecules. The plasmon resonance occurs when the frequency of the collective oscillation of the conduction band electrons in nanoparticles matches that of the incident light, resulting in strong local electric field near nanoparticles. The resonance wavelengths and local field distribution are determined by the shape, size, and composition of the particles, as well as the interparticle spacing and dielectric constant of the surrounding medium.[11-13] SERS has been well studied [14], SERS, fluorescence and electron-hole pair generation are all different, and thus the nature of interactions between nanoparticles and molecules in these three cases is not likely the same. In this work, we focus on the latter two.

To investigate the role of nanoparticles on enhanced fluorescence, we used e-beam lithography to create nanoparticle arrays systematically with various sizes and spacings in a combinatorial pattern. With transmission measurements or calculated extinction from numerical calculations (DDA), we can easily locate the plasmonic resonances of the systems. Using fluorescence microscopy, on the other hand, we can characterize the enhancement ratio for those configurations, and compare the results to find out how the plasmon resonance and local electric field resulting from the interaction between incident light and nanoparticles affect the enhanced fluorescence. In addition, from simulations carried out of with and without substrates, we characterized the influence of substrates.

On the other hand, e-beam lithography is generally not efficient for practical applications. We thus explored an alternative way to fabricate nanoparticles to optimize the system for fluorescencement for biosensor application. In our work, we use a spray pyrolysis method[15] combined with differential mobility analyzer (DMA)[16, 17] to synthesize size-selected spherical silver nanoparticles and investigate the role of the isotropic nanoparticles in the enhanced fluorescence.

Bulk-heterojunction (BHJ) organic photovoltaic (OPV) devices have been the focus of much recent work due to their potential in enabling affordable solar energy by a simple coating or a roll-to-roll printing process, their mechanical flexibility and the versatility of chemical structure from advances in organic chemistry.[18] The barrier for application of organic photovoltaic devices (OPV) is that their efficiency is unacceptable low. So far, the best commercial solar cells are silicon based with efficiency ~18%, while the OPV devices in the laboratory yield less than 10 %

efficiency.[19, 20] Significant efforts are concentrated on improving the efficiency of OPVs. One seemingly possible approach toward raising the efficiency of OPV's is to increase their absorption of solar radiation. In a BHJ polymer solar cell, the optimal thickness of the absorbing layer, however, is determined by a tradeoff: the absorber must be optically thick to absorb a significant fraction of the incident light but the thickness should not be large compared to the carrier collection length. This and other tradeoffs ultimately limit the maximum power conversion efficiency. Introducing noble metal nanoparticles (NP) and thus coupling of light to particle plasmons in thin film photovoltaic absorber layers is emerging as a potential method for enhancing their absorption. In this thesis, we present a systematic experimental and numerical study of the effect of periodic Au nanopillar arrays on absorption of poly(3-hexylthiophene) (P3HT) and [6,6]-phenyl C61 butyric acid methyl ester (PCBM) bulk heterojunction solar cells.

1.2 Background

1.2.1 Localized Surface Plasmon Resonance

Plasmons are the collective oscillation of free electrons in metal or semiconductor, and play an important role in the optical properties of metals. There are three base types of plasmon resonances: bulk (or volume) plasmons, surface plasmon, and localized surface plasmons (LSP). In this thesis work, we focus on the optical properties associated with localized surface plasmons.

The angular oscillating frequency of bulk plasmon in a free electron model ω_p is given by:

$$\omega_p = \sqrt{\frac{Ne^2}{m\varepsilon_0}} \tag{1.2.1}$$

, where N is the conduction electron density, e is the electron charge, m is the electron mass, and ε_0 is the permittivity of free space. Visible light is reflected from the metal surfaces because the frequency of light is lower than their plasmon frequency and make metals look shiny. The plasmon frequencies of copper (~2.1 eV) and gold (~2.5 eV) [21] are in the visible range, which gives them distinct colors. It is not possible to excite bulk plasmons of metals using visible light photons because of different nature of the two: Plasmons are longitudinal excitations, while photons are transverse, i.e. the fields oscillate parallel and perpendicular to the propagation vector, respectively. [22]

Surface plasmon polaritons are surface electromagnetic waves bound to the interface between a metal and dielectric interface, and travel along the interface.[23] The ε_m, or complex dielectric function of the metal is expressed as $\varepsilon_m = \varepsilon_m' + i\varepsilon_m''$, while in the visible frequency range the dielectric function of the surrounding medium only has essentially only a real part, ε_d. Surface plasmons occur at frequencies in which the real part of the dielectric constant of the metal and that of the dielectric have opposite signs. The surface plasmon frequency ω_{spp} can be determined by the bulk plasmon frequency and the dielectric constant of the dielectric ε_d [23].

$$\omega_{spp} = \frac{\omega_p}{\sqrt{1+\varepsilon_d}} \tag{1.2.2}$$

The real part of the wavevector of the surface plasmon polaritons k_{spp} can be expressed as

$$k_{spp} = k\sqrt{\frac{\varepsilon_m' \varepsilon_d}{\varepsilon_m' + \varepsilon_d}} \tag{1.2.3}$$

The wavevector of surface plasmon polaritons is always larger than that of the incident light for a metal. Thus a surface plamson can not directly couple on a flat metal surface to the incident light. The excitation of surface plasmon by light can be achieved by coupling of incident light with high dielectric medium such as prism [24, 25], with gratings [26], or with rough metallic surface [23], which make up the gaps in the dispersion relation for the excitation of surface plasmons.

Localized surface plasmons (LSP) are oscillations of the free electrons in small metallic structures; here small means the dimensions are much less than the wavelength of the light used to excite them. For small metallic nanoparticles, the collective oscillation of free electrons results in a polarization charge on the particle surface illustrated in figure 1.2.1. The polarizability of a spherical metallic nanoparticle in the presence of electric field can be obtained from Maxwell's equation with appropriate boundary conditions and is given by [27]

$$\alpha = 4\pi\varepsilon_0 R^3 \frac{\varepsilon_m - \varepsilon_d}{\varepsilon_m + 2\varepsilon_d}, \tag{1.2.4}$$

, where ε_0 is the permittivity of vacuum, and R is the radius of the spherical nanoparticle. When the denominator of the polarizability goes to zero (i.e. $\varepsilon_m' = -2\varepsilon_d$

and $\varepsilon_m'' = 0$), the polarizability diverges and a very strong interaction between the nanoparticle and the incident light occurs. In fact the dielectric function of nanoparticles and the surrounding medium both have real and imaginary parts, so even at resonance the denominator doesn't go to zero due to the presence of imaginary part of dielectric functions. Silver and gold are quite commonly used in plasmonic because the imaginary term of the dielectric constants is small at the optical frequencies we interested in, the visible and near infrared.

The excitation of LSP can result in strong absorption and scattering, and produce an intense near field that concentrates in small volume at the surface of nanoparticles. The sum of the absorption and the scattering is referred to as the extinction. It represents the total energy removed from the incident beam as measured by a detector in the forward direction due to presence of nanoparticles (figure 1.2.2). Mie presented a solution by solving the Maxwell's equations to describe the extinction spectra for free standing spherical metallic nanoparticles in a dielectric medium. Mie's solution is still used now because optical extinction is relatively easy to determine experimentally, by carrying out transmission measurements. For small particles ($x << 1$) , the absorption and scattering efficiencies are given by [27]

$$Q_{abs} = 4x \,\mathrm{Im}\left(\frac{\varepsilon_m - \varepsilon_d}{\varepsilon_m + 2\varepsilon_d} \right) \tag{1.2.5}$$

$$Q_{sca} = \frac{8}{3} x^4 \left| \frac{\varepsilon_m - \varepsilon_d}{\varepsilon_m + 2\varepsilon_d} \right|^2 \tag{1.2.6}$$

, where $x = 2\pi r\sqrt{\varepsilon_0}/\lambda$, and r is the radius of the spherical nanoparticle. The extinction cross section is given by $C_{ext} = Q_{ext} \times \pi r^2$. The absorption cross section is proportional to the particle volume and the scattering is proportional to the square of particle volume. Therefore, for smaller particle size, the extinction is dominated by absorption and the energy absorbed in metal can dissipate into heat.[28] Photo-induced heating has recently been applied in photothermal tumor ablation. [29] As particle size increase, the extinction dominated by scattering, the scattering efficiency increases [30]. Increasing the particle size, so that its dimensions are no longer much less than the wavelength of the exciting light wave results in higher order multi-pole modes being excited, which contribute to the scattering. Figure 1.2.3 shows the angular distributions (normalized) of the light scattered by a spherical Au nanoparticle with different radii plotted based on the solution of Mie's calculation. The outer and inner curves are the intensity of the scattered electric field, with nonpolarized incident light and polarized parallel to the incident plane, respectively. The arrows indicate the propagation direction of the incident light. As the particle size increases, the symmetry of the angular distribution of the scattering changes and more light is scattering in the forward direction. [31] Further increasing the particle size, that it is comparable or larger than the wavelength, results in most of the incident light is being reflected.

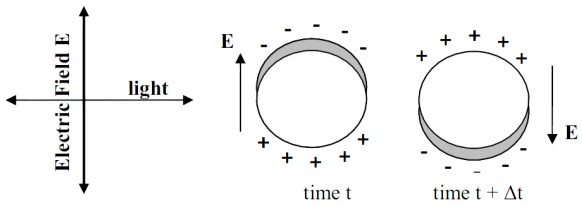

Figure 1.2.1 Schematic of the excitation of a dipole mode of a localized surface plasmon on a spherical metal nanoparticle by an incident electromagnetic field whose wavelength greatly exceeds the nanoparticle dimension. [22]

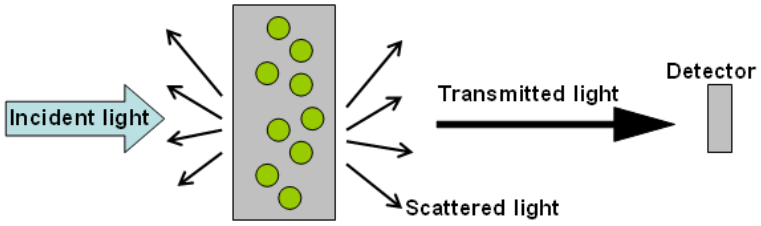

Figure 1.2.2 Illustration of extinction measurements.

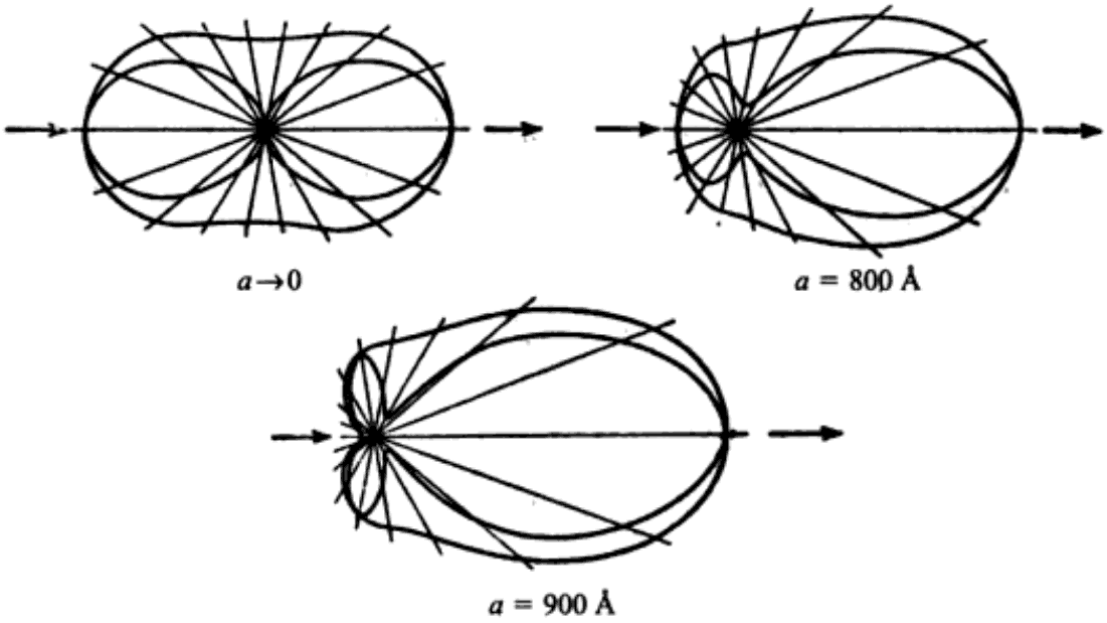

Figure 1.2.3 Angular distribution (normalized) of the light scattered by a spherical Au nanoparticle for the incident light polarized parallel to the incident plane (inner curves) and nonpolarized light (outer curves). The arrows indicate the direction of the incident light. (λ_0=550 nm, refractive index of the surrounding is 1.33, refractive index of Au is 0.27+2.45*i*). The figure is taken from [31].

Under optical illumination, the near field intensities and distribution depend strongly on the particle size, shape, interparticle spacing, and the architecture/ dielectric constants of the surrounding mediums. For example, due to image effects for a charge in front of the metallic film,[32] localized plasmons may couple to traveling plasmons in the presence of the metallic ground plane [33] which lies beneath the nanostructures.

The strong absorption, scattering, and intense near field produced by illumination of metallic nanostructures are important to the optical enhancements. The sizes and the spectra of these quantities are sensitive to many geometric and dielectric parameters [11, 12, 34], which makes it difficult to distinguish which quantities are most important to the optical enhancements.

1.2.2 Fluorescence

Fluorescence is a process in which the absorption of a photon by a molecule results in the emission of another photon with a longer wavelength, due to the Franck-Condon effect [35] which applies to changes in the vibrational levels of a molecule in the course of a change in electronic levels. Unlike the excited state in phosphorescence, in the excited singlet states for fluorescence, the electron in the excited orbital is paired by opposite spin to the second electron in the ground-state orbital. Consequently, return to the ground state is spin allowed and occurs rapidly by emission of a photon, with typical fluorescence lifetimes being nanoseconds.

1.2.3 Fluorescence Enhancement from Noble Metallic Nanoparticles

There have been a number of other studies of metal nanoparticle enhanced fluorescence. Geddes et. al.'s[9, 36, 37] and Gerber et. al.'s[38] work show that the coupling between fluorophores and the plasmon electrons is also important to enhanced fluorescence. The two groups model the origin of enhanced fluorescence, and reached similar conclusion: that the interactions between the excited fluorophores and nanoparticles change the fluorophores' radiative decay rate and, in turn, enhance fluorescence.

In these works, a common approach is to use optical extinction spectra from assemblies of nanoparticles to identify the LSP resonance conditions. As we mentioned above, however, the excitation of particle plasmon can result in enhanced absorption, scattering, and near field, and the individual contributions can not be distinguished by a simple extinction measurement. In addition, in this previous work, only small ranges of sizes and shapes of silver nanoparticles were investigated: approximately 30~80 nm in lateral diameter and 10 ~ 50 nm in height, with the shapes approximately about round disks. Therefore, the role of plasmonic excitation in the fluorescence has not been systematically investigated as yet; Important questions remaining are how do the size and the shape of the nanoparticles affect the enhancement of fluorescence. From our results with spherical silver nanoparticles[13], which we discuss in chapter 3, we find that their model is not complete: they neglected nanoparticles' responding to incident light and the spatial distribution of fluorophores. Further, the plasmonic contribution to the electric field distribution is not uniform near the surface of nanoparticle. As a result, fluorophores

at different locations will interact with plasmon electrons differently, which may result in different radiative decay rate. In fact, despite a good deal of study having been done in this area, it is not clear whether the incident light induced effect or coupling between fluorophores and nanoparticles dominates the total enhancement. How the radiative decay rate of fluorophores at different location is affected by the latter is also not clear yet. Finally, the role of the substrate in enhanced fluorescence has generally been neglected in previous work. Our results show, however, that the substrate has a significant effect.

1.2.4 Photovoltaics

A solar cell is a device that converts the energy of sunlight directly into electricity by the photovoltaic effect. There are several types of solar cells which have been developed so far, including inorganic solar cells such as those based on silicon, dye sensitized solar cells, and organic solar cells. From the chart shown in figure 1.2.4, the efficiencies of inorganic solar cells (10%~40%) are much higher compared to the organic types especially for the polymer based solar cells (<10%).[39]

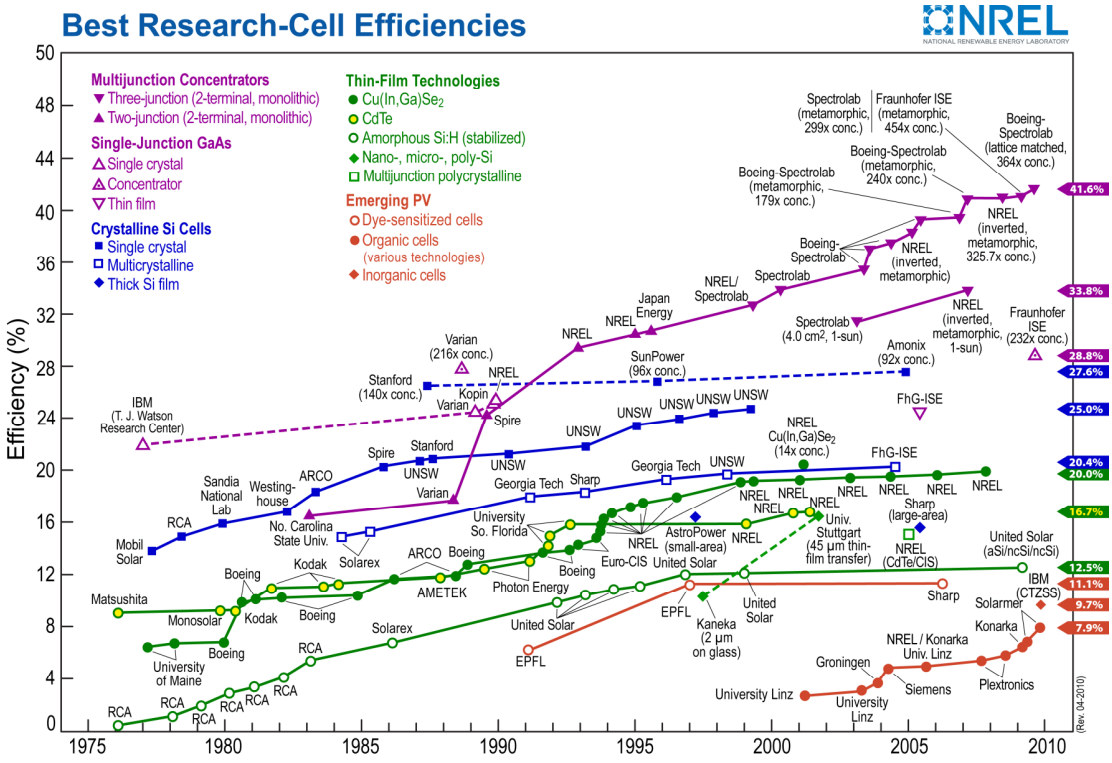

Figure 1.2.4 Solar cell efficiency chart taken from the web site of ObservatoryNANO. [39]

1.2.5 Basic Principles of Polymer Photovoltaics [40, 41]

The following brief discussion is based primarily on Mayer et al. and Blom et al.'s review [40, 41] . Polymer photovoltaics are comprised of conjugated polymers as electron donor and fullerene derivatives as electron acceptor materials. The active materials are sandwiched between a transparent conductor such as indium-tin-oxide (ITO) coated with Poly(3,4-ethylenedioxythiophene):poly(styrene sulfanate) (PEDOT:PSS) or fluorinated in oxide (FTO), and reflecting metal (usually Al or Ag). When operating the device, the donor material is illuminated with photon energy larger than the band gap energy. Electrons can be excited to lowest unoccupied molecular orbital (LUMO) by absorbed photons resulting in the formation of excitons (electron-hole pairs). Excitons can be efficiently dissociated at the interface between donor and acceptor. The resulting separated electrons and holes must be collected by the cathode and anode, respectively. The performance of a device can be described by the external quantum efficiency, which is the ratio of the number of free charge carriers to the number of incident photons. It can be expressed as

$$\text{EQE}(\lambda) = \frac{J/e}{I_{in}/h\upsilon} = \eta_A \times \eta_{ED} \times \eta_{CT} \times \eta_{CC}. \qquad (1.2.5.1)$$

, where J is photocurrent, e is charge of 1 electron, I_{in} is total power of incident light, $h\upsilon$ is energy of one photon, η_A is the efficiency of light absorption, η_{ED} is the efficiency of exciton diffusion toward a donor/acceptor interface, η_{CT} is the efficiency of exciton dissociation at such interface, and η_{CC} is the efficiency of charge carrier collection at electrodes (figure 1.2.5.1). In this thesis, we will focus on the first factor, i.e. η_A.

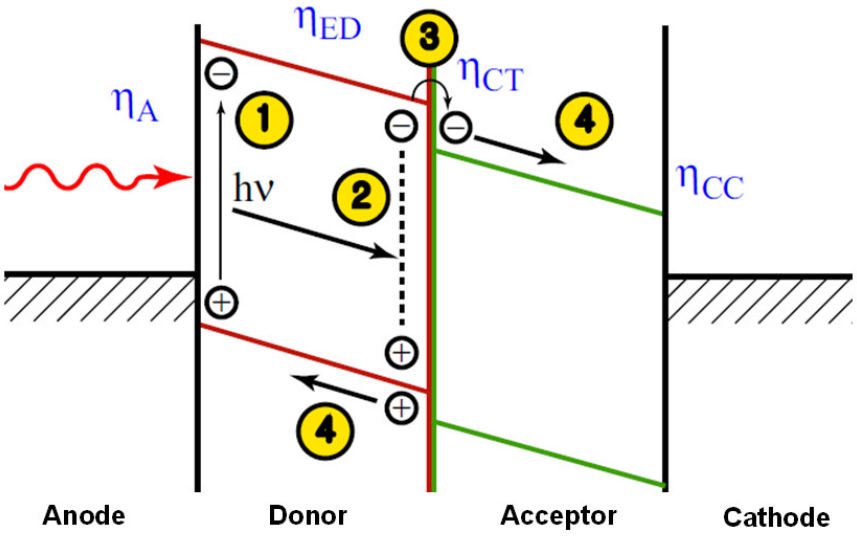

Figure 1.2.5.1 Schematic energy level diagram of a OPV device, and illustration of four steps of photocurrent generation in heterojunction PV cells. [42]

Common materials used in polymer photovoltaics are shown in figure 1.2.5.2. The charge carrier mobility and light absorption of conjugated polymers are important as a donor material in a polymer solar cell device, and correlated to the bands formed by sp^2-hybridized orbitals of carbon atoms. In conjugated polymers with chains of alternating single–double bond structure, the molecular p_z orbitals constituting the π-bonds actually overlap and spread over the entire molecule. When the donor materials is illuminated with a photon of energy larger than the "band gap" energy (the energy difference between highest occupied molecular orbital (HOMO) and the lowest unoccupied molecular orbital (LUMO)), these π electrons can be excited to donor LUMO (π -π* transitions) and form excitons (electron-hole pairs). The π–π* optical transitions are typically fall in the visible part of the spectrum, are strong (absorption

coefficients greater than10^5 cm^{-1}), and can be tuned through molecular design. The absorption spectra of conjugated polymers only cover a small region of the solar spectrum. For example, MDMO-PPV and P3HT have band gaps larger than 1.9 eV: their absorption spectra cover only 30 % of AM 1.5 solar radiation. To achieve a power conversion efficiency of polymer solar cell 11 %, a band gap of 1.1 eV is required to absorb 77% of the AM 1.5 solar photo flux. [40, 41] In addition, the charge-carrier mobilities of most polymers are low (usually in the range of 10^{-7}–10^{-3} cm^2/V.s), thus the thickness of the active layer must be limited to ~ 100 nm. However, at this thickness only ~ 60 % of light at absorption peak can be absorbed without back reflection of electrode.

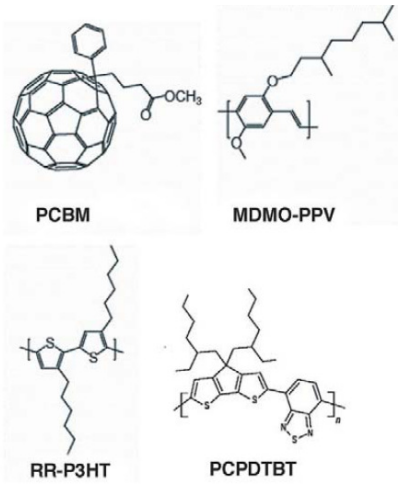

Fig. 1.2.5.2 Common materials used in polymer photovoltaics. From left to right, PCBM: (6,6)-phenyl-C61-butyric acid methyl ester; MDMO-PPV: poly(2-methoxy-5-(3',7'-dimethyloctyloxy)-1,4-phenylene-vinylene); RR-P3HT: regioregular poly(3 hexylthiophene); PCPDTBT: poly[2,6-(4,4-bis-(2-ethylhexyl)-4H-cyclopenta[2,1-b;3,4-b´]-dithiophene)-alt-4,7-(2,1,3-benzothiadiazole)].[40]

The excitons in organic photovoltaics are strongly bound, with an energy between 0.1 and 1.4 eV [43-45] which is much larger than in inorganic materials (~ 10^{-6} eV). The larger binding energy is because the electronic wavefunctions in organic molecules are more localized, and electrostatic attraction can thus keep the electron and hole together. Because of the high exciton binding energy in conjugated polymers, thermal energy at room temperature is not sufficient to dissociate the excitons into free charge carriers. The highly bound exciton in organic solar cell leads to significantly differences in the configuration and operation principle of photovoltaic devices between organic PV devices and inorganic PV devices. To separate bound excitons in organic solar cells, it must migrate to an interface betweeb donor and acceptor materials, where there is a sufficient chemical potential energy drop.

The exciton diffusion length L_D, which characterizes the effective width of the active area of the polymer at the acceptor interface, in various conjugated polymers has been reported in the literature to range from 5 to 20 nm.[46-49] Because it is considerably less than the photon absorption length (~100 nm), the efficiency of a bilayer cell is limited by the number of photons that can be absorbed within the effective exciton diffusion range at the polymer/ electron acceptor interface. To solve the problem of limited exciton diffusion length in conjugated polymers for a bilayer PPV device (figure 1.2.5.3 (a)), the bulk heterojunction PV cell architecture (figure 1.2.5.3 (b)) has been developed by simply blending the polymer with a soluble electron acceptor. In a BHJ, the electron donor and acceptor materials are blended together and cast as a mixture that then phase-separates. The domains of donor and

acceptor materials in the device are ideally separated by only several nanometers, a distance optimized for carrier diffusion. In such a case nearly all excitons can be formed within the diffusion distance from a donor/acceptor interface. The interpenetrating donor:acceptor network allows photon absorption improvement by a simple increase of the active-layer thickness, to ~ 100 nm. The carrier mobility plays an important role on further increase the active layer thickness. The mobility of the active layer can be improved by ordering the donor and acceptor materials as shown in figure 1.2.5.3 (c). Although BHJ PPV devices have a significant improvement compared to bilayer designs, BHJs require carefully control over materials morphology on the nanoscale. A great number of variables can affect the BHJ structure and thus affect the exciton diffution length and carrier mobility including choice of donor and acceptor molecules, the annealing parameters [19], solvents [19], and the donor-acceptor weight ratio. The relatively large number of such factors make it difficult to optimize BHJ PPV devices.

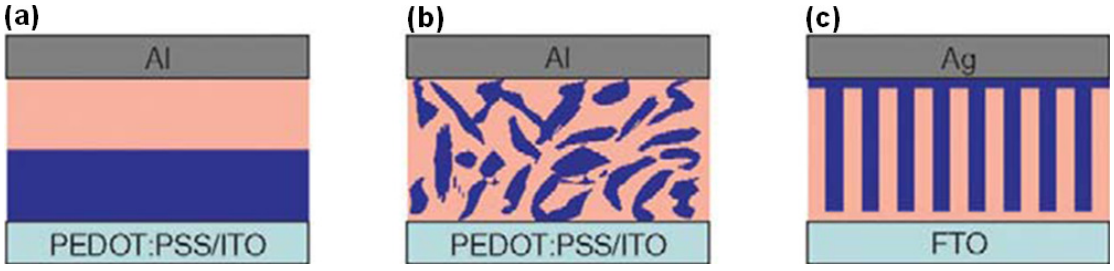

Fig. 1.2.5.3 Architectures of (a) A bilayer HJ, (b) a bulk HJ, and (c) an ordered HJ PPV device.[40]

After dissociation, each charge carrier must be transported through the device to the appropriate contact while avoiding traps and recombination. After dissociation has taken place, the electron and hole may still be Coulombically bound (called a *geminate pair*) and must be dissociated by an internal field ($E = (V_{oc}-V)/L$, where V_{oc} is open circuit voltage, V is external bias, and L is the thickness of the active layer) [41]. Besides, charge carrier mobility now begins to play a major role: the mobility should be high enough and balance to avoid recombining at trap sites and to prevent the build up of space charge which can hinder further extraction of charge carriers or remain in the device as undesirable space charges that oppose the drift of new carriers. Simple calculations show that mobilities should be 10^{-4} $cm^2/V{\cdot}s$ or higher for efficient geminate separation[50]. This process also imposes geometric restrictions. Highly folded, disordered geometries should lead to lower probabilities of geminate pair separation. Consequently, ordered nanostructures are ideal for splitting geminate pairs. Mobilities should be high enough to extract carriers as they are transported through the device before they undergo recombination, but not so high that the diffusive dark current limits V_{oc}. While still under study, mobilities of 10^{-4}–10^{-2} $cm^2/V{\cdot}s$ are probably optimal for device thicknesses of 200–500 nm. Higher mobilities will require changes in device design to minimize dark current. Similar variables need to be considered for the exciton dissociation efficiency; these variables however, can affect the carrier mobility and sometime there is a trade off between the two: an annealing process can increase the crystalline and domain size of the polymer resulting in increase the mobility, however, the increasing of domain size increases the required distance for the exciton to migrate to the interface.

The appropriate contacts in PPV devices are also a key parameter to determine their ultimate performance. The work functions of the metals, the interface dipole at the surface of metal, and induced at the interface of metal and organic are the factors that determine the carrier collection efficiency (η_{cc}). For conventional BHJ PPV devices, a ~ 40 nm thick PEDOT:PSS layer is coated on the anode surface (such as ITO) to reduce the hole injection barrier and thus increase the overall efficiency of the device. Our experiment results presented in chapter 5 show that the power conversion efficiency is reduced from approximately 2 % to 0.12 % with this interface layer being absent. Presently used interface materials, might need to be replaced to construct better architecture for optimization of light absorption. A thinner interface layer (~ 1 nm) fabricated by the self assembled monolayer method [51] or by the plasma polymerization method [52-54] might be used to fabricate thinner interface layer to optimize the absorption of the devices.

1.2.6 General Considerations to Improve the Efficiency of Polymer Solar Cells

A great deal of effort has been made to raise the efficiency of OPV, including optimizing the active layer thickness to trade-off enough light absorption and reasonable charge carrier extraction,[18] introducing of the bulk heterojunction concept [55] consisting of an interpenertrating network of electron donor and acceptor materials, searching optimized absorption polymer with highest electronic

mobility, and adjusting the composition, morphology, and ratio of donor/acceptor materials.[19, 56] To raise the efficiency of an OPV, solar radiation must be effectively absorbed. Applying noble metal nanoparticles in enhancing efficiency of BHJ OPV is an emerging field and little systematical research has been done by comparison to that done for silicon based OPVs, described briefly below.

1.2.7 Enhancement of Silicon Photovoltaic Devices by Using Noble Metallic Nanoparticles

Several experiments and/or calculations have been done to explore the effect of Au and Ag nanoparticles in inorganic solar cells, especially silicon based solar cells.[10, 57-64] The main mechanisms that contribute to the photocurrent enhancement are light scattering [61, 63, 65], coupling of LSP with waveguide mode in silicon-on insulator (SOI) solar cells, [30, 65, 66] and high near-fields around the noble metallic nanoparticles [66]. The dielectric properties of organic materials and that of silicon, however, are different: silicon usually is treated as a lossless material[61, 63] while organic materials used in OPV devices have some peaks of absorption coefficient that are much larger than the absorption coefficient of silicon. Besides, silicon has higher refractive index than organic materials. Calculated electric field intensity, ($|E|^2$) distributions (figure 1.2.7.1) show that when the Ag nanoparticles are placed on a silicon substrate, they tend to sweep the electromagnetic field into the underlying silicon. By comparison less field is swept into a silica substrate whose refractive index (n ~ 1.5 at 514 nm radiation) is much smaller than that of silicon (n ~ 4.2 at 514 nm radiation). The higher refractive index for the

silicon also benefits by forming waveguide structure, which allows more light to be trapped in the silicon by exciting a waveguide mode due to excitation of a localized surface plasmon. We thus anticipate that the plasmonic characteristics of noble metal nanoparticles in organic OPV will be different from those in silicon PV systems.

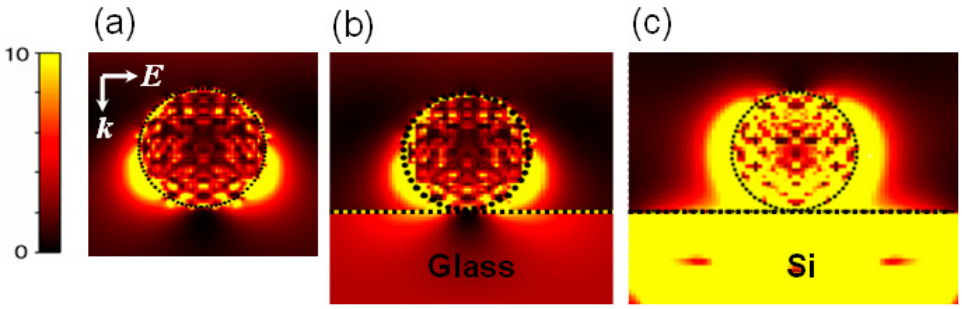

Figure 1.2.7.1 Calculated electric field intensity (E^2) distributions in cross sectional view for a silver nanoparticle in water. Panel (a) free standing, (b) on a SiO_2 substrate, (c) and on a silicon substrate. The particle diameter is 120 nm. As shown in panel (a), the incident light propagates downward and the polarization of the E-field is parallel to the substrate. The wavelength of the incident light is 388 nm wavelength (514 nm in air). The color table indicates the field intensity normalized to the incident light intensity. (From ref. [13]).

1.2.8 Enhancement of Polymer Photovoltaic Devices by Using Noble Metallic Nanoparticles

For organic solar cells, most reports to date are of simple absorption (without the presence of electrodes or full materials) and external quantum efficiency (EQE) measurement.[67-74] However, the absorption spectrum of a working device is expected to be considerably different in the presence of electrodes, due to reflectance at the interfaces and interference effects. It is thus not possible to extract the absorption of the active layer experimentally in a functional device. In addition, in previous reports [67-70, 72-75] the configurations of the nanoparticles were not well defined, making it difficult to identify the role of particle plasmon excitation, and to weight the magnitudes of absorption, scattering, and near field. Cole and Halas[7] carried out extinction calculations to determine a distribution of silica/Au nanoshell particles that have an optimal optical cross section to optimize the absorption of solar radiation. These authors assumed that increasing the extinction due to excitation of LSP should produce an increase in the absorption in nanoparticles or increase the forward scattering or near field, and thus give rise the solar cell efficiency.[7, 67, 71, 73, 74] In contrast, while Mofa et. al. [69] observed increased power conversion efficiency from 1.3% to 2.2% due to incorporation of silver nanoparticle in BHJ solar cell (ITO/Ag nanoparticles/PEDOT:PSS/ P3HT:PCBM/Al), the Ag samples exhibited a decrease in external quantum efficiency at 450 nm incident radiation, which coincides with the peak of extinction spectra. There have been other literature reports that an increase in extinction due to excitation of particle plasmon, which it can increase the absorption in nanoparticles, suggest the energy of the absorption in

nanoparticle can be translated to heat. [28, 29, 65, 76, 77] In fact it is not clear that increase in optical extinction should give rise to an increase the photocurrent generation. Based on our finding in enhanced fluorescence, however, extinction is not the only factor for the optical enhancements at play. Our results indicate that the local field might be even more important for the enhanced efficiency.[13] A direct comparison of measured and calculated[78] optical spectral response for a well defined metallic nanoparticle configuration in a bulk heterojunction OPV has not as yet been fully carried out. In this thesis, we present a systematic experimental and numerical study of the effect of periodic Au nanopillar arrays on absorption of poly(3-hexylthiophene) (P3HT) and [6,6]-phenyl C61 butyric acid methyl ester (PCBM) bulk heterojunction solar cells [19], in which we add nanoparticle arrays. As described in chapters 4 and 5, we carried out the numerical calculations, extinction measurements, and photocurrent spectroscopy to understand the role of plasmon resonance and local field in this extremely important device.

1.3 Organization

The remainder of this thesis is organized as follows: in chapter 2 we describe the experimental techniques used in fabricating and characterizing our arrays of silver nanoparticles and the fluorescent molecules in our studies of enhanced fluorescence.

In chapter 3 we describe a series of experiments in which we measured the dependence of the fluorescence from molecules proximal to different silver nanostructures, and in parameter on the role of the size, shape and spacing of the particles, as well as the nature of the substrate. We begin this chapter with results for anisotropic, rod-shaped columns consisting of both extinction and fluorescence measurements to determine the incident light-polarization dependence of fluorescence on the rods' width-to-length aspect ratio. We discuss the limitations of a simple model based only on resonant Plasmon coupling in light of these results. We next describe results for size-selected spherical nanoparticles, in which we compared the fluorescence with measurements of the optical extinction [13] and calculations of the local fields carried out by DDA.

In chapter 4 we describe the experimental techniques used in fabricating and characterizing our arrays of Au nanopillars and BHJ polymer solar cell devices.

In chapter 5 we report the results of an systematically vary the architecture of the design to obtain the optimization of energy conversion efficiency and the results of the extinction measurements and the numerical calculations (FDTD) to identify the plasmon resonance and local field distribution to see how the two quantities related to the performance of solar cells.

Chapter 6 gives some overall conclusions from this work and suggestions for future work. Additional details on the calculations and measurements are given in a series of appendices.

Chapter 2: Experimental Methods for Fluorescence Enhancement Using Nanoparticles

2.1 Metallic Nanostructure Fabrication

2.1.1 Electron-Beam Lithography

To understand the role of nanoparticles on enhanced fluorescence, we used e-beam lighography to systematically create nanoparticle arrays with various sizes and spacings in a combinational pattern on different substrates. The procedures are indicated schematically in figure 2.1.1. In most of our studies we used Si (001) substrates ($1\sim10\ \Omega-cm$). We first deposited approximately 25nm of an aluminum oxide (Al_2O_x) onto these substrates to improve the adhesion of the silver nanoparticles, as Ag does not wet SiO_2. We next spun polymethyl methacrylate (950,000 molecular weight, 4% resins in anisole solvent) onto the substrates, and then patterned this layer using a field emission scanning electron microscope (SEM, JEOL JSM-6500F), which has been modified for electron beam lithography control (Nabitty). A silver layer, typically 75nm thick, was deposited using an electron beam evaporator (CHA Mark 40). After this, the part of the silver layer coating the resist was removed by a lift-off procedure.

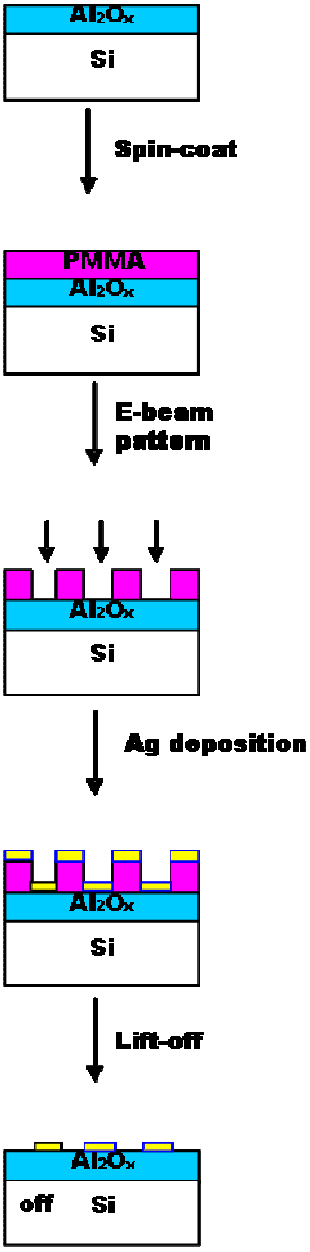

Figure 2.1.1 Schematic of electron beam lithography procedures for producing Ag nanostructures on an aluminum oxide coated silicon substrate.

2.1.2 Spray Pyrolysis Synthesis

The e-beam lithography is generally too slow and costly for practical applications. We thus explored alternative method to fabricate nanoparticles quickly and demonstrate the optimization of enhance fluorescence on this system for biosensor application. We use a spray pyrolysis method[15] combined with differential mobility analyzer (DMA)[16, 17] to synthesize size-selected spherical silver nanoparticles pyrolysis as shown schematically in Fig. 2.1.2.

Aerosol particles were produced by passing a carrier gas through an oven in which Ag is heated to 1100-1200 ^{0}C resulting in evaporation and condensation. These were then charged and passed through a differential mobility analyzer (DMA) for size-selection. Next the aerosol passed through second furnace, in which the particles were sintered in hydrogen to make them spherical. These spherical, size-selected particles were directed onto a Si (001) substrate. The substrate was pre-patterned with crossed silver lines that allow us to navigate back to the same region for different techniques, specifically for scanning electronic microscopy (SEM) and Laser scanning fluorescence microscopy (LSM).

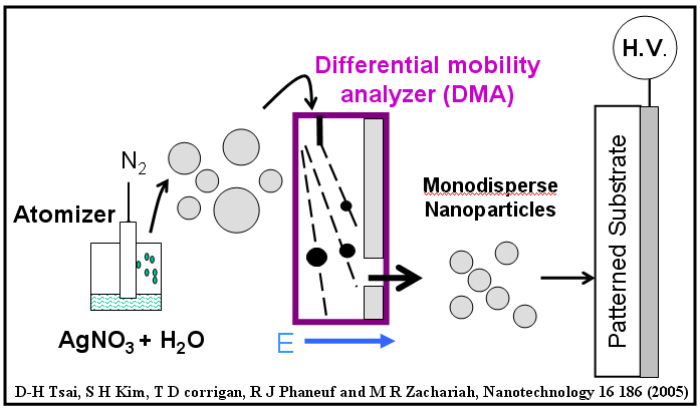

Figure 2.1.2 Schematic of synthesis of size selected spherical silver nanoparticle.

2.2 *Scanning Electron Microscopy Characterization*

In addition to atomic force microscopy (AFM), we used scanning electron microscopy (SEM, LEO 1550 VP) to characterize the sample topography after each fabrication step. While AFM provides superior information as to feature height, SEM allows us to more precisely define the lateral dimensions of the structures, as the AFM tip is wedge shaped, and produces a convolution effect which depends on the height or depth of a feature.

2.3 *Coating Sample with Fluorescent Molecules*

We coated samples with fluorescent molecules by a two-step self-assembled monolayer (SAM) method. We deposited a combination of proteins layers - BSA-bt and then Streptavidin labeled by both Cy3 and Cy5 fluorophores onto samples. Each is deposited from solution. BSA-bt solution consisted of 1 μM BSA-bt in buffer solution (5mM solution of mixture of $NaH_2PO_4 \cdot H_2O$ and $Na_2HPO_4 \cdot 7H_2O$ with the pH

adjusted to 7.5). There are two functions of BSA-bt in our system: as a link between surface of samples and streptavidins and as a spacing layer to prevent the fluorescence quenching which is believed to occur at small separations. The dye solution consisted of 0.5 µM Cy3 and 0.5 µM Cy5 solution in the same buffer solution. We first deposited BSA-bt on the sample and wait for 1 hr, we then rinsed away the BSA-bt using a buffer solution. Next, we put fluorescently labeled streptavidin solution onto the sample. Finally we rinsed away that fluorophore-tagged protein which was not bound to underlying BSA-biotin. Applying both dyes simultaneously eliminated variation in sample preparation and allowed the same areas to be evaluated using two spectral windows. Figure 2.3 is a schematic of the coated sample, in which the fluorophores are located approximately 8 nm above the sample surface.

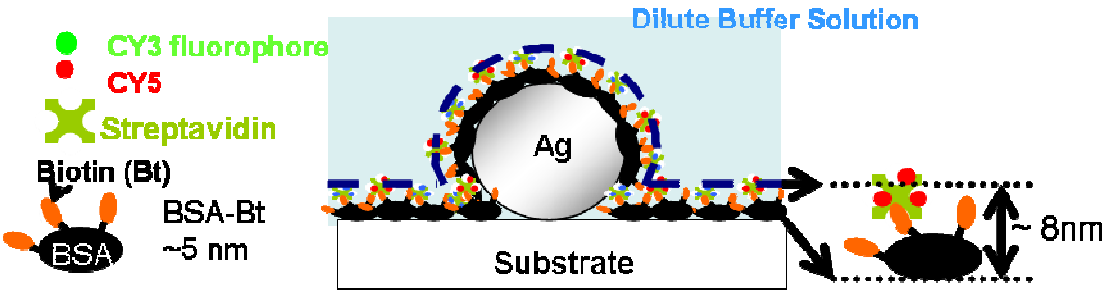

Figure 2.3 Schematic illustrating coating fluorophores onto Ag nanoparticles on substrate.

2.4 Fluorescence Measurements

We use a confocal laser scanning fluorescence microscope (Zeiss model LSM 410) with sample surface moisturized with a layer of dilute buffer solution to measure the intensity of fluorescence. The absorption and emission spectra of the CY3 and CY5 fluorophores and excitation wavelengths are plotted in figure 2.4.1. CY3 was efficiently excited by linear polarized light using the 514 nm line of an Argon ion laser, and the fluorescence collected through a filter which passes light in the wavelength range from 535 to 575nm. For CY5 the 633 nm line of a He-Ne laser was used for efficient excitation, and the fluorescence collected through a filter passing light of wavelength above 660nm. The measurement scheme is shown in figure 2.4.2

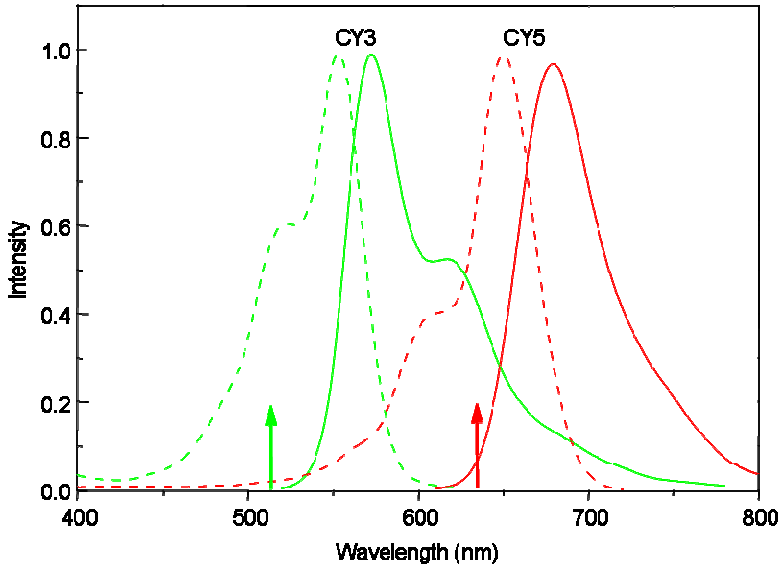

Figure 2.4.1: Absorption (dash) and emission (solid) spectra of CY3 (green) and CY5 (red); Laser lines used for excitation are shown with arrows: 514 nm (green) and 633 nm (red).

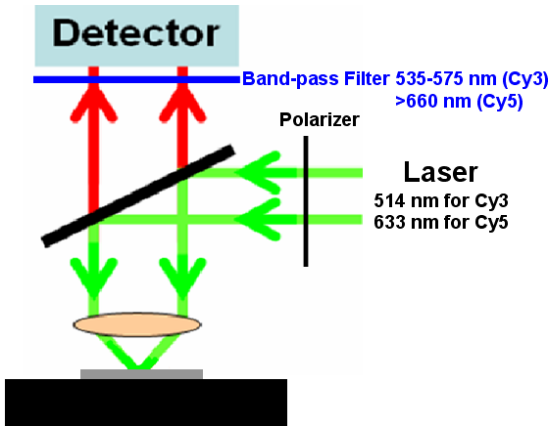

Figure 2.4.2 Schematic of laser scanning fluorescence microscopy measurement.

2.5 *Characterization of the Fluorescence Enhancement Ratio*

We developed a quantitative analysis of the fluorescence enhancement for Cy3 and Cy5 fluorophores from the silver nanoparticles. We define the enhancement ratio to be $N = \frac{I_a - I_B}{I_f - I_B}$, with $I_a = \frac{I_e - (1 - A_a) \cdot I_f}{A_a}$, where I_a is the average fluorescent intensity normalized with the percentage areal coverage A_a of the silver nanoparticles, measured using SEM. I_e is the raw fluorescent intensity measured from areas containing fluorophore/spacer coated silver nanoparticles. I_f is the fluorescent intensity without silver nanoparticles, i.e. measured from areas where only fluorophore/spacer layer is present. I_B is the background intensity measured from regions of the sample scraped so that both fluorophore and silver nanoparticles are absent. *N* basically describes the fluorescence enhancement from the area covered by the silver nanoparticles. Measuring a ratio allows us to factor out the effect of variations in fluorophore coverage.

2.6 Extinction Measurements[79]

To determine particle plasmon resonance frequencies for arrays of nanoparticle with varied size and shape we measured optical transmission spectra, in which the plasmon resonances appear as minima in the transmission spectrum, or as peaks in the extinction spectrum, as illustrated in Fig. 2.6.1.

These measurements require optically transparent substrates; we used commercial glass slides which are coated with a thin (15-30 nm), transparent indium tin oxide (ITO) layer. This conducting layer serves to prevent charge buildup during lithography, and improve adhesion of silver nanoparticles. For optical transmission measurements, metal (brass) masks provided an aperture over the silver nanoparticle array and over the bare substrate. Room-temperature transmission measurements of near-normal incident light at energies from 1 to 3 eV were performed using a Fourier-transform spectrometer. Comparing results with different polarizations of excitation light, we explore the role of the plasmon resonance coupling in fluorescence enhancement.

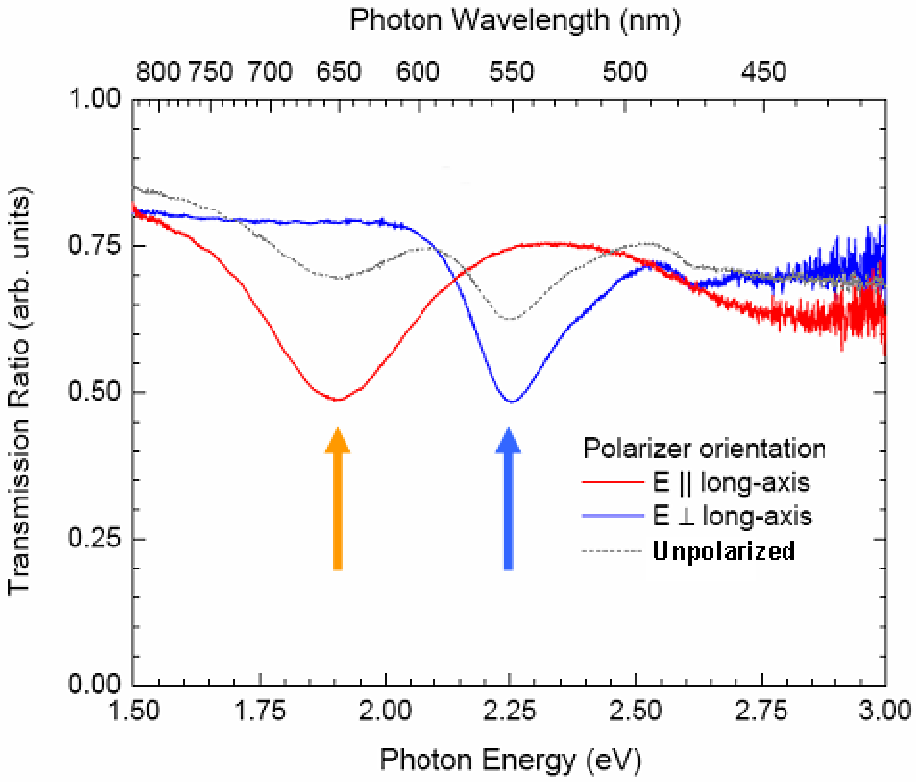

Figure 2.6.1 Transmission spectra measured for an array of rod-shaped Ag nanoparticles of lateral aspect ratio 2:1 deposited on ITO-coated glass. The red curve is for the electric field vector of the incident light parallel to the long axes of the rods; the blue curve is for the electric field vector perpendicular to the long axis of the nanoparticles.[79]

2.7 *Numerical Calculations*

We simulated the interaction between incident light (wavelength 514 nm for Cy3 fluorophores and 633 nm for Cy5) and noble metallic nanoparticles with various shape, size, interparticle spacing, dielectric constant of surrounding and the interaction between fuorophores and nanoparticles based on Discrete Dipole Approximation (DDA).[80] DDA was used to compute the extinction (scattering and absorption) cross sections and the local field for a single nanoparticle or limited number of particle arrays (due to the limitation of DDA) on a finite substrate. Furthermore, DDA provided us with the resultant spatial dipole distribution. In addition to the local field intensity distribution, it also allows evaluation the dipole moment of a nanostructure immersed in an electromagnetic field. Details for DDA methods are presented in Appendix A.

Chapter 3: Experimental and Numerical Results and Discussions for Fluorescence Enhancement Using Silver Nanoparticles

In this Chapter we present examples of results in which we have demonstrated fluorescence enhancement from a few × 10 to a few × 100 fold using both anisotropic and isotropic silver nanoparticles fabricated by e-beam lithography and a spray pyrolysis method, respectively. As discussed below the extinction measurement and calculated E-field distribution, both of the two set experiments show that near field is important in the enhanced fluorescence. Some of the results presented have been published elsewhere [13].

3.1 Enhancement from Anisotropic Silver Nanoparticles [79]

To explore the role of particle shape and the polarization of the incident light in enhanced fluorescence, we fabricated silver nanorod arrays on an ITO-coated glass substrates. We measured fluorescence for two fluorophores, Cy3 and Cy5, using on the samples pre-coated with these fluorophores, as described above. Figure 3.1.1 shows fluorescence images and summary plots of the enhancement for each of the two fluorophores and for polarization of incident light both parallel and perpendicular to the long axes. The results show a strong polarization and shape dependence of the enhanced fluorescence. For light polarization parallel to the long axis as shown in Figure 3.1.2(a) and (b), the optimum enhancement shifts slightly to larger particle

size for longer wavelength, which qualitatively agrees with the predicted red shift of the plasmon resonance for larger particle length/width ratio.[11] For the incident light polarization perpendicular to the long axis, however as shown in Figure 3.1.2 (c) and (d), the peak still shifts to larger particle size for longer wavelength, which is opposite to the predicted blue shift in the transverse plasmon resonance.[11] To test this prediction, we carried out the extinction measurements in collaboration with J. Simpson and H. D. Drew.[79] Figure 3.1.3 shows the wavelengths of the measured extinction peak versus aspect ratios for incident light parallel (orange) and perpendicular (blue) to the long axis. The extinction peaks (open circle) indeed shift toward red and blue with increasing aspect ratio for polarization of incident light parallel and perpendicular to the long axes, respectively; thus the extinction measurements are consistent with the theory of plasmon resonance.[11] Comparison with maxima in the fluorescence, however, shows that only half of the four cases reside within the bands formed by the peaks in absorption and reemission (Cy3 in short axis and Cy5 in long axis). The detailed dependence of the fluorescence enhancement we observe on anisotropic silver nanoparticles can thus not be fully explained by the simplest model of resonant plasmon coupling.

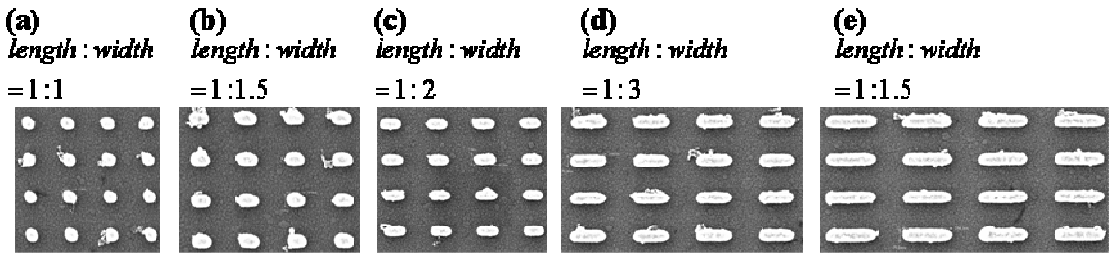

Figure 3.1.1 SEM images of nanorod silver nanoparticle arrays on an ITO-coated glass substrate fabricated by e-beam lithography. The height of particles are ~ 75 nm and lateral size is 75 nm x 75 nm for aspect ratio (length/width ratio) 1 particle. (a) to (e) are aspect ratios 1 to 4. The edge to edge spacing is 150 nm for all cases.

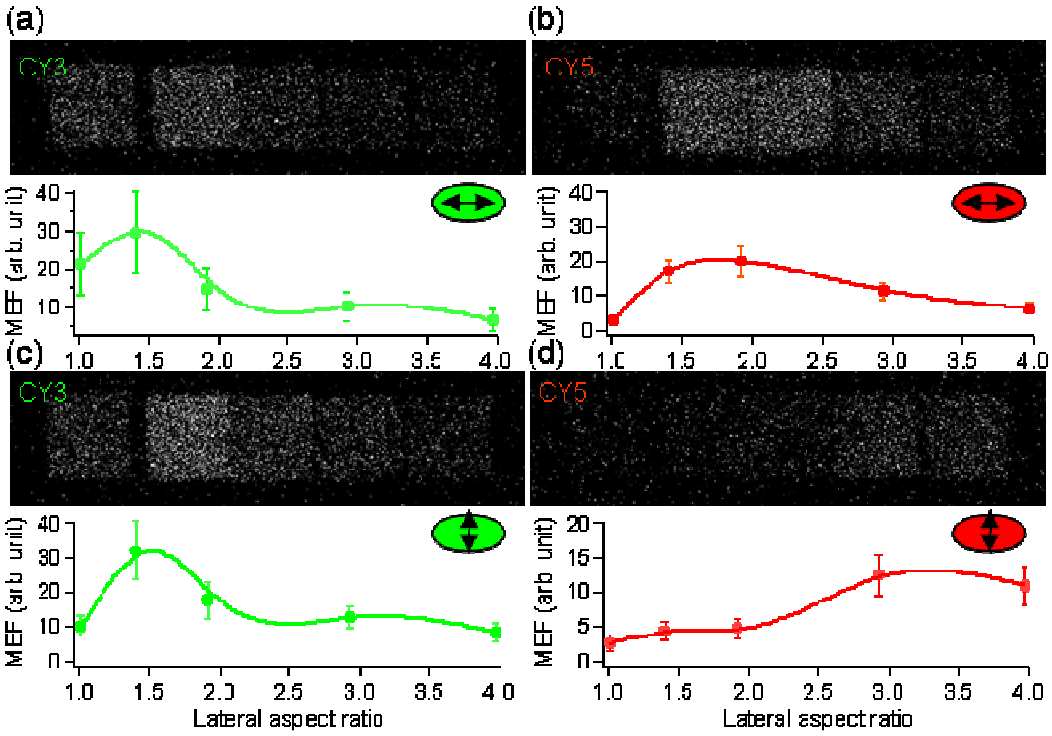

Figure 3.1.2 Plots of enhanced fluorescence for Cy3 (green) and Cy5 (red) and two polarizations of laser: (a) and (b) parallel to long axis; (c) and (d) perpendicular to short axis.

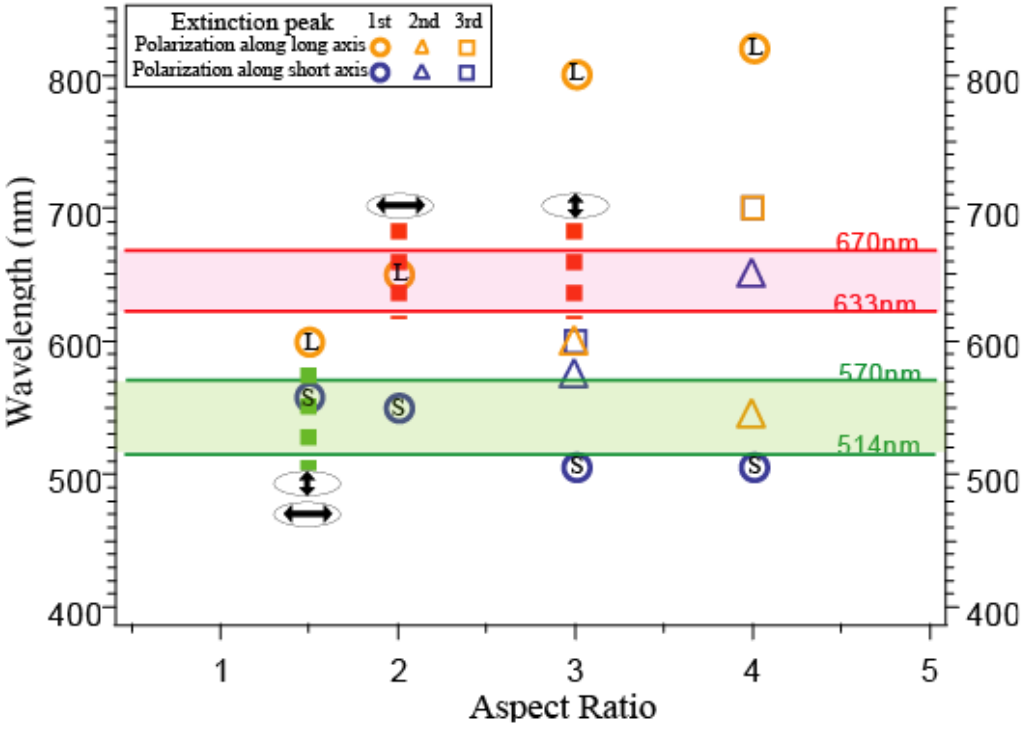

Figure 3.1.3 Comparison of measured peaks of extinction (orange and blue) and aspect ratios producing maximum fluorescence (green and red) plotted as function of length/width ratio.

3.2 Enhancement from Isotropic Silver Nanoparticles [13]

Figure 3.2.1 shows a comparison between scanning electron microscopy and fluorescence microscopy images from size-selected silver nanoparticles on a silicon substrate for the range of diameters we have studied; in Fig. 3.2.1(a) – (e) the SEM images are shown in red, and fluorescence images for an excitation wavelength of 514 nm (exciting the Cy3 fluorophore), scanned from precisely the same regions are superposed in green. The SEM images show that particles are spherical, and randomly distributed. There are rare occasions where two or more particles are in contact; this occurs more frequently on samples with larger average particle diameter, as shown in Fig. 3.2.1(e). In general, however, individual particles are well separated from their neighbors. The images show a strong and systematic variation as the average diameter of the Ag nanoparticles is varied. Highest fluorescence intensities are obtained from samples with particle diameters slightly below the middle of range we have studied, i.e. for d ~ 90 nm. A similar trend, but with a slight increase in the optimum diameter is also observed from fluorescent images for an excitation wavelength of 633 nm, as discussed below.

The fluorescence images also show variation of the intensity from point to point within an image; this is apparently due to variation in the coverage of the tagged protein, as we find that this variation remains fixed when additional images of the same region are scanned, and many of the bright regions occur between relatively well separated Ag nanoparticles. There are no extremely intense "hot spots" between particles in near – contact[81] or in agglomeration; however there is a correlation between local coverage for certain particle sizes, as seen in Fig. 3.2.1(g)

and (i) where the local fluorescence intensity varies linearly with local Ag nanoparticle coverage within a sample. For other particle sizes the intensity and coverage are nearly independent. Interestingly, it is for those particle sizes corresponding to highest fluorescent intensities that a strong correlation exists.

Fig. 3.2.2 shows the measured nanoparticle diameter dependence. As shown in panel 3.2.2(a), the enhancement initially increases with particle diameter, reaching a maximum of approximately 240 at d ~ 85 nm for the 514 nm wavelength excitation; we observe a window of particle diameters between ~85 nm and ~150 nm for which the enhancement exceeds 100 fold. For excitation at a wavelength of 633 nm, the maximum enhancement of approximately 350 is measured at a slightly larger diameter, ~150 nm, as seen in panel 3.2.2 (b); the enhancement exceeds 100 for diameters from ~95 nm to ~160 nm. Much lower or no enhancement is obtained for particle sizes outside these “high-enhancement windows”.

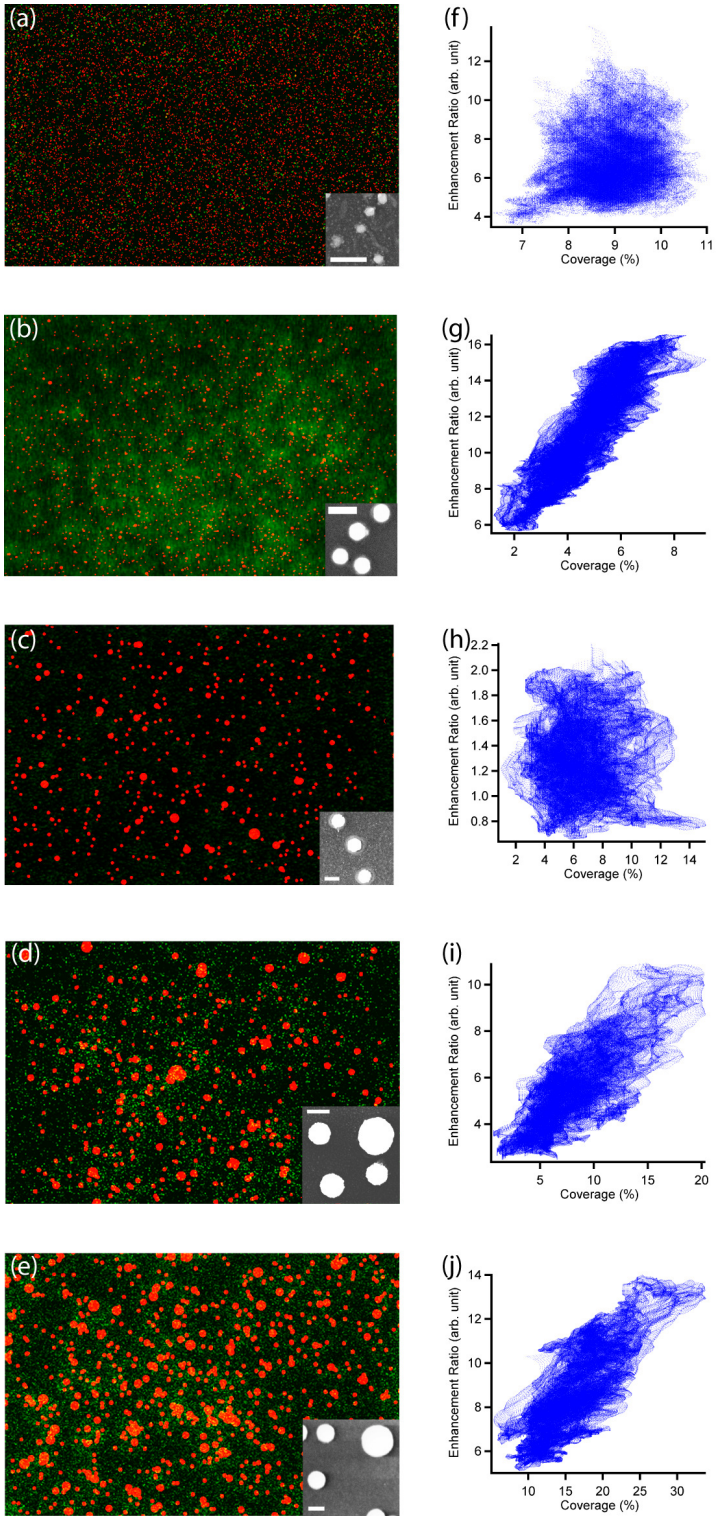

Figure 3.2.1 (a)-(e) SEM images (red) of the Ag nanoparticles deposited on silicon substrates, and the corresponding fluorescent images (green) for Cy3 fluorophore scanned with LSM from the same cell: The field of view is 20 µm. (f)-(j) Fluorescent intensity vs. local Ag nanoparticle coverage determined from 10 µm windows from panels (a)-(e). The average particle diameters in each panel are (a), (f) 67 ±1 nm, (b), (g) 96±2 nm, (c), (h) 173±24 nm, (d), (i) 271 ±14 nm, and (e), (j) 319 ±17 nm. The inset in panels (a)-(e) show higher magnification SEM images allowing the particle shapes to be seen; the size of the scale bar in the insets is 200 nm.

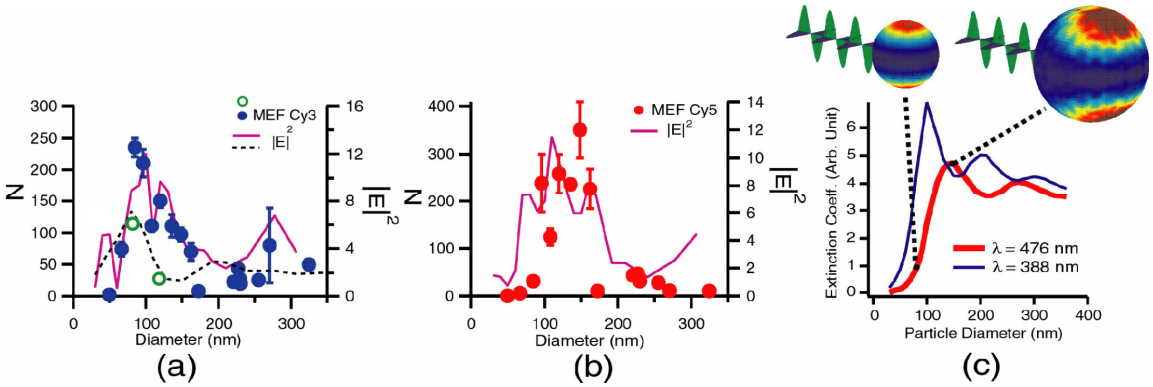

Figure 3.2.2 Measured normalized enhancement of the fluorescence, N, on silicon substrate (filled circles) or glass substrate (open circles), and the calculated (DDA) average E-field intensity (solid curve) near the Ag particles as a function of Ag particle diameter: (a) 514 nm excitation (Cy3 fluorophore), (b) 633 nm excitation (Cy5 fluorophore). The dashed curve in (a) shows the same averaged E-field intensity calculated by DDA for the case of glass substrate. (c) Calculated extinction coefficient and electrical field intensity, $|E|^2$, (with $|E|^2$ normalized to incident amplitude) for silver nanoparticles by DDA. Extinction coefficients are plotted as a function of particle diameter for incident light wave length fixed at 476 nm (633 nm in air) in red curve and 388 nm (514nm in air) in blue curve. Insets show the $|E|^2$ distribution over a spherical surface 8nm from the surface of silver particles with diameter of 80nm and 150 nm, respectively. The incident light represented by the sinusoidal modulations is traveling toward the particle, and the E-field is polarized in the vertical direction (colored in green). The color scale bar indicates the field intensity normalized to that of the incident light.

To understand the origins of the fluorescence enhancement dependence on particle size, we calculate the response of silver nanoparticles to incident light, using the discrete dipole approximation.[80, 82] In our experiment, the silver nanoparticles are always immersed in a thin layer of dilute buffer solution. Thus we assign the index of refraction of the space outside of the silver particle to that of water [83] for all calculations. For simplicity, in our calculations we model the incident light as a linearly polarized plane wave. Our SEM images show that the average particle separation well exceeds the individual diameters; therefore we limit our numerical calculations to the case of single silver nanoparticle. We begin with the simplest geometry, i.e. freely standing spherical silver nanoparticles. Fig. 3.2.2 (c) shows the calculated extinction coefficients, normalized to the geometric cross section of the particle as a function of particle diameter. The thin blue curve is for an excitation wavelength of 388 nm in water, corresponding to 514 nm in air. The thick curve is for excitation at 476 nm in water, or 633 nm in air. These two curves display qualitatively similar trends: the extinction coefficient first increases with particle diameter reaching a maximum, (at ~100 nm for the former case and ~140 nm for the latter case) then oscillates around a slow decaying tail. This behavior is qualitatively inconsistent with the abrupt drop in enhancement beyond the high-enhancement windows shown in Fig. 3.2.2(a), (b). Adding the substrate to the calculation might be expected to change the trend quantitatively, but not qualitatively.[84] This difference in behavior contradicts a simple correlation of fluorescence enhancement with resonant coupling between the incident light and plasmons in the silver nanoparticles. A hint as to the origin of this discrepancy comes from the calculated distribution of

electrical field intensity [85] near the particle shown in the insets. We note that the fluorescence intensity is expected to be proportional to the local intensity $|E|^2$. The leftmost inset shows the spatial variation of the calculated E-field intensity, normalized to that of the incident light in the vicinity of an 80nm diameter silver particle, for a wavelength of 476 nm. While the optical extinction from silver nanoparticles in this size range is small, there is nonetheless a strong E-field enhancement in regions near the top and the bottom poles of the particle. The rightmost inset shows that as the particle diameter increases to 150 nm, close to where the maximum optical extinction occurs, the regions of high E-field shift away from poles of the particle. Significantly, the main effect of the particle size is in the spatial distribution, rather than the maximum value of the field strength.

We now consider how the silicon substrate affects this picture. Simple models of the enhancement based entirely upon the plasmon resonance suggest it should simply red-shift the resonance. We include it in our calculation, treating it as a finite square slab of silicon [86] placed behind the particle in the direction of the wave vector $\vec{k}$ of the incident light. The lateral dimension of the silicon slab is chosen as 3 times the diameter of the silver particle; larger sizes are precluded by computer memory and practical computing time. We vary the thickness of the silicon slab from 75 nm to 450 nm, but find that this does not change the qualitative trend of the result. Figure 3.2.3 shows how the calculated E-field distribution in the azimuth of incident E-field polarization changes with the size of the silver nanoparticles; here a 150 nm thick silicon substrate and an incident light wavelength of 388 nm in water (514 nm in air) are used. Fig. 3.2.3 (a) and (e) are 3D and cross-sectional renderings,

respectively, of the calculated intensity $|E|^2$ for a relatively small diameter of 60 nm. As can be seen most clearly in the cross-sectional view, the silicon substrate, because of its large dielectric function, has a profound effect on the field; for this size the strongest field enhancement occurs beneath the particle. As shown in Fig. 3.2.3 (b) and (f), increasing the particle size to 100 nm, close to the observed optimum in Fig. 3.2.2 (a), causes regions of strong E-field enhancement to sweep upward, to the regions at and above the equator of the particle. A further slight increasing in particle diameter to 120 nm results both in a slight downward sweep of the high field regions (Fig. 3.2.3 (c), (g)), and a decrease in the measured enhancement (Fig. 3.2.2 (a)). Increasing the particle size further, to 210 nm, both sweeps the regions of high E-field back into the region beneath the particle as shown in Fig. 3.2.3 (d), (h), and causes a dramatic drop in the measured intensity (Fig. 3.2.2 (a)).

This sweeping of regions of high field, and its correlation to the observed fluorescence enhancement demonstrate the profound effect of coupling to the silicon substrate. Both the particles and substrate are opaque at these wavelengths; only the fluorescent emission from molecules located in regions which are not shadowed by the particles can be observed. Remarkably, ***this active substrate has a strong effect on the size-dependence of fluorescence enhancement in the presence of a substrate.*** As a rough means of accounting for the shadowing effect in our calculation, we average the E-field intensity, i.e. $|E|^2$, over only that region of the particle for which no shadowing occurs. Based upon the known thickness of the protein and spacer layer, the fluorescent tags are between 4-12 nm from the surface of the silver nanoparticles. We thus calculate the E-field intensity averaged over a hemi-spherical

surface 8 nm from the particle surface opposite the substrate. We note that although regions of high field also exist within the substrate, no fluorescent molecules exist there. Summary plots of the size dependence of this averaged E-field intensity for the two excitations are shown as solid curves in Fig. 3.2.2(a), (b). Good agreement between the measured fluorescence enhancement and the calculation is evident in both cases. This result shows that the distribution of the enhanced E-field intensity is crucial to the measured fluorescence enhancement, and leads to an important insight: ***as the particle size varies, regions of electrical field enhancement shift position; maximum fluorescence enhancement occurs when a large fraction of those fluorophores which are not shadowed by either the particles or substrate are immersed in regions of high field; low or no enhancement otherwise.***

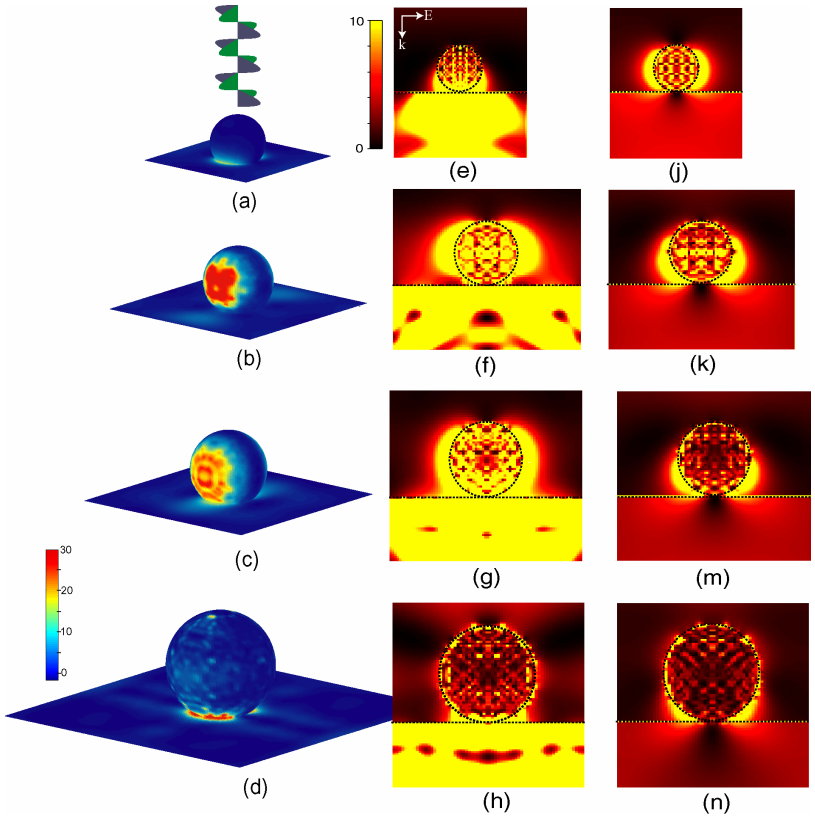

Figure 3.2.3 Calculated electric field intensity ($|E|^2$) distributions at the distance 8 nm from the surface of the silver nanoparticle and the silicon substrate. The particle diameters are 60nm, 100nm, 120nm, and 210nm for panels (a), (b), (c), and (d), respectively. As shown in panel (a), the incident light propagates downward and the polarization of the E-field is parallel to the substrate (colored in green). The wavelength of the incident light is 388 nm wavelength (514 nm in air). The color table indicates the field intensity normalized to the incident light intensity. Panels (e), (f), (g) and (h) are cross sectional renderings of electric field intensity ($|E|^2$) for particle diameters of 60nm, 100nm, 120nm, and 210nm, respectively; panels (j), (k), (m) and (n) are cross sectional renderings of the electric field intensity ($|E|^2$) for the same particle diameters, but on a SiO_2 substrate.

Our results thus demonstrate that coupling to an active substrate plays a striking, and unexpected role in the optimum enhancement of fluorescence by metal nanoparticles. Fluorescence from molecules located in close proximity to silver nanoparticles on a silicon substrate depends strongly on the particle diameter, with optimum normalized enhancement of at least 350 fold; the silicon substrate controls the regions of strong electric field, and in particular for which particle diameters are these regions not shadowed by the particles themselves. This effect is even more striking when compared to the field intensity which results from a more conventional, passive substrate, SiO_2. Fig. 3.2.3(j) - 3.2.3(n) show the calculated $|E|^2$ distribution for the same particle sizes as for the Si substrate. The substrate perturbs the field much less strongly, resulting in a conventional dipole-like distribution for smaller particles, and mixed dipolar/quadrupolar distribution at larger diameters. The resulting $|E|^2$ vs. size dependence is shown as the dashed curve in Fig. 3.2.2(a). The maximum is shifted to a smaller diameter, and reduced by approximately a factor of 2; measurements, of the fluorescence enhancement for a SiO_2 substrate, shown by the open circles in Fig. 3.2.2(a) indeed show approximately half of the enhancement measured using a Si substrate. The effect we see is similar to the hot-spot effect between particles which is believed responsible for the observation of single molecule spectrum in SERS.[87] Here, however it is the "hot regions" around single particles, where high electrical field and thus large enhancement occurs. We thus find that it is essential to include the spatial distribution of the field near the nanoparticles into the consideration for optimizing design of biosensors employing plasmonic response from metallic nanoparticles.

Chapter 4: Experimental Methods for Efficiency Enhancement for Organic Bulk Heterojunction Photovoltaic Devices

In this chapter, we describe our fabrication process for the Au nanopillar array patterned organic photovoltaic devices studies as the major part of this thesis. We also describe the characterization techniques used to determine the performance of the devices with different configurations of nanoparticles fabricated by e-beam lithography. In the next chapter, we compare the performance with results of simulation, and discuss whether nanostructures result in enhanced light absorption and whether they improve the efficiency of organic bulk heterojunction solar cells.

4.1 Design of the Photovoltaic Device

We modified a conventional design for organic solar cells [19] to include arrays of noble metal nanopillars. In this design the active layer functions to produce carriers by absorption the incident light, and is a mixture of poly(3-hexylthiophene) (P3HT) with [6,6]-phenyl C61 butyric acid methyl ester (PCBM-C_{60}) (weight ratio 1:1). The P3HT and PCBM serve as donor and acceptor molecules, respectively, in separating the electrons and holes produced by absorption of the incident light. P3HT was chosen because it has a high absorption coefficient close to the maximum photon flux in the solar spectrum. P3HT is also known in the field of organic electronics as a high-mobility material. The mobility of the blend of P3HT:PCBM 1:1 weight ratio has been reported to be 2.5×10^{-3} $cm^2/V \cdot s$ and a higher mobility up to 5×10^{-3}

$cm^2/V \cdot s$ can be achieved by an annealing process.[88] We sandwiched the active layer between two conductive layers: the bottom layer is indium-tin oxide (ITO) which serves as a high work function (4.7 eV) anode; the top layer is Al which serves as low work function (4.3eV) cathode. The high and low work functions allow for collection of holes and electrons, respectively.

4.2 *Fabrication of the Photovoltaic Device*

We now give a brief description of the design and fabrication procedure. In addition to inclusion of arrays of Au nanopillars, a further change in design from previous work [19, 20, 40, 89] was the reconfiguration of the electrical contact for the measurement circuitry. The new design avoided complete overlap between the Al contact pads and the underlying Au layer. A control cell was fabricated on each sample, using the same architecture as for the NP patterned cells, except without Au nanopillars. The steps used in our fabrication were:

1. Anode definitions. We started with 1 inch by 1 inch transparent ITO-coated glass substrates purchased from Delta Technologies (figure 4.2.1). The ITO has a sheet resistance 4-8 Ω/□ and a thickness of ~ 200 nm. The regions of ITO to be removed (figure 4.2.2) were defined by transferring a photoresist pattern onto the ITO layer. This was followed by wet chemical etching using HCl for 5 min at 80 ^{o}C hot plate temperature. A digital multimeter was used to check whether the ITO was completely cleared without leaving any unwanted residual layer that can short out the device. This left behind 4 separate anodes on the substrate, and allowed measurements to be done for 3 nanopillar arrays plus a control on each sample.

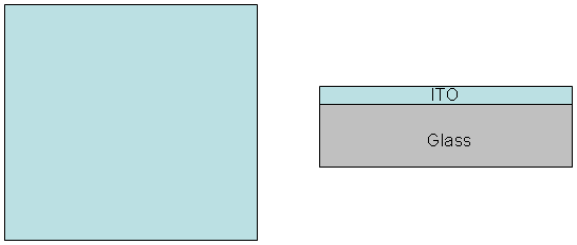

Figure 4.2.1 Schematic of an ITO coated glass substrate before anode definition.

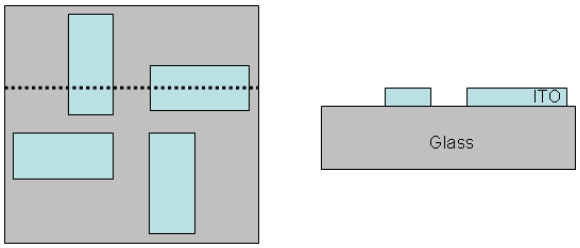

Figure 4.2.2 Schematic of an ITO coated glass substrate after patterned 4 anodes.

2. *Pattern square Au NP arrays on ITO by e-beam lithography (Fig. 4.2.3).* The details of the e-beam lithography process follow those given in chapter 2. Three of the anodes on each sample were patterned with Au nanopillar arrays with either the same or different pillar sizes; the fourth anode was used for the control device. The total pattern size was 120 μm by 120 μm in each case.

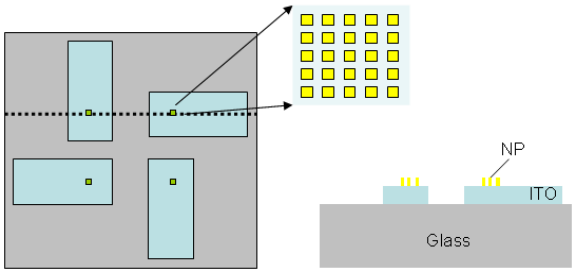

Figure 4.2.3 Patterning of Au NP arrays on ITO surfaces by e-beam lithography.

4. *Definition of the active region by photolithography (Fig. 4.2.4 and 4.2.5).* The regions in which the active organic layer overlap the anode and cathode are much larger than the Au nanopillar arrays: 5 mm × 2.5 mm. To ensure that the measured photocurrent comes almost entirely from the region of the NP pattern, we thus create an opaque mask, consisting of a 200 nm thick Au film and 100 nm insulator of aluminum oxide, around the nanopillar patterned area. The oxide layer was added to prevent a short circuit between the Al (top) and ITO (bottom) electrodes.

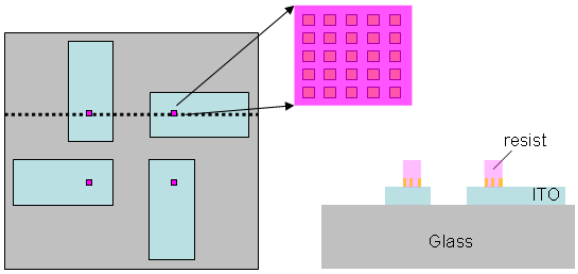

Figure 4.2.4 Patterning of negative photo-resist in the active regions.

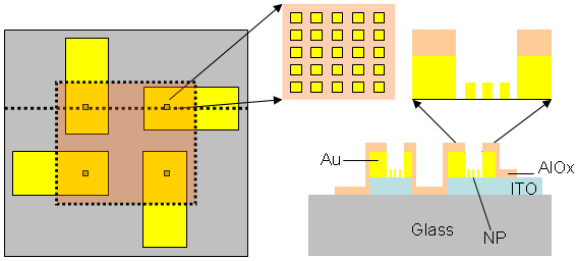

Figure 4.2.5 Device structure with an opaque mask, consisting of a 200 nm thick Au film and 100 nm insulator of aluminum oxide, around the nanopillar patterned area.

5. Deposition of *active and interface layers (Figure 4.2.6).* Our active layer consisted of a blend of regio-regular poly(3-hexylthiophene-2,5-diyl) (P3HT) and [6,6]-phenyl-C61-butyric acid methyl ester (PCBM). A solution comprised of P3HT (1.5 wt%) plus PCBM (1.5 wt%) in dichlorobenzene (DCB) was spin-cast at 400 rpm onto the Au nanopillar (NP) patterned anodes and surrounding substrate for 45 seconds. Immediately after spin-coating, the film was "solvent-annealed", i.e. placed in a covered glass jar with a small amount of DCB solvent added into the bottom for 30 minutes. The thickness of the resulting active layer was determined to be 220 nm by AFM and profilometer measurements. Following this, 1 wt% nonstoichiometric TiOx precursor solution prepared by a sol-gel method,[90] and was spun-cast at 4000 rpm onto the P3HT:PCBM composite. The above steps were carried out in an inert nitrogen gas atmosphere inside a glove box to minimize photo-oxidative degradation. Then the sample was heated at 80 °C for 10 min in air. The resulting 30 nm thick TiOx layer reduces the barrier to electron injection and protects the organic active layer from oxidation.

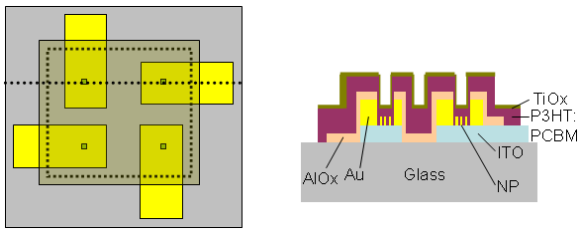

Figure 4.2.6 Device structure after coating the TiOx layer.

6. *Deposition of the cathode.* The sample was transferred back into the nitrogen glove box and 300 nm thick aluminum (Al) contact pads were thermally evaporated onto the TiOx layer through an Al shadow mask. (Fig. 4.2.7)

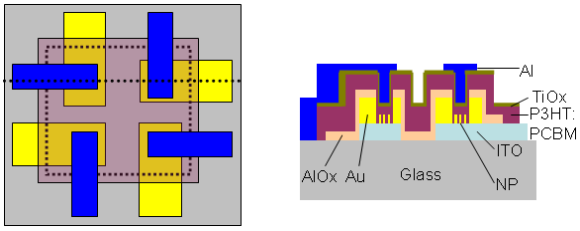

Figure 4.2.7 A complete solar cell devices on a sample.

4.3 Scanning Electron Microscopy Characterization

A field emission scanning electron microscope (SEM, JEOL JSM-6500F, operated at 30 kV) was used to characterize the sample condition after each fabrication step, and determine the pillar edge length and pitch of the Au nanopillar arrays. Images are shown in figure 4.3.1.

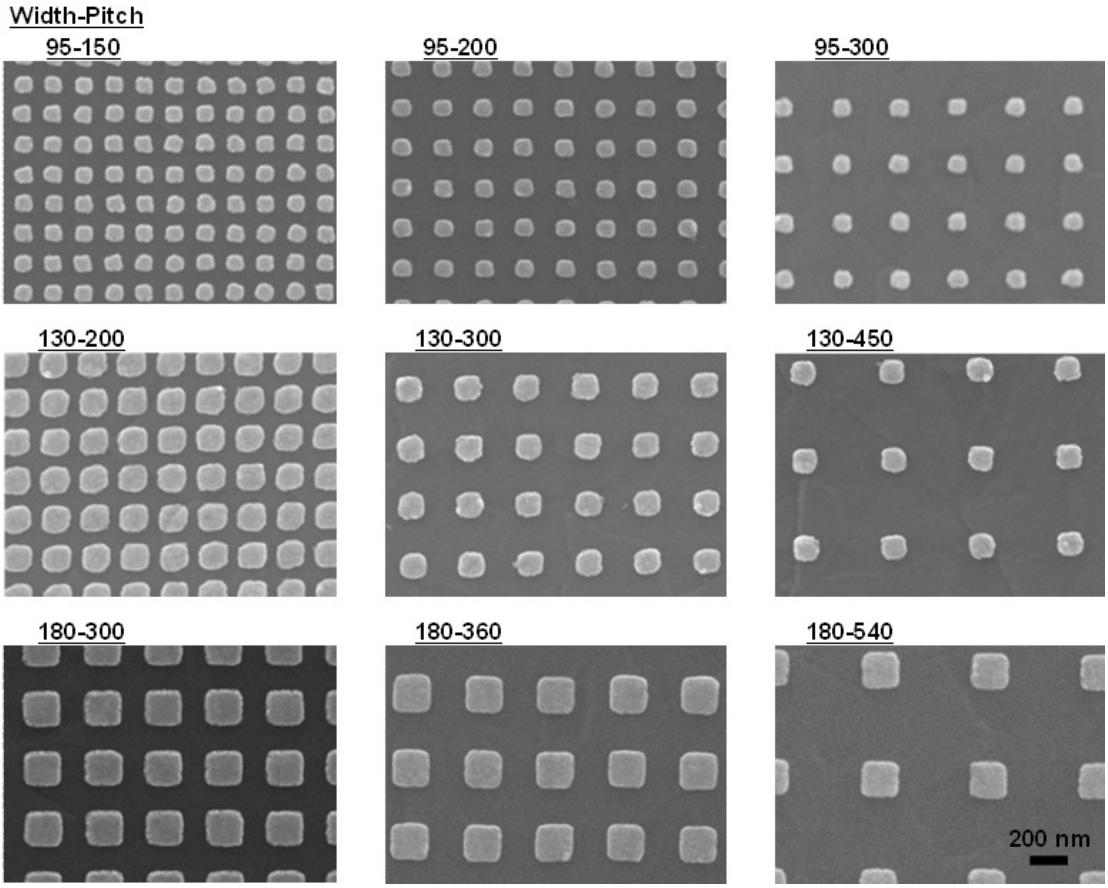

Figure 4.3.1 SEM images of the Au nanopillar arrays on ITO coated glass substrate. The widths and pitches of the individual image are shown on the top-left corner of each image. The height of the nanopillars is fixed at 70 nm.

4.4 Atomic Force Microscopy Characterization

We used a Digital AFM (Dimension 3100^{TM}) to inspect the surface cleanness after each step of sample preparation to make sure the photoresist was removed properly. We also used the AFM to characterize the particle height and the morphology of the active layer coating on patterned nanopillars. The measured morphologies of the bare Au NPs surface, P3HT:PCBM surface coated onto nanopillar arrays, and P3HT:PCBM surface coated onto ITO surfaces are analyzed statistically by calculating height-height correlation function:

$$G(\vec{R}) = \left\langle h(\vec{r}\,) \cdot h(\vec{r} + \vec{R}\,) \right\rangle \tag{4.4.1}$$

where h is the local height of the surface at $\vec{r}$, $\vec{r}$ and $\vec{R}$ are two-dimentional translation vectors lying within the average surface plane, and the average is over the entire image, < > denotes an average over $\vec{R}$. G measures how the correlation in height between different parts of the surface falls off with distance. The results were used to determined whether the P3HT:PCBM composite wet the nanopillar patterned surface.

Figure 4.4.1 shows example AFM images and the corresponding height-height correlation function maps for the sample with Au nanoparticle arrays before (4.4.1 (d)) and after (4.4.1 (e)) depositing P3HT:PCBM. Fig. 4.4.1 (f) shows a correlation map after deposition onto the control sample. Both before and after coating P3HT:PCBM for the sample with Au nanopillar arrays show a periodic pattern, which indicates that the P3HT:PCBM does wet the surface of Au nanopillars, producing a conformal layer. No periodicity is seen in the map for the coated control device.

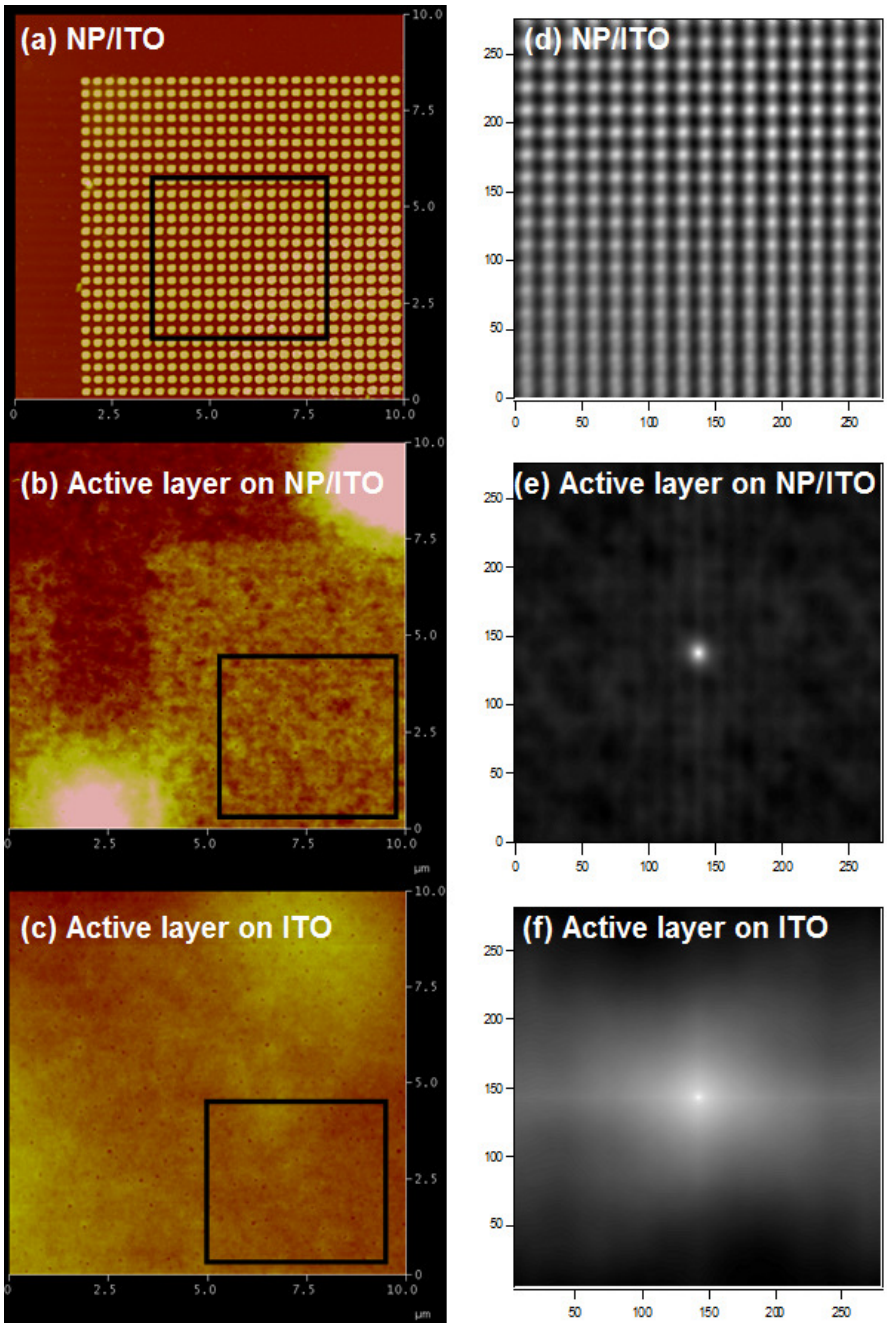

Figure 4.4.1 AFM images (a) of a Au nanopillar array, (b) of the same array subsequent to coating with P3HT:PCBM, (c) of a control device after coating with P3HT:PCBM. Height-height correlation maps (d) produced from image (a), (e) produced from image (b), (f) produced from image (c). The black square lines indicate the regions of correlation maps.

4.5 *Photovoltaic Device Performance Measurements*

There are two principal measurements that are generally carried out to determine the performance of the solar cell devices: 1) power conversion efficiency measurement to determine the overall efficiency and 2) external quantum efficiency measurement to know the spectrum response.

4.5.1 Power Conversion Efficiency Measurements

The power conversion efficiency (PCE) of the solar cell can be determined by a current vs applied voltage (I-V) measurement under illumination. The PCE is given by:

$$\eta = \frac{P_{\max}}{P_{in}} = \frac{\max\{I \times V\}}{P_{in}} = \frac{I_{sc} \times V_{oc}}{P_{in}} \times FF \qquad (4.5.1.1)$$

, where P_{in} is the input light power, I_{sc} is the current reach the contacts without applied biase, V_{oc} is the maximum potential generated by the device, FF is the fill factor. The fill factor is the ratio between the maximum power generated (P_{max}) and the product of I_{sc} and V_{oc}, and is related to the quality of the device (Fig. 4.5.1.1).

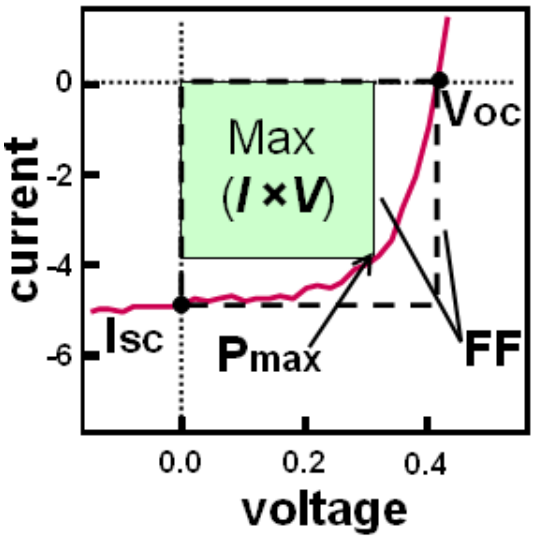

Figure 4.5.1.1 Current vs. applied voltage (I-V) characteristics of a solar cell.

To determine the power conversion efficiency (PCE) of our devices, we measured the output current as a function of bias voltage during illumination with a simulated solar illumination source (Newport, 91160 Full Spectrum Solar Simulator, collimated, 2 inch × 2 inch output beam), with an air mass 1.5 Global (AM 1.5 G) spectrum source. The set up of the measurement is shown in figure 4.5.1.2. Examples are shown in fig. 4.5.1.3. Figure 4.5.1.3 (a) is for a device without Au nanopillars, and containing a PEDOT:PSS layer between the ITO layer and the P3HT:PCBM active layer. Fig. 4.5.1.3 (b) is for our devices with the black curve for a control device, i. e. without Au nanopillars, and the red and blue curves for nanopillar patterned devices. The corresponding quantities for fig. 4.5.1.3 are summarized in table 4.5.1.1. The efficiency of our normal micro cell (with a 40 nm PEDOT:PSS) is ~2% which is comparable to the devices on the microscopy scale on

the order of few millimeter square. Clearly there is a large reduction in PCE in the absence of the PEDOT:PSS layer, presumably due to a reduction in charge collection efficiency. Our interest is in the effect of the Au nanopillars, however. The efficiencies of device with nanoparticle are about the same compared to the devices without nanoparticles. The efficiencies (η_p) of our devices (table 4.5.1.1) are ~0.1 %, J_{sc} is ~2mA/cm^2, and V_{oc} is 0.28 V, and FF is ~0.23 under AM 1.5 illumination with incident power 95 mW/cm^2, which is about the same performance compared to what our cooperators have [42] ($\eta_p < 0.6\%$, FF ~ 0.2) for the devices without the PEDOT:PSS layer.

A problem with the PEC as a measure of efficiency is that it does not allow us to understand the individual efficiencies associated with photo conversion. To gain a better understanding of the effect of the nanopillar arrays, we thus instead consider the external quantum efficiency EQE (λ) = $\frac{J/e}{I_{in}/h\upsilon}$ = η_A x η_{ED} x η_{CT} x η_{CC}, and in particular how it varies with optical wavelength.

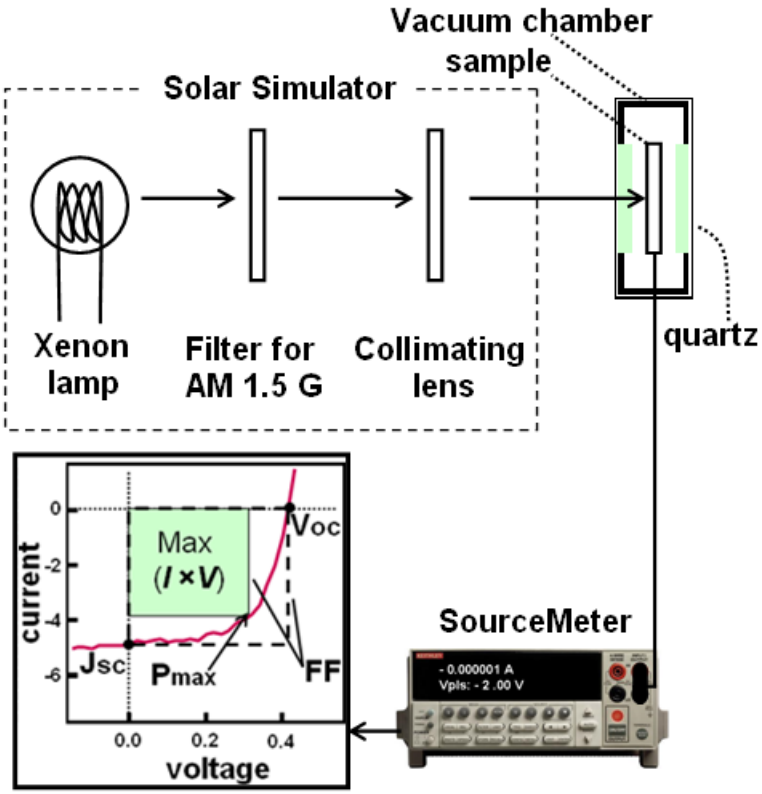

Figure 4.5.1.2 Schematic of the set up of the power conversion efficiency measurement.

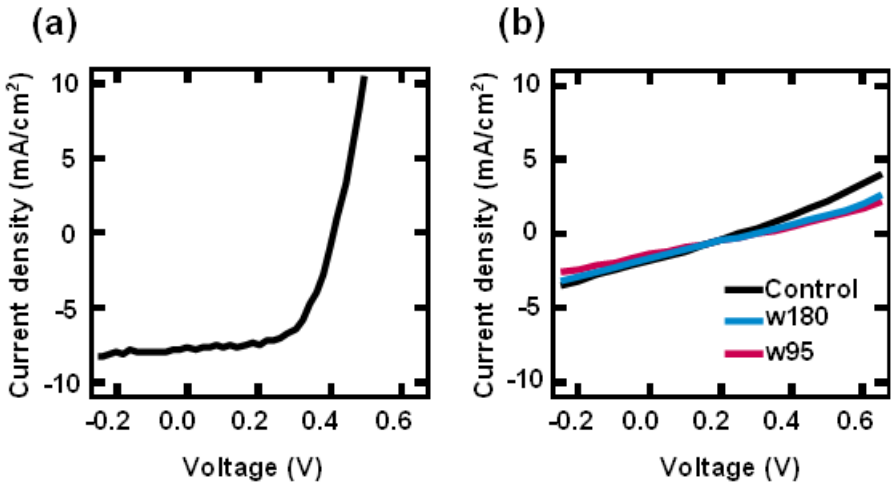

Figure 4.5.1.3 I-V curves of the micro solar cell device (a) with PEDOT:PSS layer, and (b) without. (b) The black curve is the control cell without Au nanopillar arrays and the blue and red curves are devices with Au nanopillar arrays with particle width 180 nm and 95 nm, respectively. The period of the Au nanopillars is three times of nanopillar widths.

	Coated with PEDOT:PSS	Control	W 180 nm	W 95 nm
J_{sc} (mA/cm^2)	7.68	1.81	1.63	1.46
V_{oc} (V)	0.41	0.243	0.297	0.288
FF (%)	0.60	0.239	0.233	0.241
PCE (%)	2.0	0.126	0.119	0.105

Table 4.5.1.1 The performance of the micro solar cell devices with I-V curves shown in figure 4.5.1.3.

4.5.2 External Quantum Efficiency Measurements

To determine the optical spectral response of cells both with and without NP present, the external quantum efficiencies (EQE) of patterned and control devices on a single sample were measured vs. wavelength of the incident light. The external quantum efficiencies (EQE) measurement was performed by measuring the short circuit current vs wavelength of the incident light and the measurement set up is shown in figure 4.5.2.1. Measurements were carried out with the samples maintained under vacuum (~14 Torr), using a spectrophotometer with a quartz tungsten halogen source (Spectra Physics), integrated with a computer-controlled monochromator (SPEX). The incident light was modulated by a chopper rotating at a frequency of 100 Hz, and the short circuit current, J_{sc}, (measured current without applied voltage) as function of wavelength was measured using a lock-in amplifier with the chopper frequency as external reference. The source power spectrum was measured using a commercial power meter (ThorLabs, working optical wavelength from 400 nm to 1100 nm). The schematic of the measurement set up is shown in figure 4.5.2.1. We present the results of such measurements in chapter 5, along with calculations of the optical absorption for our devices. Below we describe our optical characterization.

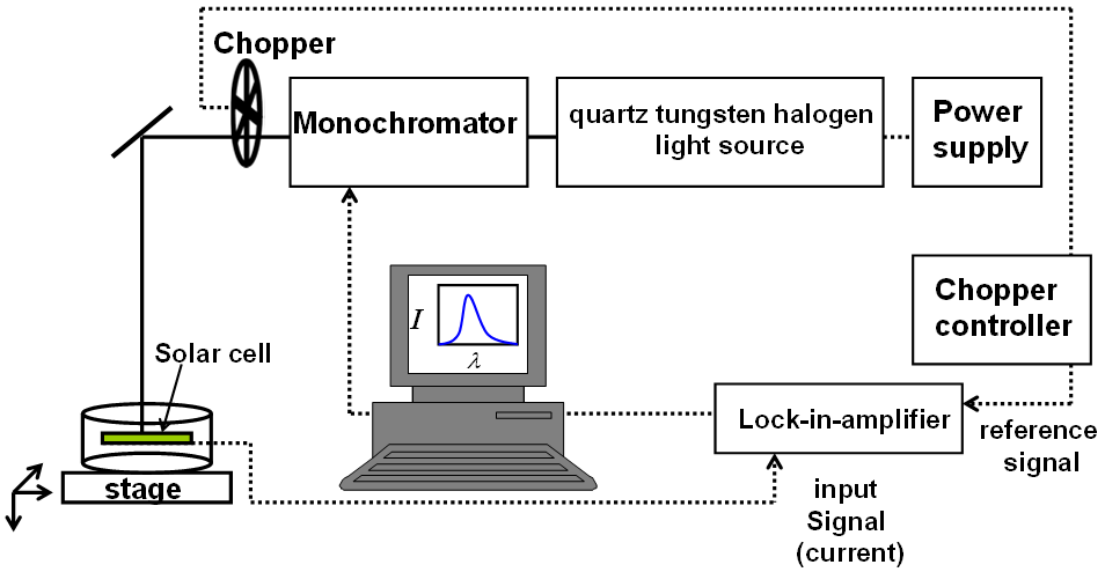

Figure 4.5.2.1 Schematic of the external quantum efficiency measurement set up.

4.6 Refractive index measurements

We determined the complex refractive index, $n+ik$, of ITO and P3HT:PCBM layers comprising our devices by spectroscopic variable angle ellipsometry using the Drude-Lorentz model (presented in Appendix E). To obtain a more accurate value of k for the active layer (k_A), we also measured the transmission spectrum for similar films on a glass substrate, correcting for the reflectance at the interfaces using n_A for P3HT:PCBM (determined ellipsometrically) and the known value of n for glass.

Determination of k_A is more involved. Figure 4.6.1 illustrates the structure of the transmission measurement on a glass substrate and on a single film on glass. The transmission for a beam passing though a glass substrate (T_{glass}) and though a single film on glass substrate ($T_{film/glass}$) are approximately equal to

$$T_{glass} = t_{ag}^{\,2} \bullet t_{ga}^{\,2} \times I_{in} \qquad (4.6.1)$$

$$T_{film/glass} = t_{af}^{\ 2} \bullet t_{fa}^{\ 2} \bullet t_{ga}^{\ 2} \times I_{in} \times \exp(-4\pi kl/\lambda) \tag{4.6.2}$$

, where t_{ag} , t_{ga} , t_{af} , t_{fa} , t_{ga} are the transmission coefficients at the interfaces of air/glass, glass/air, air/film, film/air, and glass/air, respecticely. I_{in} is the intensity of the incident light, *k* is the extinction coefficient of the film, and *l* is the film thickness that can be measured by a profilmeter. The ratio of the measured transmission is

$$\frac{T_{film/glass}}{T_{glass}} = \frac{t_{af}^{\ 2} \bullet t_{fa}^{\ 2}}{t_{ag}^{\ 2}} \times \exp(-4\pi kl/\lambda) \tag{4.6.3}$$

The transmission coefficients can be calculated by

$$t_{12}^{\ 2} = T_{12} = 1 - R_{12} \ , R_{12} = \left(\frac{\frac{n_2}{n_1} - 1}{\frac{n_2}{n_1} + 1} \right)^2 \tag{4.6.4}$$

Thus, substituting the transmission coefficients calculated from equation (4.6.4), the extinction coefficient of the film *k* can be obtained. In our analysis, the n_A of the active layer was taken from the ellipsometry, which was substituted into (4.6.4) to obtain the k_A of the active layer, calculated from equation (4.6.3).

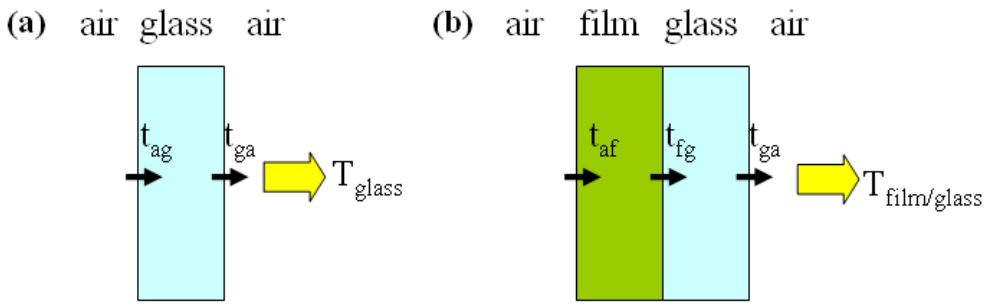

Figure 4.6.1 Schematic of the transmission measurement on (a) a glass substrate and on (b) a single film on glass.

4.6.1 Extinction/ Absorption Measurement

Both optical extinction from Au nanopillar arrays, and absorption of P3HT:PCBM films were measured by the transmission using a Cary 5000 UV-Vis-NIR spectrophotometer, equipped with a monochromateor (figure 4.6.1.1). As for the extinction measurements from Ag nanostructures described in Ch. 2, we used this approach to determine localized surface plasmon resonance frequencies for arrays of Au nanoparticle with varied size and shape by transmission measurements. The Cary 5000 UV-Vis-NIR spectrophotometer is equipped with a tungsten halogen (visible) and a deuterium arc (UV) lamps as light sources. The wavelength is selected by a monochromator equipped with two gratings for UV-Vis and NIR. The wavelength selected light is passed though a beam splitter that split the light into two directions: one goes to sample and the other direct goes to reference detector. The beam transmitted though the sample is collected by the other detector. R928 photomultiplier (PMT) and PbS photocell detectors were used for UV-Vis and for NIR, respectively.

For our optical extinction measurements, we used commercial glass slides, coated with a thin (~ 200 nm), transparent indium tin oxide (ITO) layer. As described in a previous section, we created an opaque mask, consisting of a 200 nm thick Au film, around the nanopillar patterned area to ensure that the measured transmission comes almost entirely from the region of the NP pattern. A reference spectrum from an opaque mask was measured and used as a baseline. Room-temperature transmission measurements for near-normal incident light and wavelengths from 300 nm to 1000 nm were performed.

For absorption measurements, we coated glass slides coated with a P3HT:PCBM film. In this case, the baseline value was taken from the measured transmission of a bare glass slide.

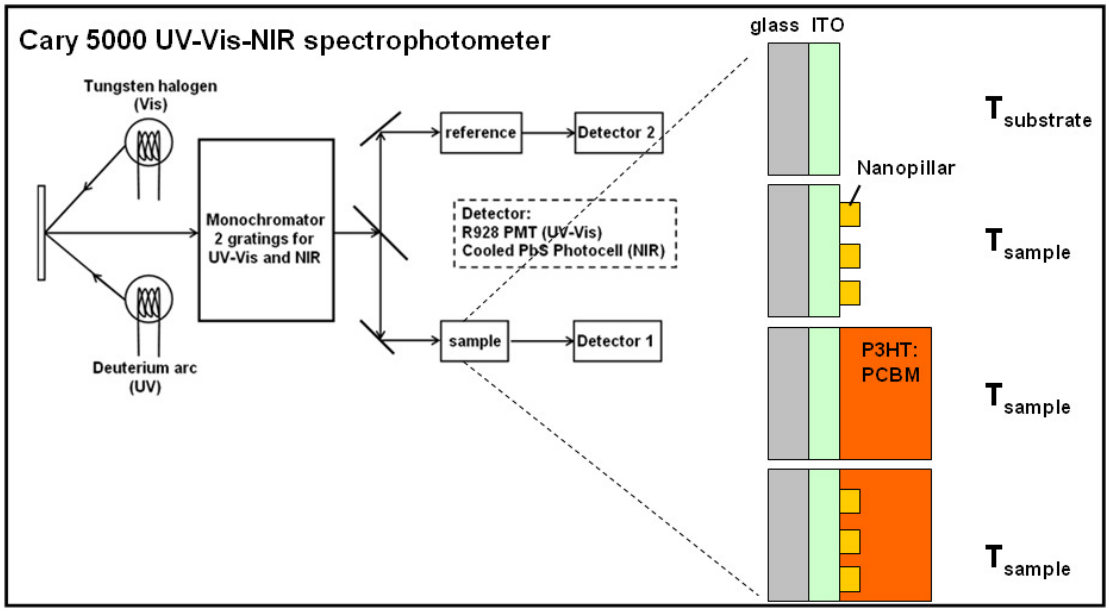

Figure 4.6.1.1 Schematic of the set up for transmission measurements.

Chapter 5: Experimental and Numerical Calculation Results and Discussions for Enhancement in Photovoltaic Devices

In this chapter, we present the major results of this thesis, a systematic investigation of the external quantum efficiency and calculated active layer absorbance for Au nanopillar array-patterned P3HT:PCBM organic solar cells as the pillar sizes, shapes, and pitches are varied. We identify a resonance in which there is an enhancement. We address the lock of overall enhancement based upon calculation of Joule heating absorbance within the Au nanopillars.

5.1 Effect of the Au Nanopillars in the Output of the Photovoltaic Devices

In this section, we describe our measurements of the effect of Au nanopillar arrays placed within the active layer of a bulk heterojunction organic solar cell on its external quantum efficiency. We fabricated arrays of gold nanopillars of varied lateral size and spacing onto the front contact (ITO) of our prototype solar cell devices. We investigated pillar widths of approximately 95 nm, 180 nm, and 400 nm, and pitches approximately 1.6 to 3 times of the pillar widths. We fixed the pillar height in theses investigations to a value of approximately 70 nm.

5.1.1 Measured Extinction vs Measured External Quantum Efficiency

It is often assumed that increasing the extinction due to excitation of localized surface plasmon (LSP) represents an increase in the absorption [7] by metallic

nanostructures or an increase in the forward scattering or a combination of the two, should give rise to increased solar cell efficiency. [67, 71, 73, 74] While it is relatively easy to either calculate the extinction efficiency for a free standing nanoparticle or to carry out extinction measurements for arrays of such structures, it is by no means clear that the light energy absorbed or scattered in extinction of localized surface plasmons in a solar cell will necessary increase its photoconversion efficiency. Here we put this assumption to the test, comparing the measured extinction spectrum from a Au nanopillar patterned BHJ OSC with its measured external quantum efficiency spectrum.

An example absorption spectrum for a P3HT:PCBM active layer is shown in Figure 5.1.1.1 (a); the film was prepared by a slow growth method (referred to as solvent annealing in section 4.2) on a glass substrate. According to the reports [19], slow grown and fast grown, films produce differences absorption spectra. During slow growth process the regioregular (RR) P3HT forms a well-organized interplane structure with lamellae orientated normal to the substrate. It has been reported that this structure shows enhanced absorption in the red region of electromagnetic spectrum and also increases the charge carrier mobility [19]. The shape of the absorption spectrum for our slow grown film is similar to others reported in the literature. Fig. 5.1.1.1 (b) shows a comparison of absorption spectra for different growth and annealing procedures. Three pronounced absorption peaks of the active layer can be observed for the slow grown film at ~ 605 nm, ~ 553 nm, and ~ 515 nm shown in figure 5.1.1.1 (a) and (b) (slow no. 1 as cast). These peaks have been identified as coming from the singlet excitonic transition at 2.05 eV with vibronic

sideband at 2.20 eV and 2.35 eV. [91] The peak at 605 nm results from the interplane interaction of the lamellae structure. The absorption of P3HT in high photon energy region above 2.5 eV has been assigned as due to the HOMO-LUMO transition with energy gap 2.75 eV. [91] The peaks at ~ 333 nm and shorter wavelength (~ 270 nm) have been attributed to absorption of PCBM. [91]

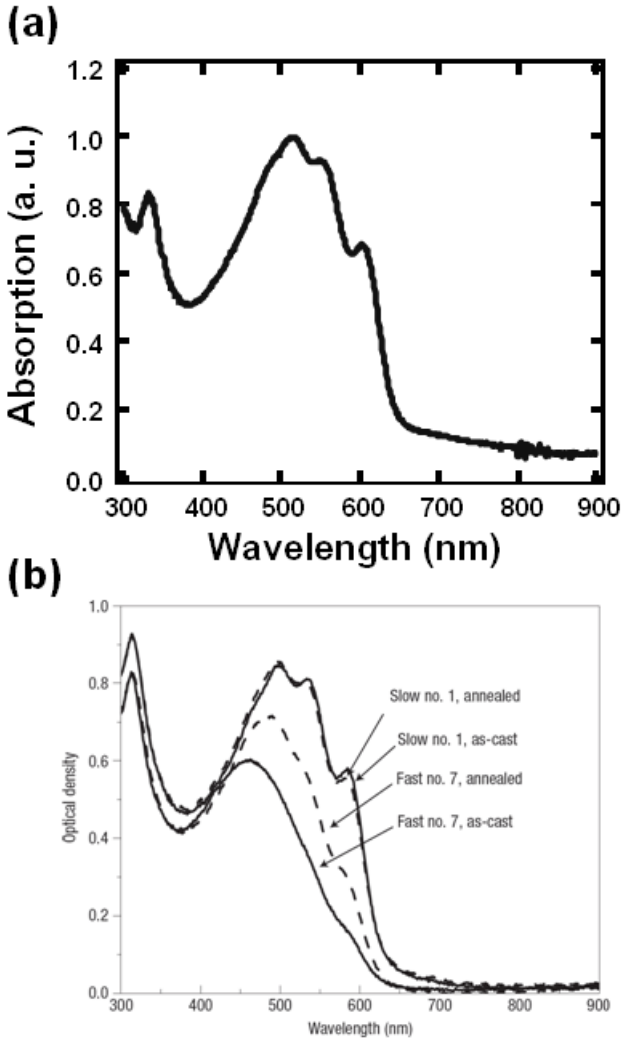

Figure 5.1.1.1 Absorption spectra of blends of P3HT:PCBM for different film preparations. (a) Absorption measured in this work. (b) Absorption taken from reference [19], showing differences according to growth and annealing procedures.

To explore the relationship between optical extinction and efficiency of OPV devices, we carried out transmission measurements in which we observed resonances typically identified with localized surface plasmons [11, 92, 93]. We evaluate the extinction as follows: $Extinction = 1 - \frac{T_{NPonSub}}{T_{Sub}}$, where $T_{NPonSub}$ is the transmission for samples patterned with Au NPs on the substrate and T_{Sub} is that of the ITO-coated glass substrate.

Example SEM images of the Au nanopillar (NP) arrays investigated in this work were shown in figure 4.3.1. Figure 5.1.1.2 (a) shows the extinction spectrum of the nanopillar-patterned samples with nanopillar widths of ~ 95 nm. The extinction peak is at ~ 596 nm in wavelength for pitch of 150 nm (figure 5.1.1.2 (a), purple curve). This extinction peak shifts slightly to 609 nm as we increase the pitch to 300 nm. Figure 5.1.1.2 (b) and (c) are the corresponding spectra for nanopillars with widths fixed at ~ 130 nm and at ~ 180 nm, respectively. For a fixed pitch of 300 nm, the peak shifts from 609 nm to 683 nm (5.1.1.2 (a)-(c), green curve) as the width increased from 95 nm to 180 nm. This is consistent with the expected red shift in the plasmon resonance for nanoparticles with increasing particle size [11, 13]. Figure 5.1.1.2 (d) shows a summary plot of the wavelength for the largest peak in the extinction, as the pitch is increased. The arrays with larger width nanopillars show a monotonic increase in red shift vs pitch. This is consistent with Haynes et. al.'s earlier extinction measurements for Au/Ag nanopillar arrays with cylindrical/triangular shapes, for pillars of lateral size 200/170 nm, height 35 nm, and pitches ranging from 230 to 500 nm [92]. They proposed a coupled dipole approximation (CDA) to explain this. This model indicates that the red shift of

localized surface plasmon resonance (LPSR) as particle spacing increasing (for pitch/lateral size > 1.5) results from radiative dipole coupling [92]. A second CDA calculation for 2-D arrays of spherical silver particles 60 nm in diameter also shows a red shift behavior as the ratio of pitch/diameter increasing from 2 to 6, but the total amount of this red shift is only 5 nm in extinction peak [94]. The smaller red shift for arrays of nanospheres with 60 nm in diameter [94] compared to oblate cylinder pillars with 200 nm wide [92] is seemingly due to the much different aspect ratio, i. e. between lateral size and height of nanoparticles (W/H) or due to the volume of the nanostructures. Our additional calculations indicate that the degree of red shift with pitch is associated with the dimensions of the individual nanopillars: the larger nanopillars arrays lead to stronger red shift of localized surface plasmon resonance as the pitch increased, apparently due to larger dipole moments. This is qualitatively what is expected from the dependence of the polarizability on nanoparticle dimensions as seen in Eq. (1.2.4) for a sphere.

To sum up, we have demonstrated that we can tune the extinction peaks over the range at least 600 nm wavelength to > 800 nm by selecting the corresponded combination of the particle width and pitch within the range explored. Following previous reports [92, 94], we explain the monotonic increase in the red shift of the resonance with pillar width as due to a stronger radiative dipole coupling effect for particle arrays with larger W/H ratio.

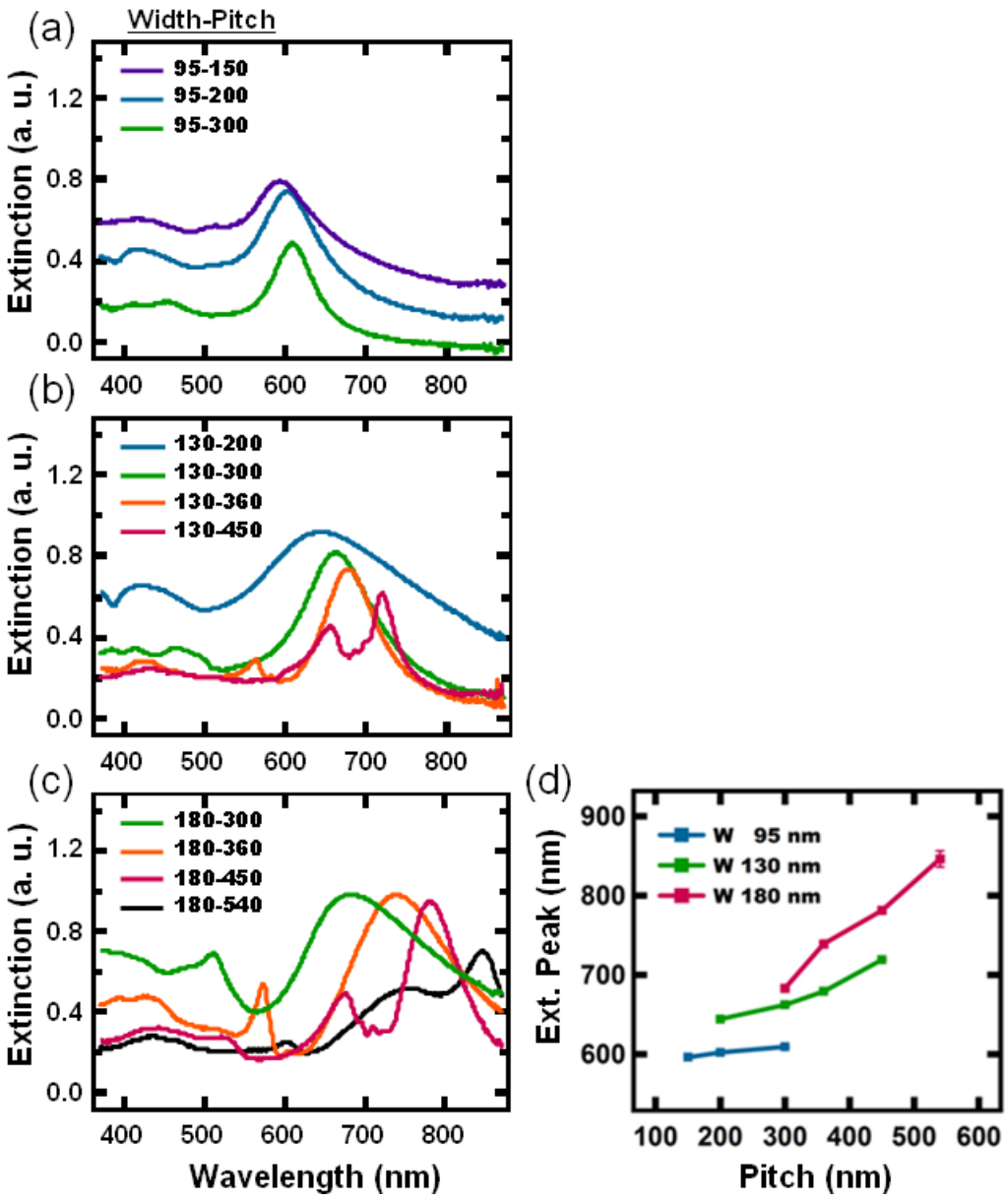

Figure 5.1.1.2 (a)-(c) The extinction spectra of the Au nanopillar arrays for different pitch with W= 95 nm, 130 nm, and 180 nm, respectively. (d) The summary plot of the maximum extinction peaks in (a)-(c).

Below we make a direct comparison of the measured optical extinction and performance of Au nanopillar-patterned organic solar cells; for this comparison we fixed the nanopillar height at 70 nm and the pitch at ~ 2 times of width. First however we show the effect of the P3HT:PCBM layer on the optical extinction. Figure 5.1.1.3 shows a side by side comparison of the extinction spectrum before (a)-(b) and after (c)-(d) depositing P3HT:PCBM for arrays of Au nanopillars which are 95 nm (left panels) and 180 nm (right panels) in width. The green curves show spectra for the samples with Au nanopillars, and the black curves in 5.1.1.3 (c) and (d) are for a control sample without patterned nanopillars. The thickness of the P3HT:PCBM layer is 168 nm, as determined by a profilometer measurement; this is sufficiently thin to avoid spectrum saturation. After coating with P3HT:PCBM (figure 5.1.1.3 (c)-(d)), the peaks in extinction shift toward the red: from approximately 602 nm to 657 nm for the 95 nm wide pillars, and from approximately 740 nm to 830 nm for the 180 nm wide pillars. This is due to the increase of dielectric constant of the surrounding medium, i.e. P3HT:PCBM, compared to that of air [11].

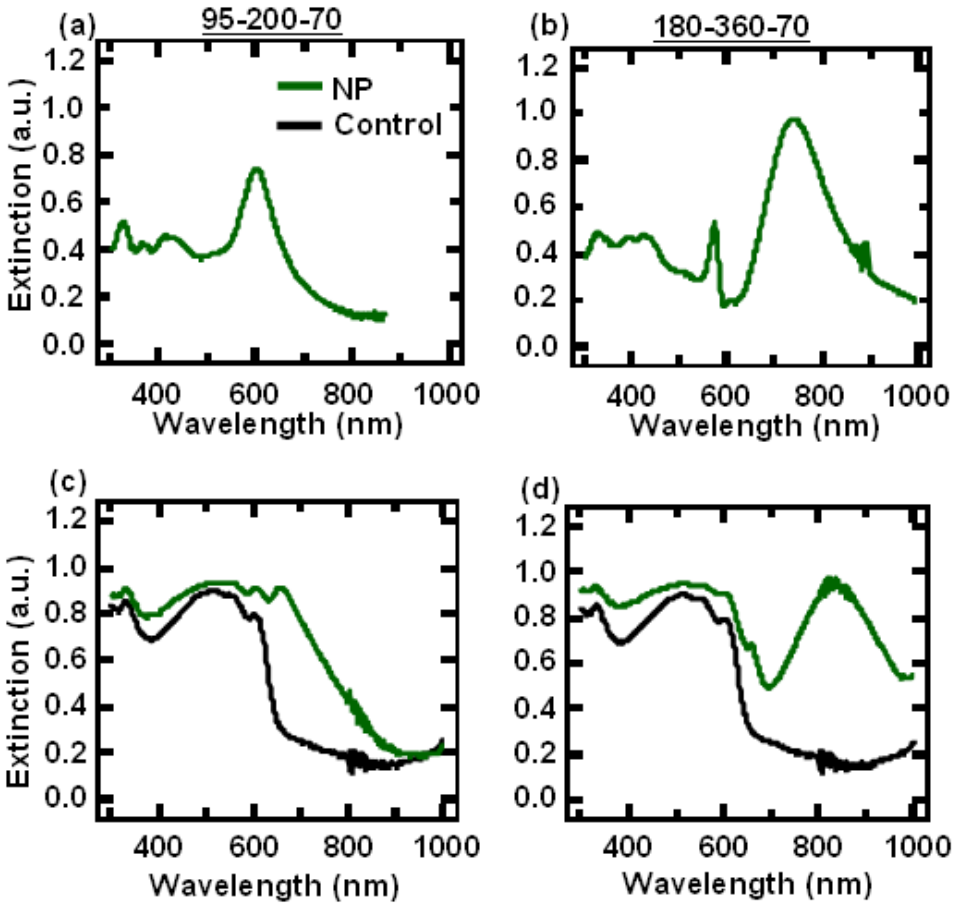

Figure 5.1.1.3 Extinction spectrum from Au NP arrays on ITO coated glass substrate: (a) for uncoated arrays of 95nm wide Au nanopillars spaced at 200 nm; (b) for uncoated arrays of 180 nm wide Au nanopillars spaced at 360 nm; (c) for 95 nm wide, 200 nm pitch Au nanopillar arrays coated with 168 nm of P3HT:PCBM (green curve); (d) for 180 nm wide, 360 nm pitch Au nanopillar arrays coated with 168 nm of P3HT:PCBM (green curve). In (c) and (d) black curves are for a control sample, i.e. P3HT:PCBM without Au nanopillars.

A comparison of the green and black curves in figure 5.1.1.3 (c) shows that the 95 nm wide × 200 nm pitch nanopillar array produces an extra peak in the extinction spectrum of P3HT:PCBM, at 657 nm, extending the absorption/scattering further into the red. A number of authors have suggested in the literature that such an effect alone might be sufficient to give rise to enhanced solar cell efficiency [7, 67, 71, 73, 74]. We next test this suggestion. Figure 5.1.1.4 shows a comparison of the extinction (green) and external quantum efficiency (EQE, red) spectra for 95 nm wide × 200 nm pitch and 180nm wide × 360 nm pitch nanopillar array-patterned devices. In each case spectra were also measured for control cells fabricated on the same samples, to eliminate possible variation of the performance due to the uncontrollable parameters that might affect the EQE measurements, including the morphology of the P3HT:PCBM, and electrical properties of interfaces. Each of the measured EQE spectra are normalized to the maximum value of EQE of the control cells on the same substrate or same batch. The control devices (5.1.1.4 (c) and (d), black curves) show higher efficiency than the nanopillar-patterned devices at wavelengths below ~ 640 nm, perhaps due to relatively low transmission though the nanopillar arrays in this range. Examination of the red curve in fig. 5.1.1.4 (c) shows that there is no peak in the EQE at 657 nm corresponding to that in the extinction. Interestingly, however, the 180 nm nanopillar patterned devices show *higher* efficiency from ~640nm to 720nm; we discuss this observation in detail in the following section. The extinction spectrum from these devices is monotonically increasing in this range, with an apparent peak in measured extinction at approximately 830 nm.

In summary, while extinction measurements do show enhanced absorption/ scattering in the red and near IR for P3HT:PCBM organic solar cells patterned with arrays of Au nanopillars, we find that, contrary to suggestions in the literature [7, 67, 71, 73, 74], this does not give rise to an overall increase in the external quantum efficiency of the devices.

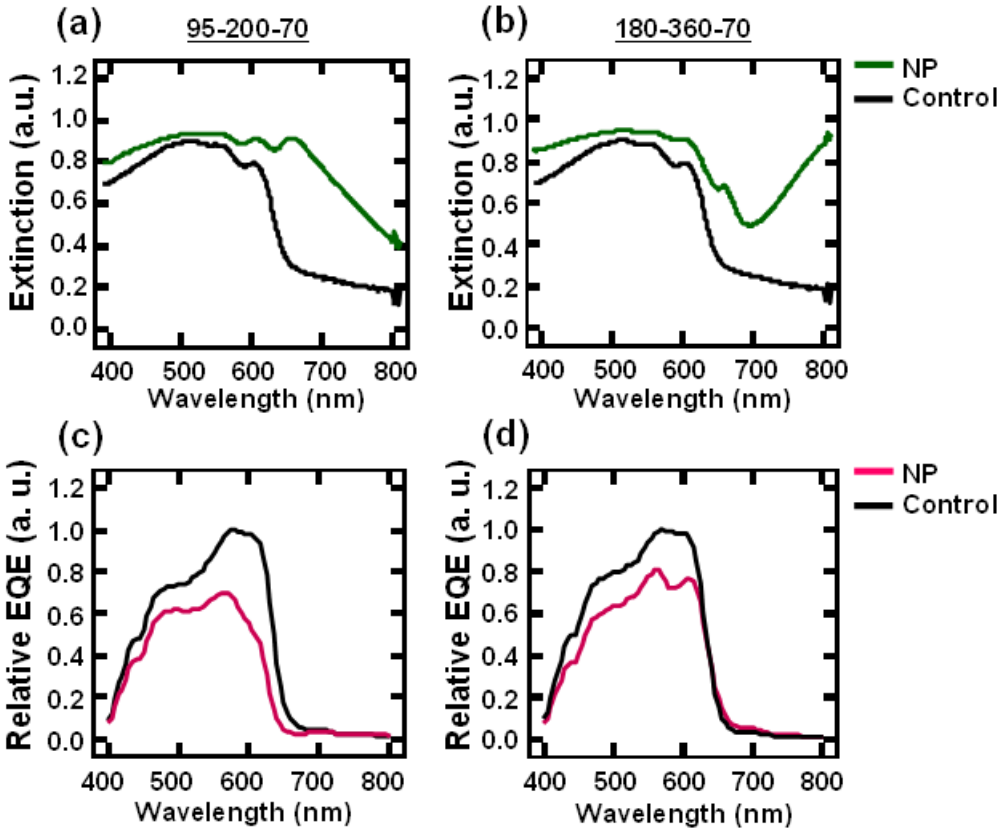

Figure 5.1.1.4 Comparison of (a), (b) optical extinction spectra and (c), (d) external quantum efficiency measurements vs optical wavelength for Au nanopillar-patterned (green, red) curves) and control (black curves) devices. Nanopillar widths, pitches, and height in nm are indicated at the top of each column. The measured EQE spectra are normalized by the maximum value of the EQE of the control cells in the same substrate or same batch.

5.1.2 Measured External Quantum Efficiency vs Calculated Absorbance and $|E|^2$

As pointed out in the last section, in spite of an extra peak in the measured extinction, we find no corresponding peak of enhanced photocurrent in the presence of Au nanopillar arrays. Based on our earlier results for enhanced fluorescence, we might expect better correspondence between the EQE and the near electric field-squared within the active layer. To test this we compared the measured EQE with a quantity that proportional to the near field squared that is proportional to the absorbance. The external quantum efficiency can be written as EQE (λ) = A(λ) × IQE (λ), where A(λ) is the absorbance of the photoactive layer at a given wavelength and IQE (λ) is the internal quantum efficiency. This latter quantity is related to the conversion of the absorbed photons into free carriers and their subsequent collection at the electrodes.[95]

We calculated A(λ) within the active layer for the NP-patterned and control devices, using the geometry and optical constants of the individual structures within each device. As a first step we determined the complex refractive index, $n+ik$, of ITO and P3HT:PCBM by spectroscopic variable angle ellipsometry as described in chapter 4. To obtain a more accurate value of k for the P3HT:PCBM layer (k_A), we measured the transmission spectrum for such a film on a glass substrate. We corrected for reflectance at the interfaces using n_A for P3HT:PCBM (determined ellipsometrically) and the known value of n for glass.[96] Optical constants for Au,[82] titanium oxide,[97] and Al[98] were taken from literature values. Although the DDA method allows us to calculate the extinction and E-field distribution of a

system, it requires us to represent the whole system as a set of small cubes, and thus has limitation on simulating large periodic arrays of particles. Therefore, for periodic structure, we instead used the finite difference time domain method (FDTD) to calculate the E-field distribution.

We calculate the calculated local field $E_A(x,y,z)$ which we obtained from 3-dimention finite-difference time-domain (FDTD), method with periodic boundary conditions [99-101], we next find the absorbed optical power per unit volume within the active layer. This is given by

$$Q_A(x,y,z) = \frac{2\pi c \varepsilon_o n_A k_A}{\lambda} \left| E_A(x,y,z) \right|^2, \tag{5.1.2.1}$$

The total intensity of the absorbed light in the active layer, I_{abs}^{A}, is given by integrating this over its volume:

$$I_{abs}^{A} = \iiint_{Layer} Q_A(x,y,z)\,dx\,dy\,dz\,. \tag{5.1.2.2}$$

Finally the absorbance $A(\lambda)$ is calculated by dividing this by the incident optical intensity $A(\lambda) = I_{abs}^{A} / I_{in}$.[102]

Example results of such calculations for devices with (red curves) and without (black curves) nanopillar arrays are shown in Fig. 5.1.2.1 (d) for 95 nm wide with pitch 200 nm, (e) for 180 nm wide with pitch 360 nm, and for 180 nm wide with pitch 540 nm. For a device with 95 nm width-pillars we use both square (Fig. 5.1.2.1 (d)) and cylindrical (Fig. 5.1.2.1 (g)) shapes for nanopillars in simulations. We do so because based on our SEM images, the smaller width pillars have rounded corners, and approximate square pillars less so than those with larger widths. The correspondence between the measured EQE (Fig. 5.1.2.1 (a)-(c)) and calculated

absorbance (Fig. 5.1.2.1 (d)-(g)) is visibly much better than between EQE and measured extinction. We find that all of the patterned cells show lower efficiencies than the control cells for optical wavelength less then approximately 625 nm, and the overall efficiencies of the high density NP cells are even lower than the low density NP cells. The strong correspondence to the local field squared, which is also reduced for the arrays suggests that the lower overall efficiency is related to a lower transmission.

The dashed lines in 5.1.2.1 indicate, however, a region of wavelength in which we observe enhancement in external quantum efficiency: from approximately 640 nm to approximately 720 nm. For wavelengths longer than 720 nm, the measured photocurrent we measure is very low, thus we are not able to distinguish the difference in EQE with and without nanopillars beyond this. The corresponding resonance which we discuss in more detail below is sensitive to the geometry of the NP array: it is absent for the 95 nm wide × 200 nm pitch NP array (fig. 5.1.2.1 (a)) but present for the 180 nm wide × 360 nm pitch and 180 nm wide × 540nm pitch arrays.

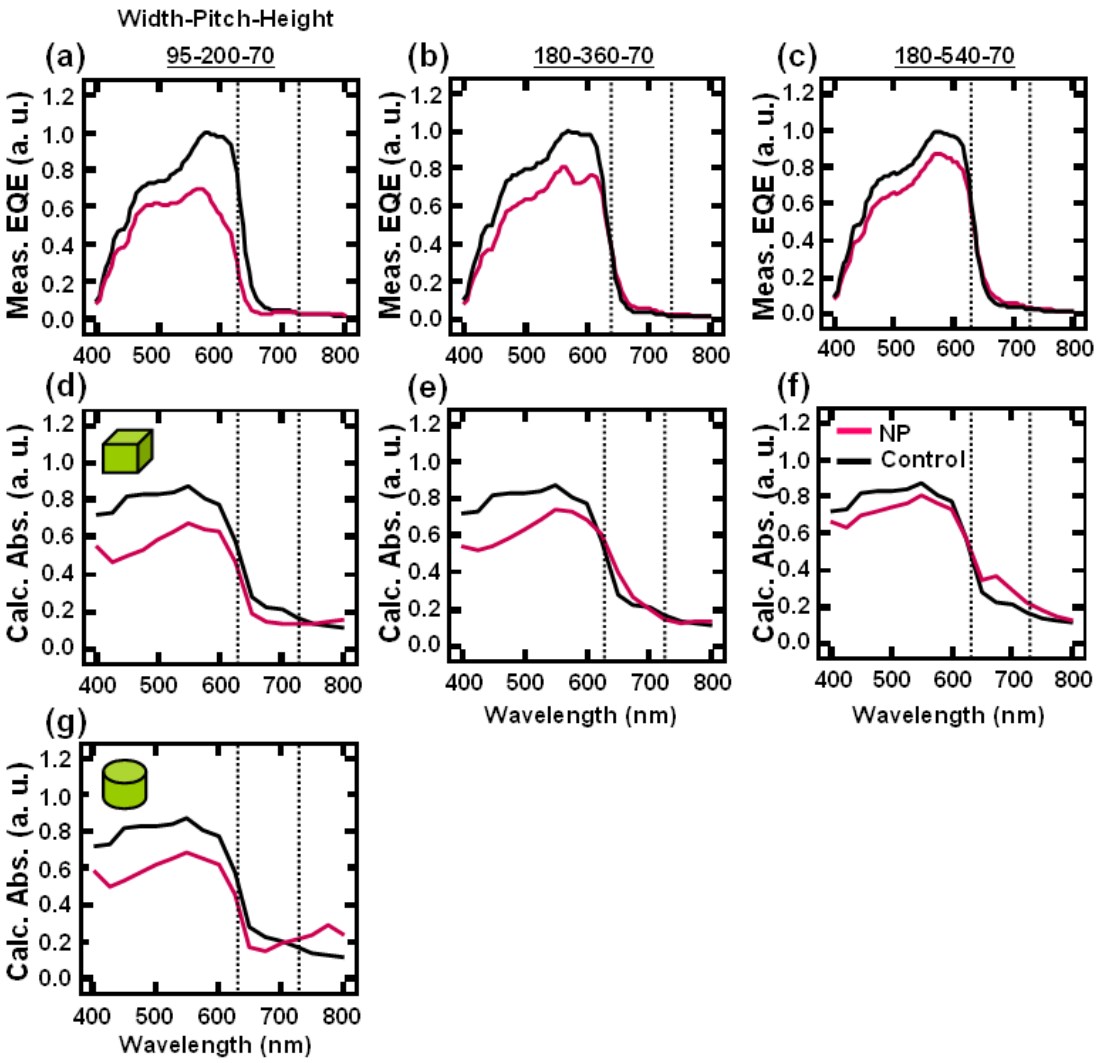

Figure 5.1.2.1 Comparison of measured external quantum efficiencies (a)-(c) and calculated active layer absorbance (d)-(g) for arrays with nanopillar 95 nm wide, spaced at 200 nm (a), (d), and (g); 180 nm wide, spaced at 360 nm (b), (e); 180 nm wide, spaced at 540 nm (c), (f). (d)-(f) Use rectangular shape and (g) use cylindrical shape for nanopillars in simulations. The color curves are for cells patterned with Au nanopillars, and the black curves are for control cells. The measured EQE spectra are normalized to the maximum value of the EQE of the control cells in the same substrate or same batch.

We next more closely examine the effect of the nanopillar arrays for a geometry in which we observe a band of enhanced efficiency. Figure 5.1.2.2 (a) and (b) show the measured EQE and calculated active layer absorbance at increased vertical scales for the device with 180 nm wide pillars with 540 nm pitch. In fig. 5.1.2.2 (c) we show the ratio of the field squared for NP-patterned device to that for the control device (black curve) as well as the ratio of the measured EQE for the NP-patterned device to that for the control device (blue curve). The insets in figure 5.1.2.2 (a) and (b) show at reduced vertical scale. The overall shapes of the calculated absorption spectra for the NP patterned and control devices between 400 nm and 800 nm are similar, with the control samples showing very slightly higher EQE below ~640 nm. As noted above, the calculated absorbance is enhanced in the nanopillar patterned device above ~640 nm, in qualitative agreement with the enhancement in the experimentally determined EQE in this range. The shapes of the simulated and experimental ratio curves, shown in Fig. 5.1.1.2(c), are similar; both show a peak at 675nm wavelength. Furthermore, the magnitude of enhancement at the peak agrees well in the two cases: we find 63 % and 60 % increases for the simulated absorption and measured EQE, respectively. To summarize: within a narrow range of wavelength: (1) the optical field enhancement occurs within the Au nanopillar arrays in the patterned devices, (2) this results in increased absorption within the bulk heterojunction organic layer, leading to (3) higher photocurrent. In contrast, near the peak of the measured EQE (i.e. λ ~575nm, inset Fig. 5.1.1.2(a)) our simulations (Fig.5.1.1.2 (b)) do not show strong field in the organic layer near the nanopillars.

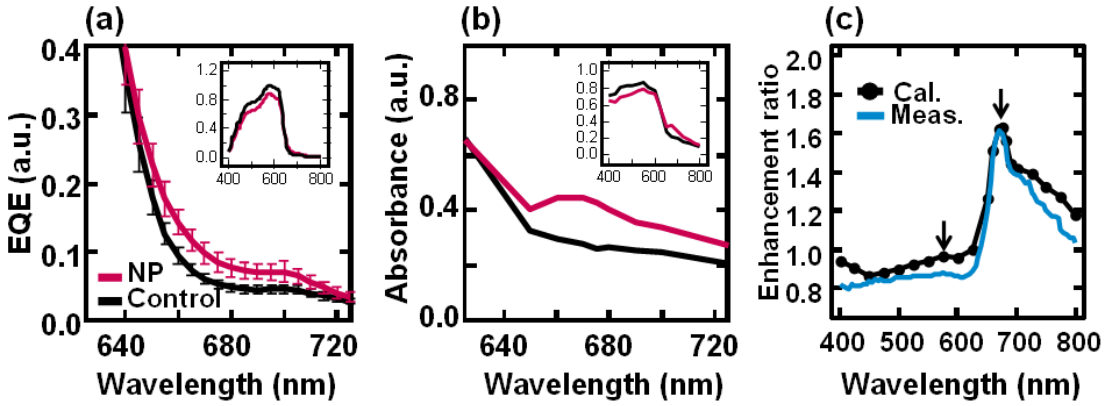

Figure 5.1.2.2 (a) Normalized external quantum efficiency (EQE) for the control cell (black curve) and nanopillar-patterned cell (red curve) measured under zero bias. In the patterned cell 180 nm wide 70 nm high Au pillars are spaced at 540 nm. (b) Calculated absorbance for control and patterned cells. (c) Ratios between measured EQE (blue curve) and simulated $|E|^2$ (black curve) for a nanopillar-patterned cell and those for a control cell.

As we now show, FDTD simulations of the near field-squared indicate that the resonance corresponding to the common peak in Fig. 5.1.1.2 (c) is of mixed nature. Figure 5.1.1.3(b) displays $|E|^2$ vs position for a cross-section of a 180 nm wide x 70nm high Au nanopillar for 675 nm wavelength incident radiation. Periodic boundary conditions are used corresponding to an array of such pillar with a 540 nm pitch. High field intensity occurs in two types of regions: at the corners of the nanopillars and further into the organic layer and substrate, in the form of intense cloverleaf-shaped lobes. The evanescent field associated with localized surface plasmons is generally very short range, and we suspected that the latter feature were due to a different effect. To test this, we show in fig. 5.1.1.3(c) the results of an additional FDTD simulation, in which we substitute for the dielectric function of the nanopillars values corresponding to Fe [103], for which the imaginary component dominates the real component. This effectively suppresses excitation of the localized particle plasmon, as evidenced by the absence of intense fields at the corners. The extended lobes however remain, suggesting that they are due to multiple reflections within the nano cavity formed by the nanopillars and the top electrode. Fig. 5.1.2.4 shows the results of increasing the thickness of the P3HT:PCBM layer, and thus the height of the cavity on the near field-squared. Fig. 5.1.2.4(a) and Fig. 5.1.2.4 (b) show $|E|^2$ integrated over the entire organic layer volume for Au and Fe nanopillars, respectively. In this case the lobes dominate the integration; the magnitudes are similar, and both show a red shift with increasing thickness. Fig. 5.1.2.4 (c) and Fig. 5.1.2.4 (d) show the result of integrating the $|E|^2$ over a narrow shell, 20 nm thick, around the nanopillars; again a red shift occurs for the Au case. In the case of the Fe

nanopillars is “very near-field squared” integration yields nearly, zero due to the suppression of the particle plasmon by the large imaginary component of the dielectric function.

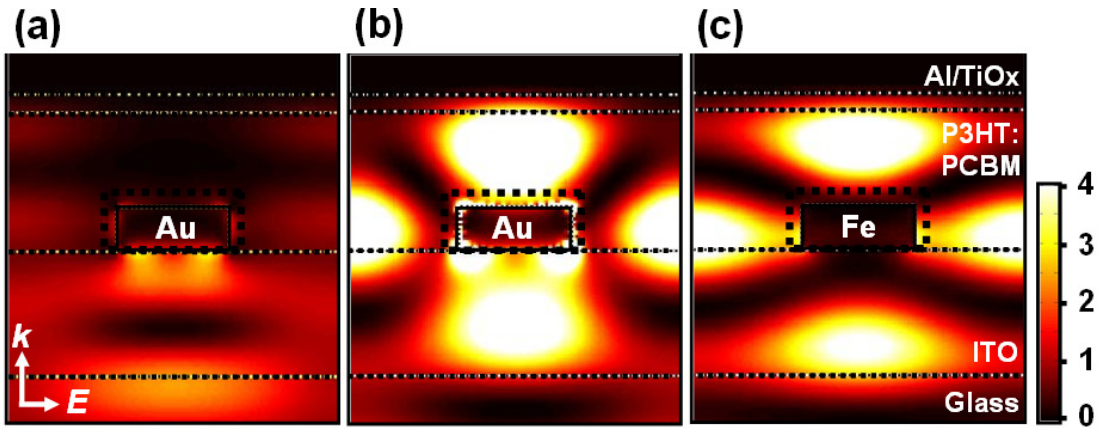

Figure 5.1.2.3 (a) Simulated $|E|^2$ image cutting though the center of Au nanopillar in patterned cell at peak of P3HT:PCBM absorption, but off resonance (575nm wavelength). (b) Corresponding image on resonance (675nm wavelength). (c) Simulated $|E|^2$ image cutting though the center of Fe nanopillar in patterned cell on resonance (675nm wavelength). Nanopillar dimensions are 180 nm width and 70 nm height. Periodic boundary conditions corresponding to an array pitch of 540 nm are used.

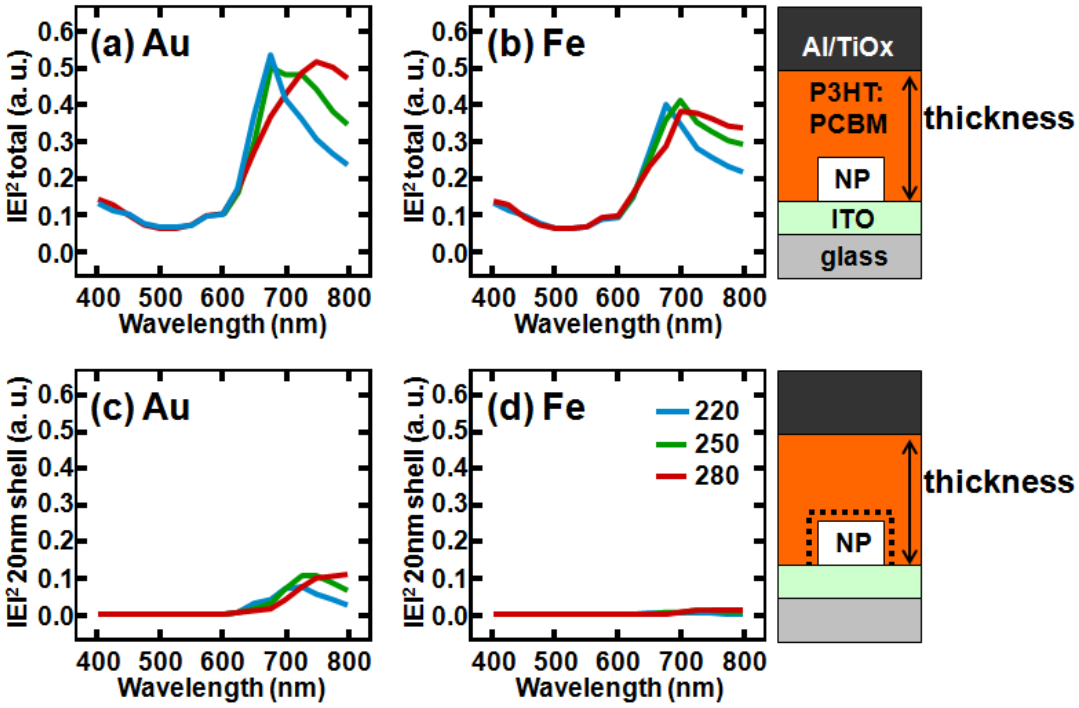

Figure 5.1.2.4 Near-field squared vs. very near-field squared. (a) $|E|^2$ integrated over volume of P3HT:PCBM layer for Au NP-patterned cell. For this and following panels: nanopillar widths are 180nm, pitch is 540nm, and heights are 70nm, illumination is at 675 nm wavelength at normal incidence, blue curve is for a P3HT:PCBM layer thickness of 220 nm, green curve for 250 nm and red curve for 280 nm. (b) $|E|^2$ integrated over volume of P3HT:PCBM layer for Fe NP-patterned cell illuminated with 675 nm wavelength light at normal incidence. (c) $|E|^2$ integrated over the volume of a 20 nm wide shell around an Au NP. (d) $|E|^2$ integrated over the volume of a 20 nm wide shell around a Fe NP.

In the organic solar cell literature, many reports to date are of simple absorption (without present of electrodes or full materials) and external quantum efficiency (EQE) measurement.[67-74] However, the absorption spectrum of the device is expected to be considerably different in the presence of electrodes, due to reflectance at the interfaces and interference effects. To explore the effect of Al electrode in comparison of absorbance and the solar cell efficiency, we calculated the $|E|^2$ spectrum for both the patterned and control cells, both with and without Al layer. Figure 5.1.2.4 (a) show the $|E|^2$ integrated over volume of P3HT:PCBM layer and $|E|^2$ integrated over 20 nm shell for an Au nanopillar patterned cell without presence of Al layer. The nanopillar width is 180 nm, height is 70 nm, and pitch is 540 nm. The volume-integrated $|E|^2$ intensity increases monotonically for the patterned cell without the Al layer as the wavelength is increased from 600 nm to 800 nm both for integration over the active layer volume and over a narrow shell. While the $|E|^2$ intensities (5.1.2.4 (b)) show peaks at 675 nm integration over the volume of the P3HT:PCBM layer, and at 700 nm for integration over a 20 nm shell with the Al layer. The insets in figure 5.1.2.4 display calculated $|E|^2$ images for a cross-section of a nanopillar for 675 nm/800 nm wavelength incident radiation for the cells with and without the Al layer. The field intensity and distributions change qualitatively of the layer is absent. The lobe of high $|E|^2$ between the nanopillars and Al layer is absent for 675 nm wavelength in the absence of the Al layer. The near field-squared shows intense lobes between nanopillars in the absence of an Al layer for 800 nm illumination; these shift toward the ITO side in the presence of Al layer. The Al layer clearly shows a strong effect on the in $|E|^2$ for both the Au patterned and non-pattern

cells, and thus should not be ignored in the measurement and calculation to estimate the performance of the solar cells.

To summarize, the above discussion demonstrates an effect of the back electrode in the performance of organic solar cell with Au nanopillar arrays, which ofen ignored [7, 67-75]. Diffraction from the nanopillars and multilayer interference cause an enhanced field at 675 nm; plasmon excitation in the nanopillars results in a further increase in the very near region. The $|E|^2$ distribution for arrays of nanopillars in a functional device will be different compared to that for the free standing nanoparticles due to these diffraction and interference effects.

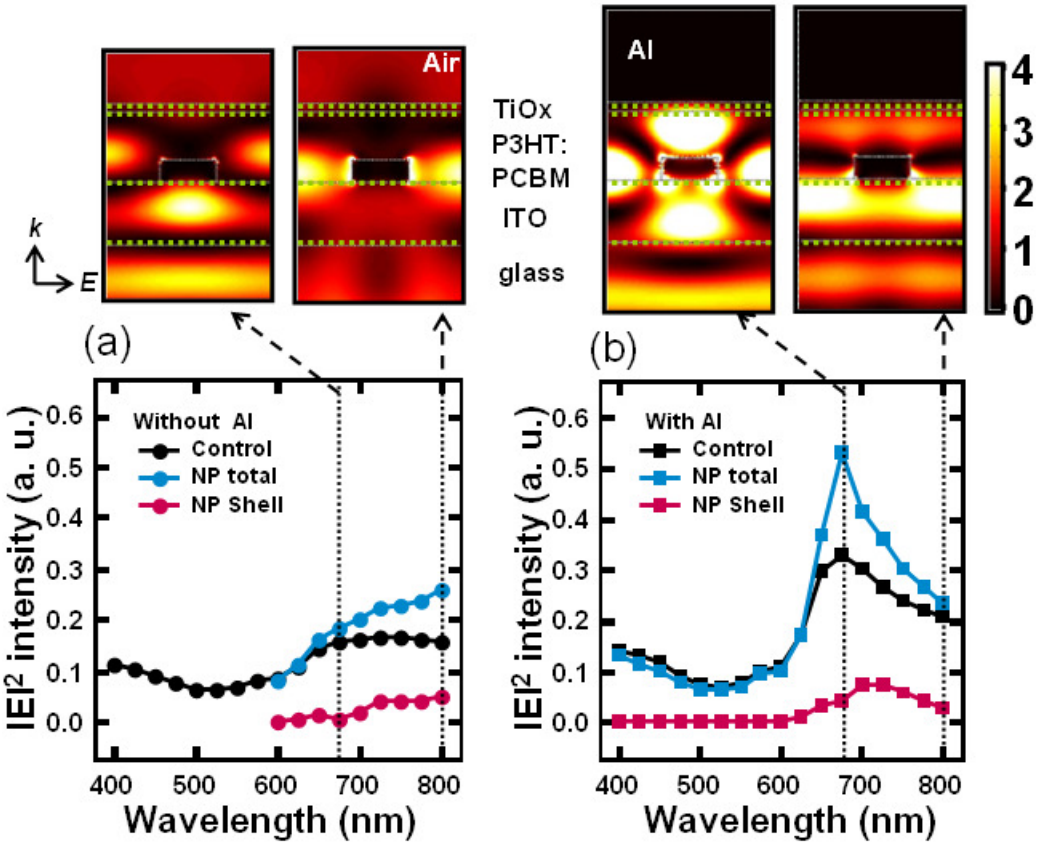

Figure 5.1.2.4 (a) Calculated $|E|^2$ for cells without the Al layers. Shown in blue is $|E|^2$ integrated over the volume of P3HT:PCBM layer for Au NP-patterned cell with nanopillar edge length 180nm, pitch 540nm, height 70nm, and P3HT:PCBM thickness 220 nm. Red curve is $|E|^2$ integrated over the volume of a 20 nm thick shell around an Au NP within the P3HT:PCBM layer. The black curve shows the $|E|^2$ integrated over the volume of P3HT:PCBM layer for the control cell. (b) The corresponding $|E|^2$ integrations for the NP-patterned (blue and red) and control cells, including 300 nm thick Al layers. The inserts are simulated $|E|^2$ images cutting though the center of Au nanopillar in patterned cell at 675 nm (left) and 800 nm (right) optical wavelengths at normal incident with/ without the Al layers.

5.1.3 Nanopillar Spacing vs Measured External Quantum Efficiency and Calculated Absorbance

In this section we explore how the pitch of the Au nanopillar arrays affects the performance of the organic solar cells. For nanopillars of 180 nm wide and 70 nm high we fabricated arrays in which the pitch varies from 300 nm to 540 nm. Figure 5.1.3.1 shows a side by side comparison of the measured EQE (5.1.3.1 (a)-(c)) and calculated absorbance (5.1.3.1 (e)-(g)). The measured EQE and calculated absorbance for the pitch at 360 nm were shown in figure 5.1.2.1 (b) and (e), respectively. These measured EQE and calculated absorbance spectra are again qualitatively in agreement. Except for the minimum pitch at 300 nm, all of them show enhancement in the narrow range of wavelength approximately 625 nm to 725 nm, where the P3HT:PCBM absorbs weakly. The insets in the fig. 5.1.3.1 (e)-(g) are simulated $|E|^2$ images cutting though the center of the Au nanopillar in patterned cell within the enhancement region (675nm wavelength). The $|E|^2$ distributions evolves strongly as the pitch is varied. From the previously discussion the resonance observed for a pitch 540 nm at 675 nm illumination contains contributions from optical interference and localized surface plasmons. To understand how these contributions are affected by the pitch of the array, we again compared the near-field squared and very near-field squared. For the near field squared, we integrated $|E|^2$ over the volume of P3HT:PCBM layer (fig. 5.1.3.2 (a), blue curves) and over volume of a 20 nm thick shell (fig. 5.1.3.2 (a), red curves) for a unit patterned cells. The very near-field squared, i. e. $|E|^2$ integrated over 20 nm shell shows a variation compared to the intensities of as pitch increased from 300 nm to 720 nm with local maxima of

the $|E|^2$ intensities for pitch at ~ 480 nm and at 600 nm. Fig. 5.1.3.2 (a) is for the integrated $|E|^2$ over a unit cell divided by the area of the unit cell; it shows a peak of at pitch 540 nm. The $|E|^2$ intensity in 20 nm shell is not the local maximum at this wavelength. The results show that the peak of $|E|^2$ integrated over the active layer volume is not necessarily at the peak of $|E|^2$ from plasmons. The nanocavity interference intensity is larger, and can dominate the $|E|^2$ intensity for devices consisting of nanopillar arrays.

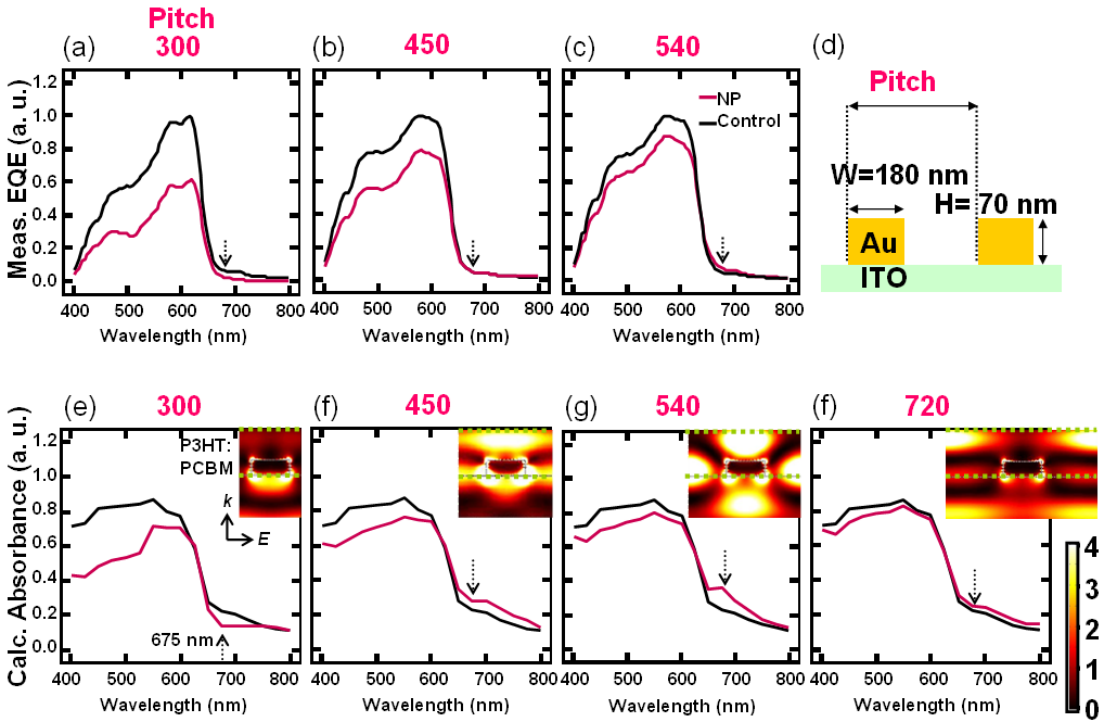

Figure 5.1.3.1 (a)-(c) are measured EQE and (e)-(h) are calculated absorbance for the for the devices with and without nanopillar arrays. The pitches of the nanopillar arrays are varied from 300 nm to 720 nm. (d) The configuration of the system. The insets are the $|E|^2$ images of the active layer (dashed lines) and ITO cutting though the

center of the particles in patterned cells at incident wavelength 675 nm for a series of periods.

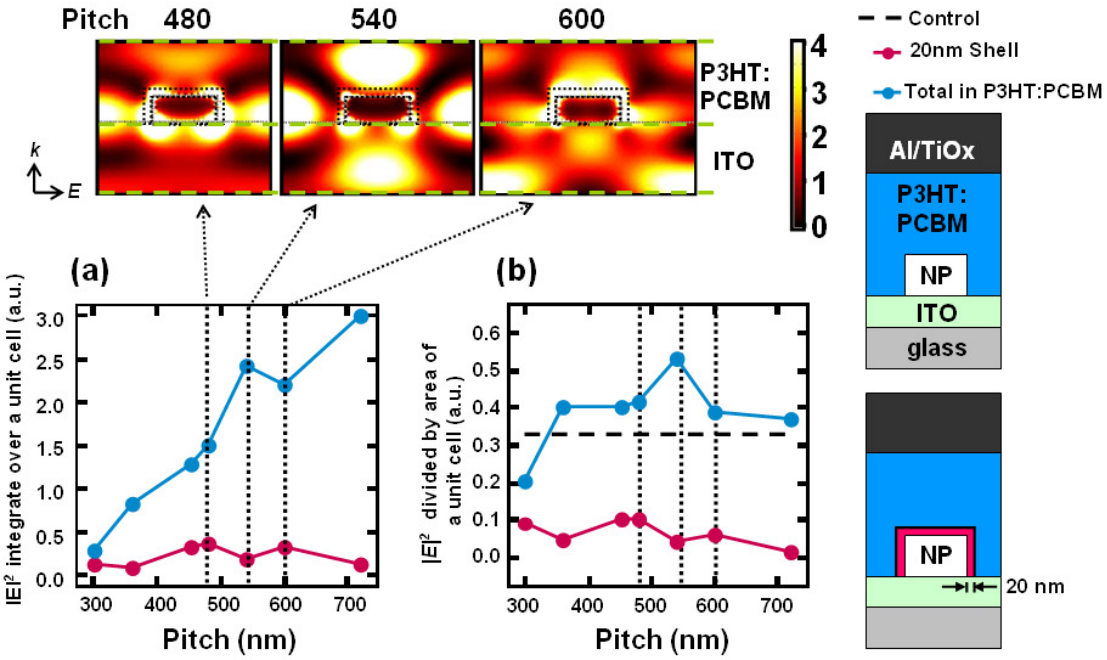

Figure 5.1.3.2 Blue curve shows $|E|^2$ integrated over volume of P3HT:PCBM layer for a Au NP-patterned cell with varied pitch. Red curve is $|E|^2$ integrated over volume of a 20 nm wide shell around an Au NP in P3HT:PCBM. Both of the curves are normalized by the device area. The nanopillar width is 180nm and height is 70nm, illumination is at 675 nm wavelength at normal incidence.

5.1.4 Effect of Extinction Coefficient k_A of the Active Layer on Absorbance and $|E|^2$

Our measured EQE and calculated absorbance reveal a resonance case for patterned with Au nanopillar arrays of width 180 nm, height 70 nm, and pitch 540 nm under illumination at 675 nm and normal incidence. An interesting possibility is seemingly that by tuning the peak in the wavelength dependence of the local field from nanopillars to coincide with the peak of absorbance of the absorbing layer it might be possible to further increase the overall efficiency.

We checked this indirectly, instead increasing the attenuation coefficient of the active layer at 675 nm, i. e. the wavelength corresponding to the plasmon resonance, and calculating the absorbance of the active layer with and without NPs. Fig. 5.1.4.1 shows the results, with k_A varying from 0 to 0.8, bracketing the measured value of 0.03. Example $|E|^2$ images at a series of increasing values of k_A are shown in figure 5.1.4.1 (a); for larger k_A the high field squared near the nanopillars is visibly suppressed by the higher attenuation within the active layer. Interestingly, the difference between the calculated absorbance within the active layer with and without nanopillars, shown in Fig. 5.1.4.1 (c), reaches a maximum at a value of k_A ~0.03, which is coincidently equal to our measured value for P3HT:PCBM. (Although the ratio of the absorbance with and without nanopillars, shown in the inset of fig. 5.1.4.1 (c) decreases monotonically with increasing k_A.) For further increases in k_A beyond this, the enhancement decreases, and for k_A larger than ~0.2 the absorbance in the active layer of the control cell exceeds that of the NP-patterned cell. Our calculations thus seemingly indicate that k_A is already close to optimum for maximum

enhancement of absorption from a gold nanopillar array of the dimensions studied here.

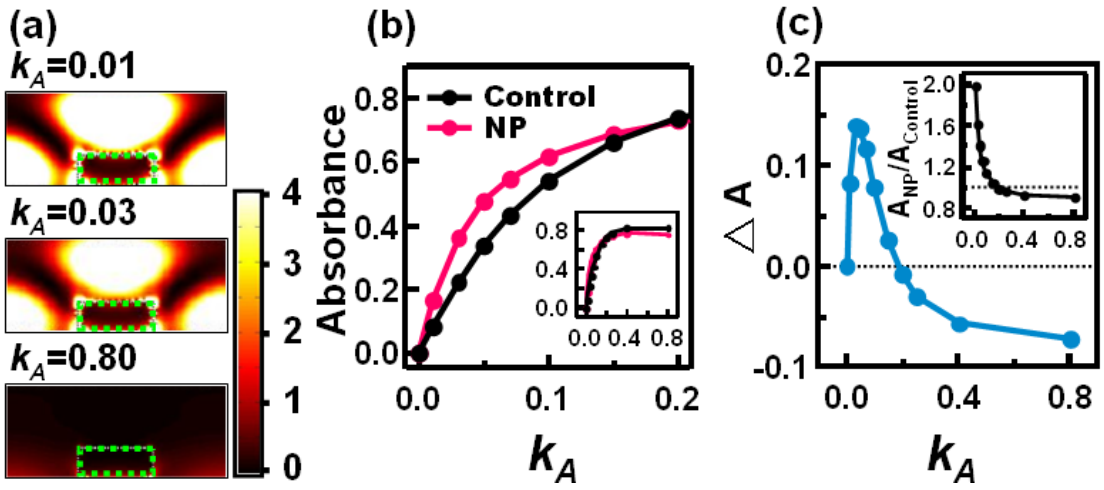

Figure 5.1.4.1 (a) $|E|^2$ images cutting though the center of the Au nanopillars (dashed squares) in patterned cells at a series of increasing values of active layer attenuation coefficients k_A. Au nanopillars in these calculations are 180 nm in width, 70 nm in height, and spaced at 540 nm. (b) Calculated absorbance by the active layer with (pink curve) and without (black curve) NPs, as function of attenuation coefficient (k_A) at an incident wavelength of 675nm. (c) Difference between absorbance of the patterned cell and that of the control cell. Inset shows the ratio of the calculated absorbance within the active layer of the NP-patterned cell to that of the control cell.

The observation in fig. 5.1.4.1 of the suppression of field intensity contribution from localized surface plasmon and interference at the resonance case suggests an explanation as to why there is no enhancement below the 625 nm incident wavelength. A possible reason for this might be due to the increasing attenuation coefficients of the P3HT:PCBM (k_A > 0.13) below this wavelength resulting in a suppression of the field associated with the resonance. To test this idea, we carried out further simulations to calculate the enhancement ratio of the active layer for the An NP-patterned cell to that for the control cell, but using a lower k_A at shorter wavelength, 550 nm. Figure 5.1.4.2 (a)-(d) show the calculated field square using the measured value of k_A for P3HT:PCBM and for 180 nm wide pillars with pitch varied from 300 nm to 540 nm. The ratio of absorbance with and without nanopillars is lower than 1 in each case, decreasing as the pitch is decreased. In contrast, substituting a much lower value for k_A (figure 5.1.4.2 (e)-(h)), results in a equal or larger than one. We thus would expect to observe increased field from excitation of the resonance when the k_A is low. This supports the suggestion posed above, i.e. that the high field associated with the plasmon/cavity interference resonance would be suppressed by the relatively high value of the active layer attenuation coefficient k_A in the region where it absorbs strongly, i.e. from 400 nm – 640 nm.

Next we consider the effect of the transmission though our Au nanopillar arrays. Although in the range of widths and pitches we explore here geometrical shadowing is not expected to give a quantitative description of the transmission [104] show below that it gives a rough approximation to the apparent transmission. The luck of no electromagnetic field enhancement at the shorter wavelength region (400 nm~ 640

nm) in our devices, along with a limited transmission though the nanopillar arrays seem to explain why the overall performance of Au NP-patterned devices we fabricated didn't show enhancement in EQE. Figure 5.1.4.3 shows a summary plot of the ratio of the calculated photocurrent for NP-patterned cells to that for the control cell illuminated under AM 1.5 G condition with total power density 100 mW/cm^2 as a function of the area fraction of the cell not covered by nanopillars. To calculated the photocurrent, we multiplied the absorbance $A(\lambda)$ with photon flux of the AM 1.5 G solar spectrum from solar irradiation and then integrated over 400 nm to 800 nm optical wavelength. Finally the photocurrent is obtained by dividing the integration by the Coulomb for an electron. In this calculation we assumed one absorbed photon is converted into one electron, i. e. no recombination losses, and the calculated short circuit photocurrent of the control cell with P3HT:PCBM thickness at 220 nm is 13.51 mA/cm^2, which is comparable to the literature calculated value, ~13 mA/cm^2 [105]. It is interesting to note that for most of the results shown in figure 5.1.4.3 most of the NP-patterned arrays show higher relative efficiency than for a simple geometrical shadowing (i.e. area fraction) model, shown by the black dashed curve. This might be due to extraordinary transmission effects [104], or to nanocavity interference within the active layer. However, in each case the relative efficiency is less than one, i.e. the unpatterned control cells are equally or more efficient than those with NP arrays.

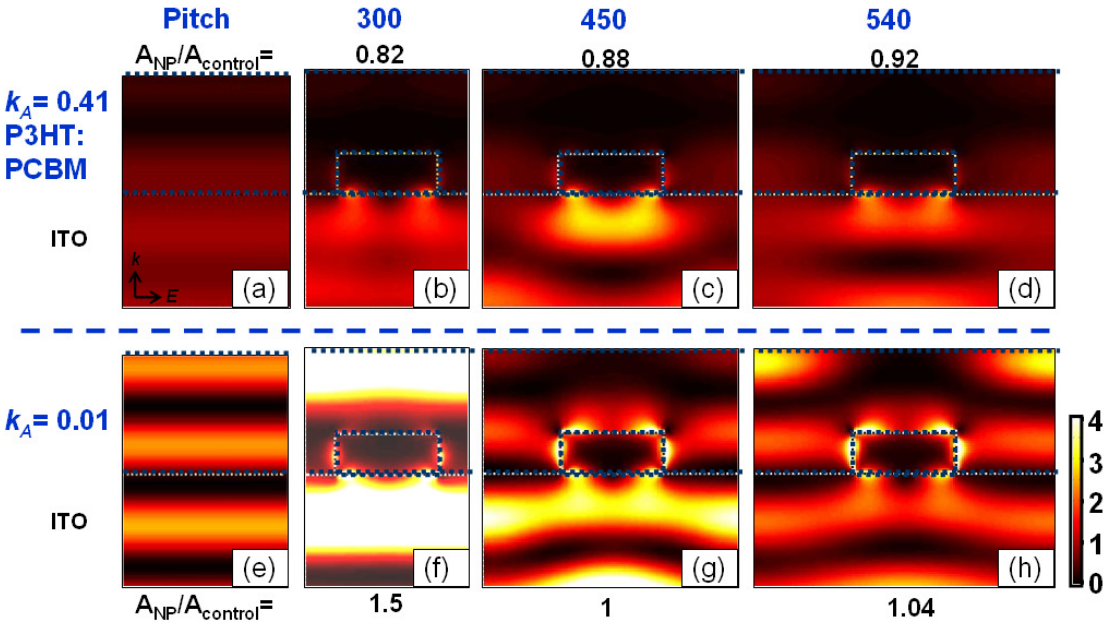

Figure 5.1.4.2 (a)-(d) $|E|^2$ images of the active layer of a device cutting though the center of the nanopillars (dashed squares) in patterned cells with k_A = 0.41, the value for P3HT:PCBM at 550 nm irradiation under normal incidence. (e)-(h) are for k_A = 0.01. (a) and (e) are $|E|^2$ images for control cells, and others are for Au NP-patterned cells with width = 180 nm, height = 70 nm, and pitch = 300 nm, 450 nm to 540 nm second, third, and fourth columns from the left.

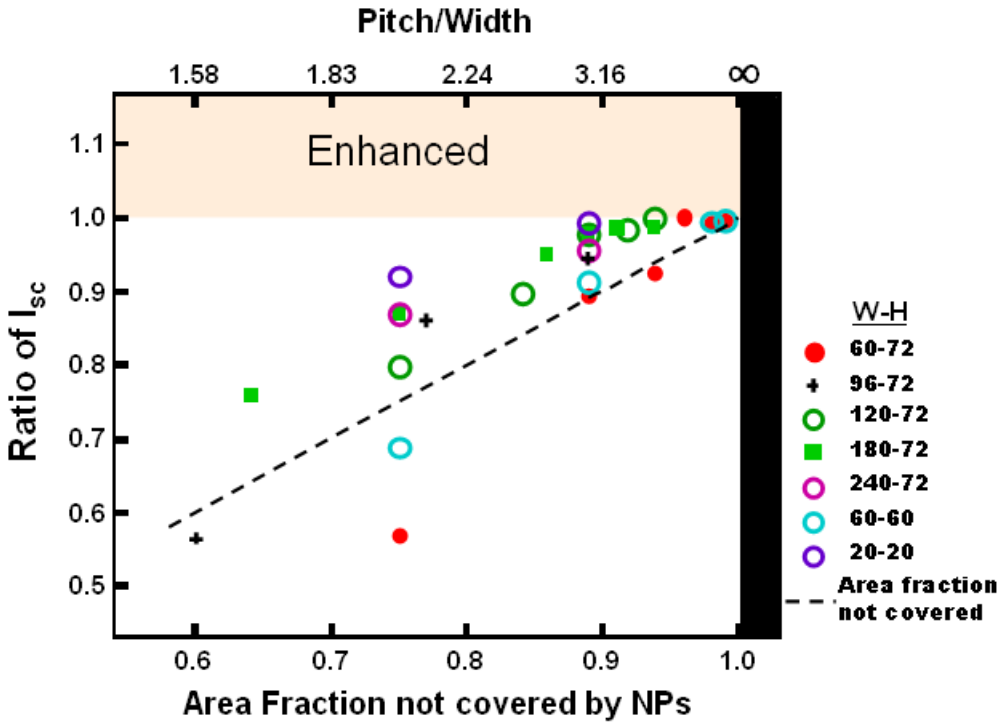

Figure 5.1.4.3 Calculated results of the ratio of short circuit photocurrent of the Au patterned cells to the control cell under AM 1.5 G condition vs uncover Au patterned area (or pitch/width ratio) for varying pillar width/height combination. The calculated short circuit current density (Jsc) for the control cell under illumination at 100 mW/cm^2 (AM 1.5 G) is 13.51mA/cm^2

5.1.5 Where Does the Extra Absorbed/Scattered Light Go?

As shown above in fig. 5.1.1.5 (a) we observe an increase in optical extinction, i.e. absorption plus scattering, in the presence of arrays of Au nanopillars at incident radiation 657 nm for pillar width 95 nm, height 70 nm, and pitch 200 nm. We now consider the obvious question: where does energy associated with this extra extinction go? There are at least three possibilities, which we discuss below.

The first possibility suggested by other authors in the literatures [7, 67, 71, 73, 74] was that it might go to increasing the solar cell efficiency. We find that this is not the case, as shown above. The measured EQE (fig. 5.1.1.5 (c)) shows no corresponding enhancement.

A second possibility is that increased absorption gives rise to increased radiative loss. We tested this idea by measuring the fluorescence of P3HT:PCBM from the combinatoral width/pitch particle arrays, using a scanning laser microscope with an incident wavelength of 633 nm. The sample is patterned with Au nanopillar arrays whose width varies from 75 nm to 400 nm and whose pitch varies from 130 nm to 1200 nm. The areas patterned with width/pitch = 75 nm/200 nm, 110 nm/200 nm, and 95 nm/180 nm show about same (75 nm/200 nm) or lower fluorescence intensity (110 nm/200 nm and 95 nm/180 nm) than the intensity of a control region without pillars (figure 5.1.5.1). The results show that there is no significant fluorescence enhancement from the nanopillar arrays whose dimensions bracket those for which we see the peak in the extinction at a near by extinction wavelength. This is consistent with the report in the literature [106] that the photoluminescence quantum yield for the blend of P3HT:PCBM with weight ratio 1:1 is very low, $<1\%$. The possibility

that the "extra" energy, absorbed/scattered, is lost to the process of photoluminescence can seemingly thus be ruled out.

The last possibility is that the energy is dissipated by heat. Based on Mie Theory, for smaller particles the extinction should dominated by the absorption within the particles. We now consider how much of the power absorbed by the nanopillars in our arrays goes to Joule heating.

To calculate the Joule heating due to absorbance by the Au nanopillar arrays, we recall the complex Poynting vector theorem, from which the time-average Ohmic loss [107] is expressed as

$$P(\lambda) = \frac{1}{2}\iiint \sigma(\lambda)\left|E(x,y,z)\right|^2 dxdydz \qquad (5.1.5.1)$$

, where σ is the conductivity, $\left|E(x,y,z)\right|^2$ is the local electrical field intensity within the Au nanopillars. From the relationship between the complex permittivity, ε_r, and the complex refractive index, $n + ik$, we know that [27]

$$\varepsilon_r = (1+\chi) + i\frac{\sigma}{\omega\varepsilon_0} = (n^2 - k^2) + i2nk \qquad (5.1.5.2)$$

Thus, the conductivity can be expressed as $\sigma = 2nk\omega\varepsilon_0 = 4\pi nkc\varepsilon_0/\lambda$. We obtain the local field within the Au nanopillars $E_{Au}(x,y,z)$ by calculation, using the 3-dimention finite-difference time-domain (FDTD) method, with periodic boundary condition [99-101]. Substituting the resulting expression for the conductivity into (5.1.5.1), the Ohmic loss in Au nanopillars can be calculated by

$$P(\lambda) = \iiint 2\pi nkc\varepsilon_0\left|E(x,y,z)\right|^2/\lambda\, dxdydz \qquad (5.1.5.3)$$

Finally the heating absorbance, $A_h(\lambda)$, is calculated by dividing $P(\lambda)$ by the incident optical intensity $A_h(\lambda) = P(\lambda) / I_{in}$.

Figure 5.1.5.2 shows a side by side comparison of (a) the extinction spectrum after depositing P3HT:PCBM for arrays of Au nanopillars which are 95 nm in width and (b)-(c) calculated corresponding heating absorbance (red curves in (b) and (c)) and total absorbance (blue curves in (b) and (c), i.e. absorbance of P3HT:PCBM plus heating absorbance of Au). The green curves in fig. 5.1.5.2 (a) show spectra for the samples with nanopillars and the black curves in fig. 5.1.5.2 (a)-(c) are for the control sample without patterned nanopillars. Note that in the measured extinction spectra of fig. 5.1.5.2 (a), the back electrode (30 nm thick TiOx plus 300 nm thick Al) is absent, while in the calculation (fig. 5.1.5.2 (b), (c)) it is included. The difference between fig. 5.1.5.2 (b) and (c) is that we use rectangular-shaped (95 nm in width) Au nanopillars in (b) and cylindrical-shaped pillars (95 nm in width) in (c). The shape of our 95 nm wide nanopillars is somewhere between rectangular and cylindrical due to corner rounding corresponding to proximity effect in the lithography. Our calculation shows that near the peak of extinction (657 nm), the heating absorbance increases (red curves in fig. 5.1.5.2 (b) for rectangular and in fig. 5.1.5.2 (c) for cylindrical nanopillars).

We next estimate how much the solar power would be transfered into heat for arrays of 95 nm wide and 70 nm high Au nanopillar arrays with 200 nm pitch in a BHJ OPV solar cell device. For this, we calculate the total power density of this heat by multiplying the absorbance for rectangular Au nanopillars (fig. 5.1.5.3 , red curves) and solar power density (fig. 5.1.5.3, black curves), and then integrate over the solar

spectrum; including only calculated the absorbance from 400 nm to 800 nm wavelength, the power lost to the joule heating is 23.57 mW/cm^2 under AM 1.5G 100 mW/cm^2 illumination within this band of wavelengths.

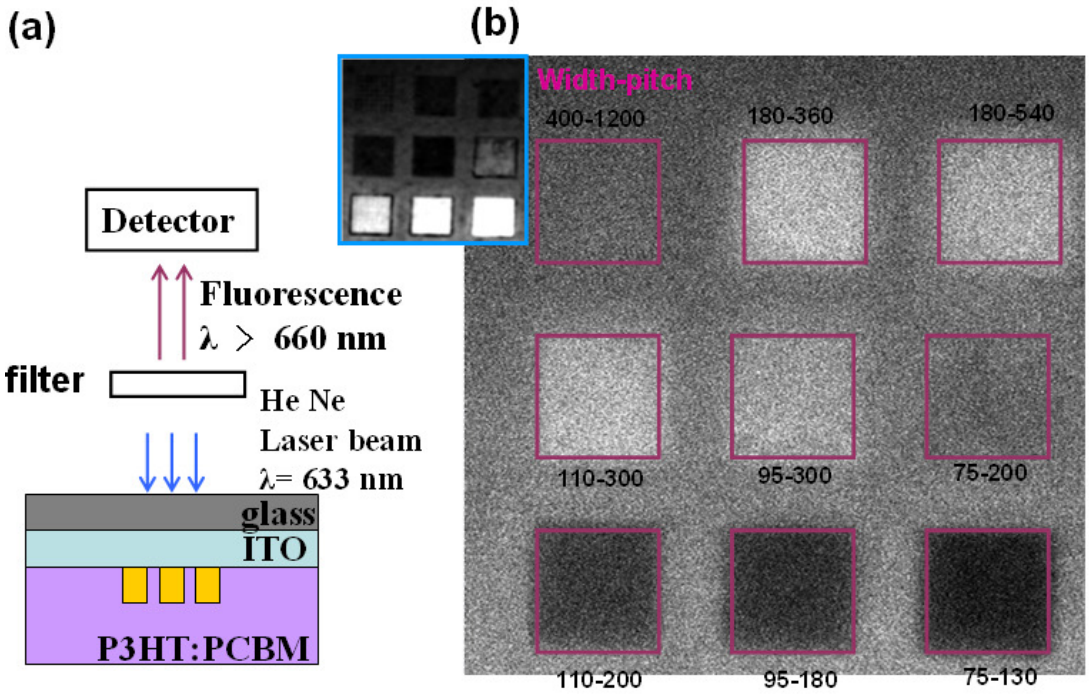

Figure 5.1.5.1 (a) System set up for fluorescence measurement using laser scanning microscope. (b) Measured fluorescence image of P3HT:PCBM at an excitation wavelength 633 nm with different cells containing nanopillar arrays. The red squares indicate the borders of the arrays, and the width and pitch labeled on the outer borders of the squares. The inset in (b) is the reflectance image of the same arrays.

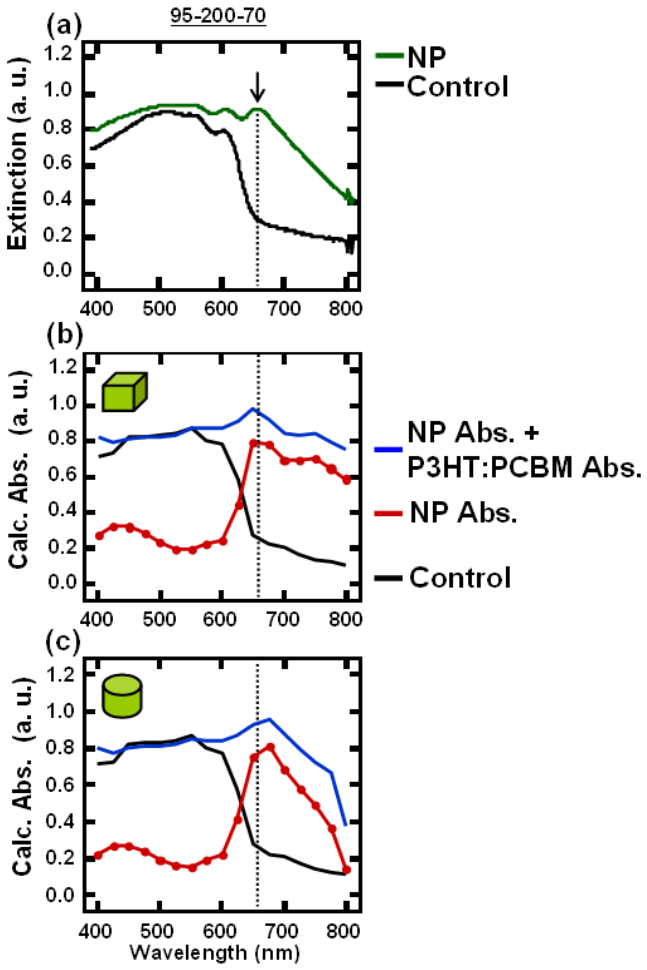

Figure 5.1.5.2 Comparison of measured optical extinction and calculated absorption for Au-NP and control cells. (a) Measured extinction for a NP-patterned cell, with nanopillar width = 95 nm, height = 70 nm, and pitch = 200 nm (green curve), and for a control cell (black). (b) Calculated heating absorbance of the solar cell devices in the square Au nanopillar arrays (red) and sum of the calculated absorbance in Au nanopillars and in the active layer (blue). The black curve is the calculated absorbance of P3HT:PCBM in the control cell. (c) Calculated absorbance of the solar cell devices in cylindrical Au nanopillar arrays (red), and sum of absorbance in Au nanopillars and in the active layer (blue). Nanopillar diameter = 95 nm, height = 70 nm, and pitch = 200 nm.

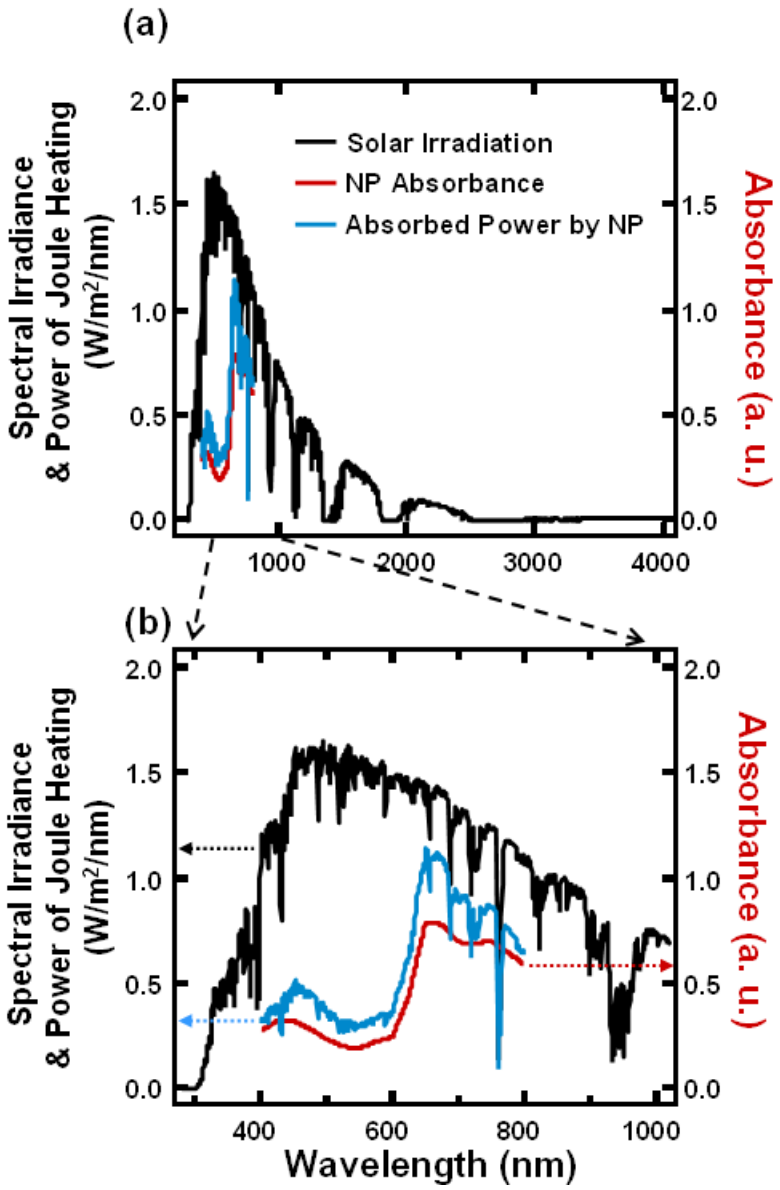

Figure 5.1.5.3 (a) Calculated estimation of Joule heating power density (blue curve) for a square Au nanopillar array, in a P3HT:PCBM BHJ solar cell device under illumination of solar irradiance at AM 1.5 G with total power 100 mW/cm^2. (Red curve) Calculated nanopillar absorbance. (Black curve) Solar spectrum. The width, height, and pitch of the Au nanopillars are 95 nm, 70 nm, and 200 nm. (b) Replot of individual curves over a narrower range of wavelengths.

We end this section with a summary of the performance of P3HT:PCBM BHJ organic solar cells patterned with Au nanopillar arrays in the region of incident wavelength from approximately 400 nm to 800 nm. The ratios of the measured EQEs and that of the calculated absorbances with Au nanopillar array for various nanopillar widths, square/cylindrical shapes, and pitches are shown in figure 5.1.5.4. In each case, there is no significant enhancement in the wavelength region beneath (approximately 625 nm) because of suppression of the field generated by particle plasmons and interference within the device nanocavity by the attenuation coefficient k_A of the active layer. We find that efficiencies in this region of wavelength are reduced by an amount approximately proportional to the nanopillars' coverage. For most of the devices with 180 nm wide pillar arrays, the reduction of the measured EQE and calculated absorbance is approximately equal to the area fraction covered by nanopillars, indicated by the dot lines in each plot. For the 180 nm wide, larger pitch arrays, longer wavelengths where the k_A is small, we observed enhancement in both measured EQE and calculated absorbance in a narrow band, and the enhancements are contributed from both plasmonic and interferenced electrical field square. For device patterned with pillars of width 95 nm and pitch varying from 150 nm to 300 nm, both the measured EQE (fig. 5.1.5.4 (e)-(j)) and calculated absorbance (fig. 5.1.5.4 (e)-(f) show dips between 600 nm~ 700nm wavelength, approximately coincident with the wavelength of the peaks in the measured extinction spectra: The peaks for P= 150 nm and 200 nm is located at 650 nm and 657 nm, respectively, after coating P3HT:PCBM. We did not measure the extinction for P= 300 nm coating with P3HT:PCBM, but extrapolating linearly (as suggested by fig. 5.1.1.2 (d), blue curve)

would give a position of 671 nm. The wavelength at which the dip occurs for calculated ratios of absorbance using cylindrically shaped for nanopillars show better agreement with those in the EQE ratios than those calculated using a square shape. In addition the calculated peaks in the extinction from the 95 nm diameter cylindrical nanopillar arrays on ITO-coated glass substrates, with pitch 150 nm and 300 nm also show better agreement in peak position (625 nm for both P= 150 nm and P= 300 nm) with the measured extinction (at 596 nm and 602 nm for P= 150 nm and P= 300 nm). Our previous calculations suggest that the dips seen in the ratio plots of fig. 5.1.5.4 result from an increase in absorption in Au nanopillars due to excitation of localized surface plasmon resonances, and that the energy is dissipated by heat. From figure 5.1.5.4 (e)-(j), at longer wavelengths, beyond approximately 750 nm, the measured EQE ratio and calculated absorbance ratio show poor agreement. This might be due to very small measured photocurrents beyond this.

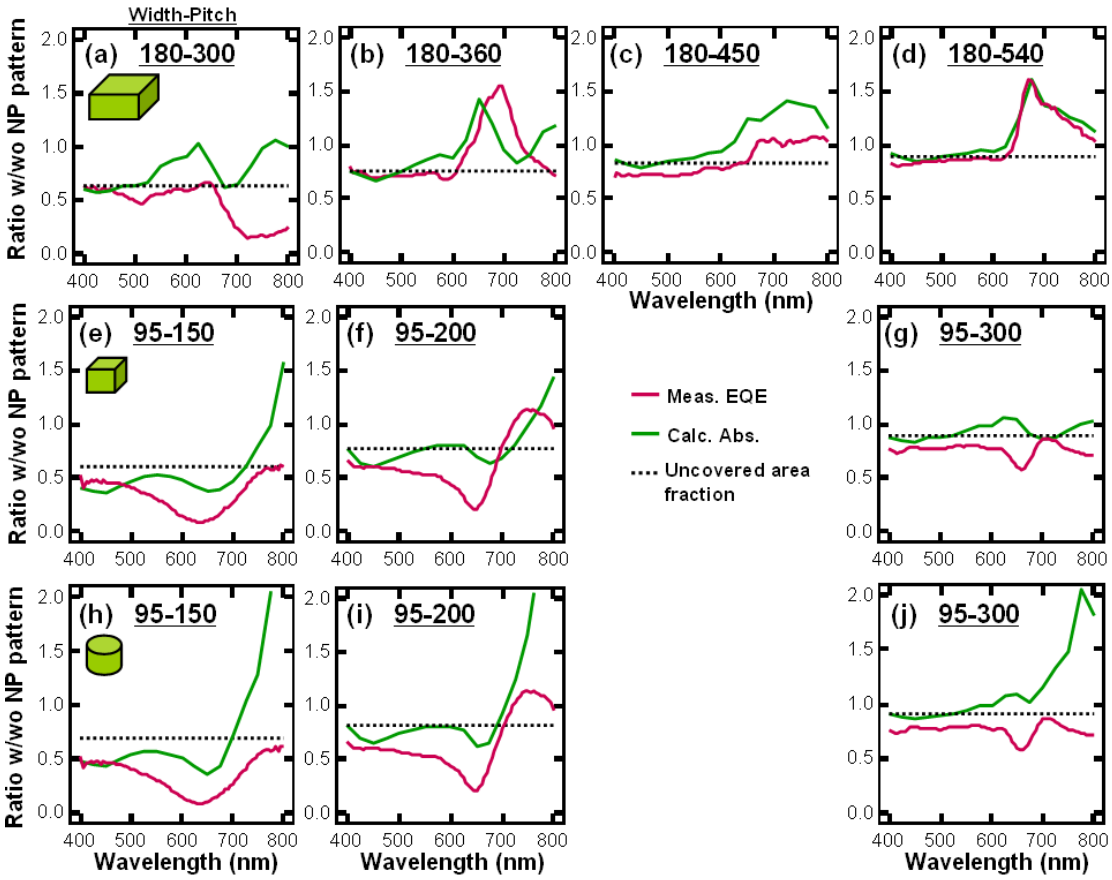

Figure 5.1.5.4 Ratios of measured EQE for devices with Au NP arrays and without (green curves) and ratios of calculated absorbance for devices with Au NP arrays and without (red curves). (a)-(d) are for fixed square-pillar width = 180 nm, height = 70 nm, and varying pitch from 300 nm to 540 nm. (e)-(g) Ratios for fixed square-pillar width = 95 nm, height = 70 nm, and varying pitch from 150 nm to 300 nm. (h)-(j) Ratios for fixed cylindical-pillar diameter = 95 nm, and varying pitch from 150 nm to 300 nm. The dotted lines in each plot show area fraction of the active layer not covered by nanopillars.

5.1.6 Comparison with Literature Reports on Effect of Au and Ag Nanoparticles

In both our measured EQE and calculated absorbance spectra, we found that for arrays of smaller size of nanopillar arrays, i.e. width = 95 nm, the additional absorption/scattering indicated by the peak in the extinction spectrum extinction doesn't give rise to an increase in BHJ OSC efficiency, rather it results a decrease (fig. 5.1.5.4 (e)-(j)). We suggested above that this is likely due to Joule heating within the nanopillars. This is qualitatively consist with EQE spectra published by Morfa, et. al. [69], where they observed a dip (~ 450 nm optical wavelength) in EQE (fig. 5.1.6.1 (c)) for devices incorporating randomly spatially distributed silver nanoparticle (averaged diameter 10 nm ~ 13 nm) deposited on an ITO coated glass substrate and covered by a PEDOT:PSS layer with different densities of Ag nanoparticles. In Morfa's approach Ag nanoparticles were formed by depositing a thin layer of Ag (1, 2, 3, and 4 nm) followed by thermal annealing resulting in a dewetting. The SEM image of Ag nanoparticles resulted from 2 nm thick silver film is reproduced in figure 5.1.6.1 (a) and the device architecture is reproduced in 5.1.6.1 (b). Fig. 5.1.6.1 (c) reproduces Morfa's measured EQE spectra. As shown by the vertical dotted line, the dips for devices with Ag nanoparticles coincide with the peaks in measured extinction pointed out in this paper (extinction spectra were not provided in the paper). With further increase the density of Ag nanoparticles by depositing thicker Ag film (3 nm and 4 nm), they observed larger dip in EQE. This is consistent with our results for devices

patterned Au nanopillar arrays with 95 nm wide and pitch in 150 nm, 200 nm, and 300 nm, as shown in fig. 5.1.5.4 (h), (i), and (j), respectively.

In contrast, Lee et. al.'s reported [67] an the increased in extinction at 550 nm optical wavelength (fig. 5.1.6.2 (d)) coincident with an increase in EQE (mainly enhanced from approximately from 500 nm to 600 nm, fig. 5.1.6.2 (e)) in the presence of Au nanospheres of 30 nm average diameter reproduced in (fig. 5.1.6.2 (a) and (b)) in their BHJ OSC devices. Lee et. al.'s device architecture (reproduced in figure 5.1.6.2. (c)) is similar to that for Morfa's devices (fig. 5.1.6.1 (b)) in which the nanoparticles are deposited on ITO surface and covered by a layer of PEDOT:PSS. They fabricated BHJ OSC devices with both low and high densities of Au nanoparticles. Their extinction measurement indicates an increased in extinction at ~ 550 nm wavelength for the low (fig. 5.1.6.2 (d), red curve) and high (fig. 5.1.6.2 (d), blue curve) density of Au nanoparticle covered by PEDOT:PSS deposited on quartz substrate. Although the authors stated that there is competition between the loss of transmission and enhancement of incident light intensity by a far-field scattering resulted from excitation of localized surface plasmon, the short circuit current density Jsc changes ***negligibly*** from 10.74 mA/cm^2 to 11.13 mA/cm^2 for control to device with low density Au. The coincident increases in EQE and in extinction at same optical wavelength suggests that in this case an increasing extinction gives rise to higher solar cell efficiency, presumably due to increased electric field intensity caused by far field scattering. Whether or not there is an increase in far field scattering should be addressed clearly to allow a correct insight into the enhancement in BHJ OSC efficiency due

to presence of small-sized Au nanoparticles. To address this, we carried out addition numerical simulations to calculate the absorbance of the P3HT:PCBM in Lee et. al.'s device. Figure 5.1.6.3 (a) shows our calculated extinction [108] (black curve), absorption (red), and scattering (blue) spectra for a free standing spherical Au nanoparticle with diameter 30 nm and refractive index for surrounding medium equal to 1.6, i.e. between the refractive index of PEDOT:PSS, 1.65[109], and that of quartz, 1.55 [110], at 550 nm optical wavelength. Our calculated extinction is in good semiquantitative agreement with Lee et. al.'s measured absorbance (more precisely extinction): both of sets of spectra show a peak near 550 nm wavelength. Next, we carried out a FDTD calculation to calculate the absorbance of P3HT:PCBM for a BHJ OSC device with and without spherical Au nanoparticles on ITO-coated glass substrate. In this simulation, the thickness of ITO, PEDOT:PSS, P3HT:PCBM, Al are 200 nm, 40 nm, 100 nm, and 150nm, respectively The LiF is optically thin (0.5 nm) and ignored in the simulation. Our calculated absorbance spectra for Lee et. al's devices are shown in figure 5.1.6.3 (b). The black curve is the absorbance spectra of a control cell without Au nanoparticles, and the blue curve is that of a cell with low density Au nanoparticle array, with pitch = 90 nm. The coverage of Au in this simulation is approximately the same as in Lee et. al.'s cell (SEM image in 5.1.6.2 (a)) containing low density of Au nanoparticles. Our calculated absorbance shows a dip in absorbance of P3HT:PCBM near our calculated extinction and their measured absorbance peaks, which indicates near the resonance the $|E|^2$ intensity in the P3HT:PCBM should be decreased due to Joule heating associated with

absorption by the Au nanoparticles. The red curve in figure 5.1.6.3 (b) shows the calculated Joule heating absorbance in the Au nanoparticles at the resonance wavelength (550 nm), and the fig. 5.1.6.3 (c) shows a $|E|^2$ image cutting though the center of a Au nanoparticle at the resonance wavelength. The $|E|^2$ is mostly concentrated inside the Au nanoparticle. Although there is some increased near field squared on the two sides of the nanoparticle, the $|E|^2$ only extends approximately 10 nm away from particle surface consistent with our other results, discussed above. This very near field is not far enough to reach into the P3HT:PCBM active layer. Therefore, the coincident increase in EQE around the peak of extinction in Lee et. al.'s report is apparently not due to the local increase in $|E|^2$ intensity in P3HT:PCBM due to excitation of localized surface plasmon resonances.

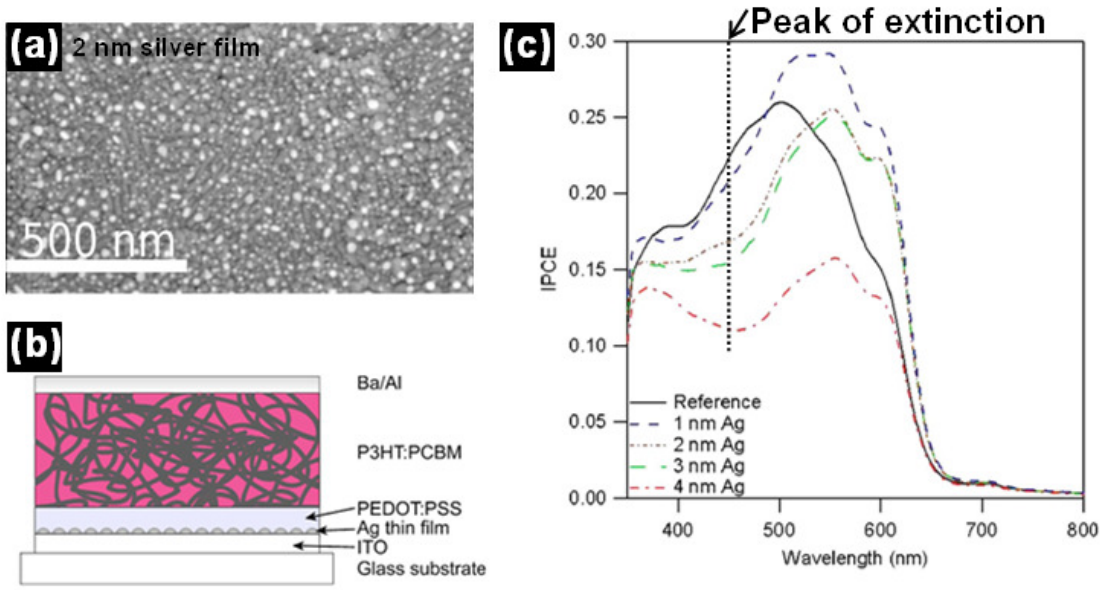

Figure 5.1.6.1 (a) SEM image of a representive a 2 nm thick silver film on ITO-coated glass substrate after annealing. (b) Device architecture of Morfa et. al.'s BHJ OSC incorporating silver nanoparticles. (c) External quantum efficiency spectra of devices containg 1, 2, 3, and 4 nm silver film (color curves) and of a control device without Ag nanoparticles. The dashed line indicates the wavelength (near 450 nm) in extinction peak of the sample with those silver films deposited on. Figures are adapted from [69].

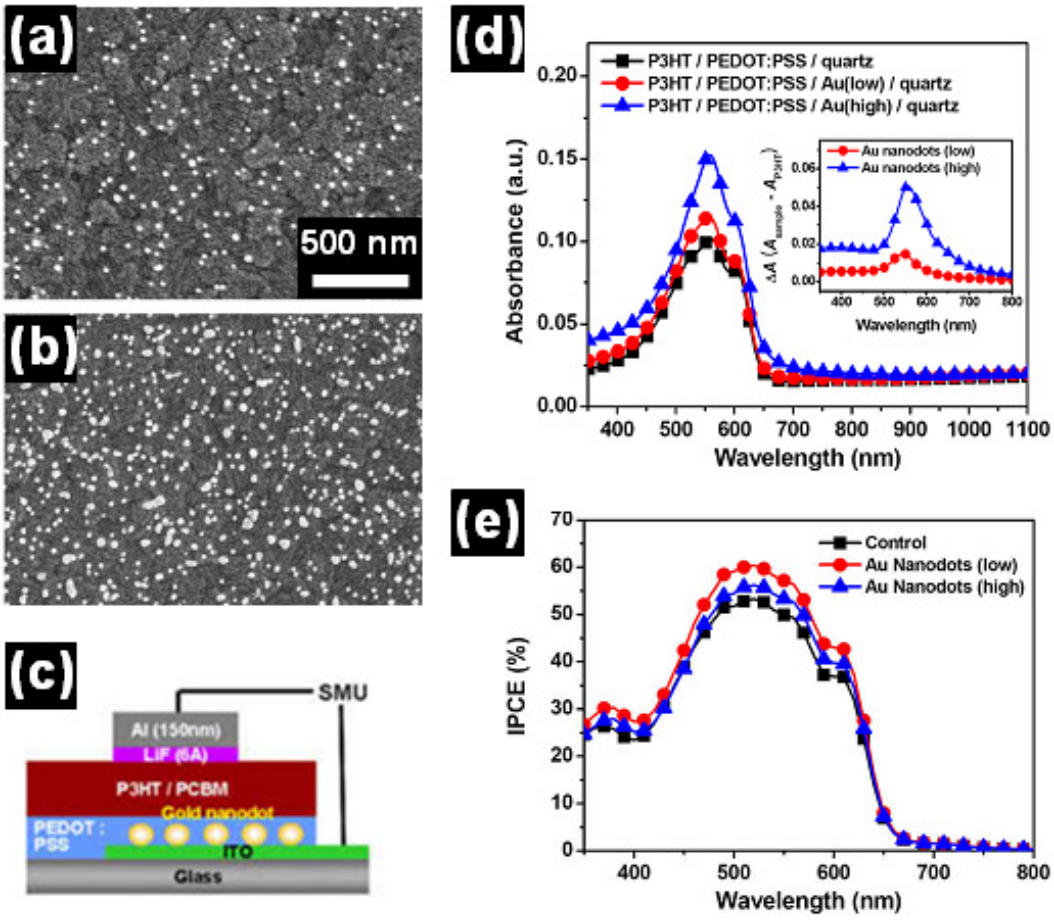

Figure 5.1.6.2 (a) and (b) SEM images of low and high densities of Au nanoparticles on an ITO-coated glass substrate, with particle diameter about 30 nm on average. (c) Device architecture of Lee et. al's BHJ OSCs with Au nanoparticles within a PEDOT:PSS film. (d) Extinction spectrum of the Au nanoparticles (red and blue curves) and control sample (black curve) on quartz substrate after deposited PEDOT:PSS layer. (e) External quantum efficiency of Lee et. al.'s OSCs with (red and blue curves) and without (black curve) Au nanoparticles. Figrues are taken from Lee et. al.'s report. [67]

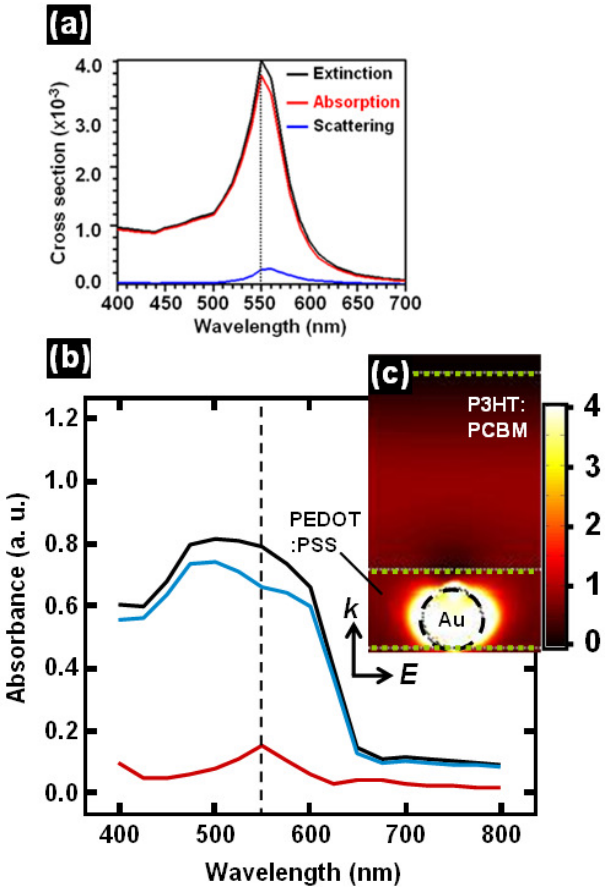

5.1.6.3 (a) Calculated extinction for a free standing spherical Au nanoparticle (30 nm in diameter) with refractive index of the sourrounding medium equal to 1.6. The calculation is done by the program provided in website (http://www.lightscattering.de/MieCalc/eindex.html [108]). (b) Black curve is for calculated absorbance of P3HT:PCBM in a control device corresponding to Lee et. al's OSC structure. Blue curve and red curves are for calculated absorbance of P3HT:PCBM and Au nanosphere, respectively, in a device with low density of Au nanoparticle (30 nm in diameter, and 90 nm in pitch) corresponding to Lee et. al's OSC structure. (c) A $|E|^2$ image, cutting though the center of a Au nanospheres with the incident light at resonance wavelength, 550 nm.

5.2 *Variation of Au Nanopillar Array Location in OSC Devices*

In the experiments described above we fabricated Au nanopillar arrays on the transparent electrode. A possible interpretation for the absence of an overall improvement is a suppression of the electromagnetic field in the active layer by the nanopillar arrays, as suggested by the results shown in Fig. 5.1.4.3. To test this possibility, we investigated the effect of the NP arrays at different location. Since the calculated absorbance spectra are in good agreement with the measured photocurrent spectra, we used numerical calculations of the field-squared to obtain the absorbance in the active layer for different particle placements. In this section, we present the simulated results for a fixed pillar width, height, and pitch on the absorbance of the active layer with NP's patterned on the front contact (ITO), on middle of active layer, and on back contact (TiOx/Al). The device architectures are shown in figure 5.2.1.

Figure 5.2.2 shows the plots of the absorbance as function of wavelength for three designs. The pillar topography was fixed at width 180 nm, pitch 540 nm, and height 70 nm, which we obtained about maximum and measured efficiency in this work. When the particles were moved forward from the front contact, the calculated absorbance increased qualitatively consistent with a simple shadowing model. The slightly lower absorbance from 400 nm to 500 nm wavelength for devices with NPs on the back contact (Al/TiOx) may result from diffraction, leading to destructive interference due to the positions of nanopillars. The absorbance at shorter wavelength increased for NP's placed at the rear of active layer, but the enhanced peak at 675 nm slightly decreased. The ratios of the short circuit photocurrent (under AM 1.5 G illumination) for the devices with to without nanopillars slightly increase

from 0.98 (NP on ITO) to 1.00 (NP in organic), and to 1.02 (NP on Al/TiOx) as we move the nanopillars toward back contact. Although the efficiency doesn't show significant improvement, we note that the topographic parameters of the nanopillar arrays are not optimized for the new design (placing Au nanopillars on the back contact). The calculated results show the possibility for further improving the efficiency by using Au nanopillar arrays in other organic solar cell architectures.

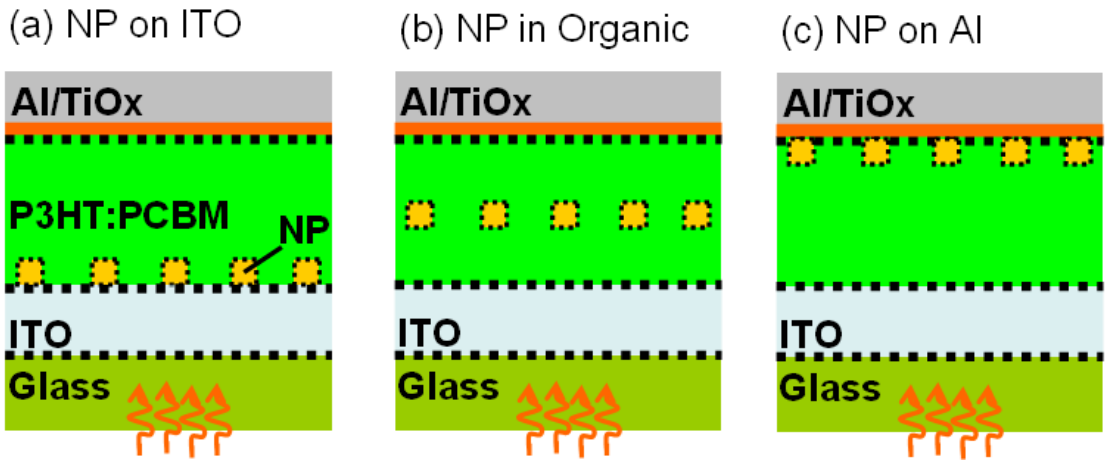

Figure 5.2.1 Schematics of device architectures used in the numerical calculations.

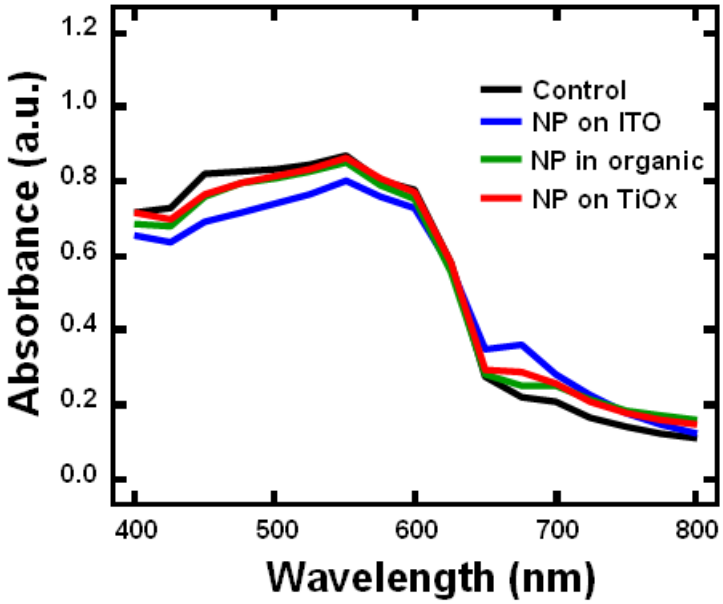

Figure 5.2.2 Calculated absorbance of the devices in which the Au nanopillar arrays are placed at different location: on ITO (blue), in organic (green), and on TiOx (red). In these calculation the pillar width= 180 nm, height= 70 nm, and pitch= 540 nm.

5.3 *Alternative Device Designs*

Our results confirm that the electric field intensity resulting from excitation of plasmons have effect on the EQE. However, the field induced by plasmon excitation can be suppressed in the high absorption medium. We find a possible improvement in design to achieve higher absorbance might be to place the nanoparticle on the back electrode, reducing shadowing effects.

For the low cost fabrication, it would be possible to fabricate silver nanoparticle by spray pyrolysis-synthesis on the back contact of the organic solar cell devices. Silver nanoparticles might be expected to give superior efficiency as they produce strong scattered field around the plasmon resonance, and the work function of the silver is lower than that of Au, for improved electron injection compared Au. In addition round nanoparticles might be expected to give more isotropic scattering than flat topped pillars leading to more intensity at larger scattered angles, effectively increasing the path length of light travel in the active layer.

Figure 5.3.1 (a) shows the calculated absorbance of an OSC device with a Ag nanosphere array on the back contact. The absorbance not suppressed at shorter wavelength in this case shows higher enhancement at wavelengths beyond 575 nm compared to the current design. The field enhancement is higher than the case where we place the nanoparticle on ITO substrate, which might be due to the interaction of Ag nanoparticle with the Ag substrate. [111] Most importantly, the enhanced field produced from the coupling is not only localized on the small volume of the particle surface, but is also spread in a region distant from the particle and the Ag layer (figure 5.3.1 (c)). Besides, other literature reports [111, 112] and our fluorescence

measurement and field calculation on active substrate (silicon, Ag, or Au) and nonactive (glass or ITO) substrate [13] have demonstrated that the particle plasmon resonance is significantly broadened with the active substrate present, leading to a field enhancement at wide range of wavelength. This might broaden the EQE spectrum of OPV devices.

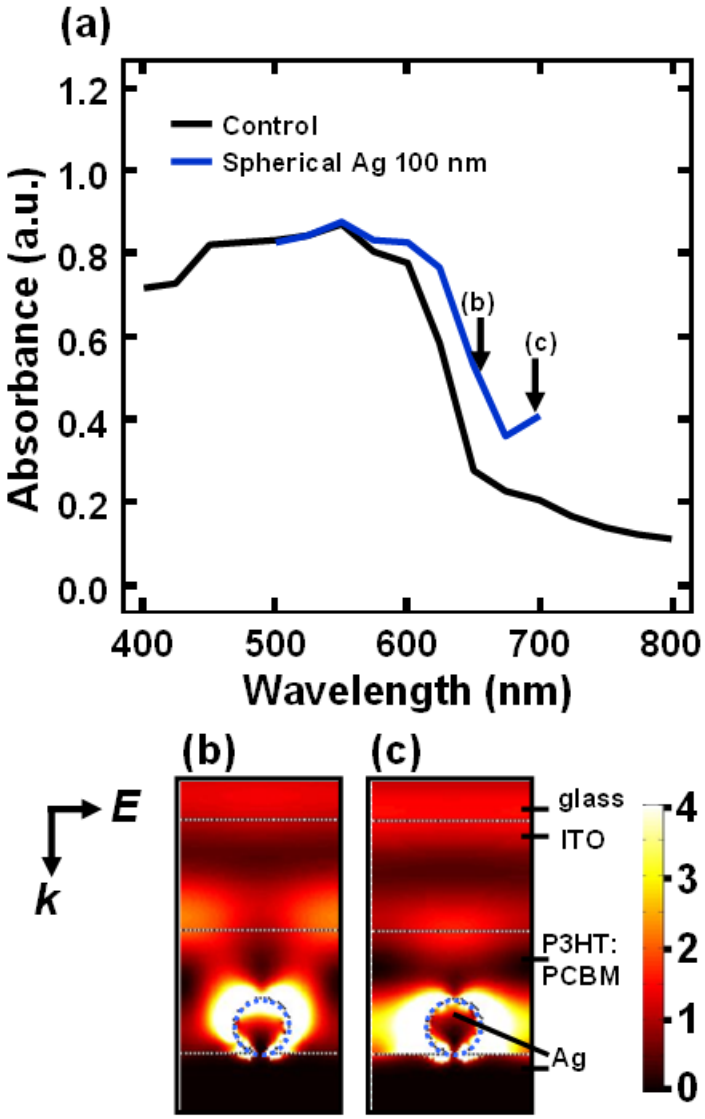

5.3.1 (a) Calculated absorbance of an control device (black) and an device with Ag spherical nanoparticle arrays (blue). The particle diameter is 100 nm and pitch is 300 nm. (b) and (c) are $|E|^2$ image in cross sectional view on the center of particle at incident wavelength 650 nm and 700 nm at the resonance frequencies.

Chapter 6: Conclusions

The major contributions of this work were to employ electron beam lithography in systematic studies of fluorescence and BHJ organic photovoltaic enhancement from noble metallic nanostructures.

Fluorescence enhancement from silver nanoparticles is highly size-, shape- , and polarized dependent. The measured extinction peaks shift toward red and blue with increasing aspect ratio for polarization of incident light parallel and perpendicular to the long axes, respectively, which are consistent with the theory of plasmon resonance.[11] Comparison with maxima in the fluorescence, however, shows that only half of the four reside within the bands formed by the peaks in absorption and reemission (Cy3 in short axis and Cy5 in long axis). For light polarization parallel to the long axis, the optimum enhancement shifts slightly to larger particle size for longer wavelength, which qualitatively agrees with the predicted red shift of the plasmon resonance for larger particle length/width ratio.[11] For the polarization perpendicular to the long axis, however, the peak still shifts to larger particle size for longer wavelength, which is opposite to the predicted blue shift in the transverse plasmon resonance, [11] although our shapes are more complex, resulting in additional modes. Therefore, by comparing the optimum height/width ratio of the spheroid nanoparticles with the polarization dependence of the incident light, simplest model of particle Plasmon resonance can no longer fully explain the mechanism in the fluorescence enhancement.

For isolated nanoparticles in enhanced fluorescence, we demonstrate that active substrates, i.e. those with large dielectric functions, have a strong effect on the size-

or period-dependence of fluorescence enhancement in the presence of a substrate, and the region of high field shift position as the particle size varies, thus maximum fluorescence enhancement occurs when a large fraction of those fluorophores which are not shadowed by either the particles or substrate are immersed in region of high field; low or no enhancement otherwise.

In the study of photovoltaics, photocurrent enhancement from gold nanopillar arrays is highly size-, shape, pitch-, position, dielectric constant of the surrounding medium dependent. We investigate nanoparticle arrays with tunable plasmon resonance range from 600 nm to > 800 nm wavelength. The red shift of plasmon resonance as increasing particle width and dielectric constant of the surrounding due to coating of P3HT:PCBM consistent with the theory of plasmon resonance [11]. The red shift as the pitch increased consists with Zhao et. al. [94] and Haynes et. al.s' [92] results, and they indicated that the red shift associates to the radiative dipole coupling in two–dimensional nanopillar arrays. We tested the assumption that several authors have been made in literature that increase absorption can give rise to solar cell efficiency [7, 67, 71, 73, 74]. Our systematically study in which we compared the extinction spectrum with photocurrent spectrum indicates that the extra absorption at 657 nm for Au nanoparticle arrays with width 95 nm didn't show enhanced photocurrent. Merely increase absorption due to excitation of plasmon resonance did not increase the efficiency, and the energy might lose by joule heating.

The spectra of measured external quantum efficiencies and calculated absorbance from FDTD simulations are qualitatively in good agreement. we find that while our prototype Au nanopillar-patterned devices show nearly the same overall

power conversion efficiency as those without nanopillars, the patterned devices (W= 180 nm, P= 540 nm, H= 70 nm) do show higher external quantum efficiency in a narrow wavelength range where the active layer absorption, however, is relatively low, from approximately 640nm to 720nm, with a peak of enhancement of about 60% at 675nm. Our calculated variation of the local electric field squared with wavelength within the active layer follows that of the measured external quantum efficiency; this modeling can thus reliably be used in further optimization of the nanostructural pattern parameters and optical properties of individual photovoltaic components. We also find evidence that this resonance of mixed nature, with contributions both from plasmon excitation and multiple reflections/diffraction within the cavity formed by the nanopillars and top electrode. Finally, our calculations indicate that the measured low value of attenuation coefficient k_A of the P3HT:PCBM active layer in the wavelength range of the observed mixed resonance is already close to the optimum value for achieving maximum absorption enhancement, and that if k_A were larger, which would be expected to increase the overall power conversion efficiency, then the resonance-field enhancement would be extinguished. Due to suppression by higher k_A, we are not able to enhance the field in the shorter wavelength (approximately < 625 nm), where the k_A of P3HT:PCBM is sufficient large.

To sum up, in this thesis, we investigated effect of Au nanopillar arrays in a BHJ OSC device when nanopillars are placed in front of active layer in the direction of incident light. Nanopillar height is fixed at 70 nm, nanopillar coverage is varied from 1% to 60 %, and width is varied from 60 nm to 240 nm. Similar design, i e. random distributed Ag nanoparticle on front part of devices was applied in silicon

based solar cell and the device with Ag nanoparticle shows 33% increase in power conversion efficiency [65]. Our prototype BHJ OSC devices with Au nanopillar array, however, show overall lower efficiency compared to the device without nanopillar arrays as nanopillar coverage increase. Our EQE measurement and calculated absorbance indicated that the decrease in efficiency is at shorter wavelength region (approximately < 600 nm) where absorption coefficient of active layer is relatively high, which can suppress high electric field contributed from interference and plasmons in that active layer. Our measured extinction spectrum for samples with smaller width nanopillar arrays do show increased in extinction at red side of absorption edge of active layer. This extra energy is dominated by nanopillar absorption and it might dissipate by joule heating. Therefore, device with smaller width of pillars shows lower efficiency compared to that with larger width of pillars for the same nanopillar area coverage. To achieve enhance efficiency by using noble metallic nanostructure in a BHJ OSC, we need to by pass the "shadowing effect" at wavelength with high attenuation coefficient for active layer and joule heating loss by placing nanostructure on the back electrode and using wider pillars.

Since both absorption and reemission of fluorescence are wide spectrums, the possible future work is to replace band pass filter and detector with spectrometer to collect spectral response of fluorescence. We can even replace the excitation by lamp with finite and compatible spectrum for absorption in fluorescence.

We expect this new insights provided by this work to lead to advances in the development of highly sensitive biochips. We further note that the work presented here represents only a limited optimization, and anticipate larger enhancements via a

systematic variation of the multiple parameters we find are important in noble metal nanoparticle enhanced fluorescence and photovoltaic. For photovoltaic enhancement by nanopillars, we suggest fabrication of the Ag nanospheres on the back (opaque) contact might lead to an overall enhancement of the organic solar cell efficiency.

Appendix A – Discrete Dipole Approximation (DDA)

The whole system, including nanoparticles and a substrate are modeled by collection of N dipoles with dipole moment $\vec{p}$. We calculate the response of these dipoles to fields associated with the incident light and those induced by the other dipoles.[80] For a dipole at site *i*, the dipole moment is $\vec{p}_i$ with amplitude α proportional to the electric field on the *i* site (eq. (A1) and (A2))

$$p_i = \alpha\ E_i \tag{A1}$$

$$E_i = E_0 \hat{y} \exp(ikx_i) + \sum_{j \neq i} \frac{\exp(ikr_{ij})}{r_{ij}^{\ 3}} \times [k^2 (r_{ij} \times p_j) \times r_{ij} + \frac{(1 - ikr_{ij})}{r_{ij}^{\ 2}} (3 p_j \cdot r_{ij} r_{ij} - r_{ij}^{\ 2} p_j)] \tag{A2}$$

$$p_i^{\ (l+1)} = \eta \alpha E_i^{\ (l+1)} + (1 - \eta) p_i^{\ (l)} \tag{A3}$$

Here E_i is the electric field on the *i* site resulting from the incident light and induced field from other dipoles. By an iterative method with initial condition $p_i^{\ (0)} = 0,\ \ E_i^{\ (1)} = E_0 \hat{y} \exp(-ikx_i)$, we can calculate the dipole moments, using

$$E_i^{\ (l+1)} = E_0 1_z \exp(ikx_i) + \sum_{j \neq i} \frac{\exp(ikr_{ij})}{r_{ij}^{\ 3}} \times [k^2 (r_{ij} \times p_j^{\ l}) \times r_{ij} + \frac{(1 - ikr_{ij})}{r_{ij}^{\ 2}} (3 p_j^{\ l} \cdot r_{ij} r_{ij} - r_{ij}^{\ 2} p_j^{\ l})] \tag{A4}$$

,where η is introduced for improving convergence, set 0.5. Then we extract the dipole moments for each site to calculate the spatial variation of electric field.[85]

Appendix B - Finite-Difference Time-Domain (FDTD)

In 1966 Yee[101] proposed a technique to solve Maxwell's curl equations using the finite-difference time-domain method.[113] It has been used to solve numerous scattering problems on microwave circuits, dielectrics and electromagnetic wave interaction with a number of materials at different frequencies.[114-116]

Maxwell's equations for an isotropic medium are:

$$\nabla \times \vec{E} + \frac{\partial \vec{B}}{\partial t} = 0 \tag{B1a}$$

$$-\nabla \times \vec{H} + \frac{\partial \vec{D}}{\partial t} = \vec{J} \tag{B1b}$$

$$\vec{B} = \mu \vec{H} \tag{B1c}$$

$$\vec{D} = \varepsilon \vec{E} \tag{B1d}$$

Where $\vec{J}, \mu, \varepsilon$ are assume to be given functions of space and time. In a Cartesian coordinate system, (B1a), (B1b) are equivalent to the following:

$$\frac{\partial H_x}{\partial t} = \frac{1}{\mu}\left(\frac{\partial E_y}{\partial z} - \frac{\partial E_z}{\partial y}\right) \tag{B2a}$$

$$\frac{\partial H_y}{\partial t} = \frac{1}{\mu}\left(\frac{\partial E_z}{\partial x} - \frac{\partial E_x}{\partial z}\right) \tag{B2b}$$

$$\frac{\partial H_z}{\partial t} = \frac{1}{\mu}\left(\frac{\partial E_x}{\partial y} - \frac{\partial E_y}{\partial x}\right) \tag{B2c}$$

$$\frac{\partial E_x}{\partial t} = \frac{1}{\varepsilon}\left(\frac{\partial H_z}{\partial y} - \frac{\partial E_y}{\partial z} - \sigma E_x\right) \tag{B2d}$$

$$\frac{\partial E_y}{\partial t} = \frac{1}{\varepsilon}\left(\frac{\partial H_x}{\partial z} - \frac{\partial E_z}{\partial x} - \sigma E_y\right) \tag{B2e}$$

$$\frac{\partial E_z}{\partial t} = \frac{1}{\varepsilon}\left(\frac{\partial H_y}{\partial x} - \frac{\partial E_x}{\partial y} - \sigma E_z\right) \tag{B2f}$$

Yee defines the grid coordinates (i,j,k) as

$$(i, j, k) = (i\Delta x, j\Delta y, k\Delta z) \tag{B3a}$$

where $\Delta x, \Delta y, \Delta z$ are the actual grid separations. Any function of space and time is written as

$$F^n(i, j, k) = F(i\Delta x, j\Delta y, k\Delta z, n\Delta t) \tag{B3b}$$

where Δt is the time increment, n is the time index and $\delta = \Delta x = \Delta y = \Delta z$. The spatial and temporal derivatives of written using central finite difference approximations as

$$\frac{\partial F^n(i, j, k)}{\partial x} = \frac{F^n(i + \frac{1}{2}, j, k) - F^n(i - \frac{1}{2}, j, k)}{\delta} + O(\delta^2) \tag{B4a}$$

$$\frac{\partial F^n(i, j, k)}{\partial t} = \frac{F^{n+\frac{1}{2}}(i, j, k) - F^{n-\frac{1}{2}}(i, j, k)}{\delta t} + O(\delta t^2) \tag{B4b}$$

Equations (B4a), (B4b) are applied to the six scalar equations (B2a) ~ (B2f) resulting in six coupled explicit finite difference equations, and then the electric field and the magnetic field are solved alternatively in time. In all of the finite difference equations the components of $\vec{E}, \vec{H}$ are located within a single unit cell in the three-dimentional lattice depicted in Figure B.1.

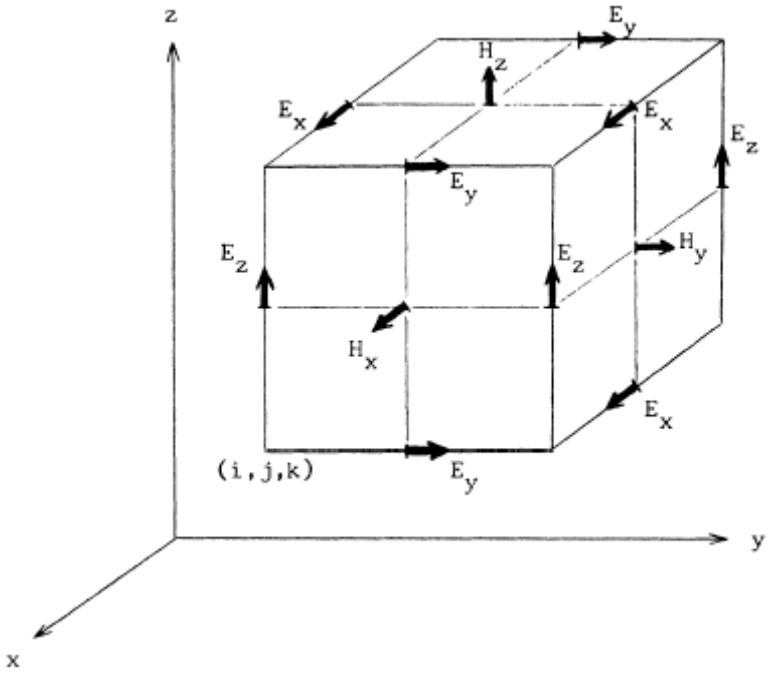

Figure B.1 Yee cell demonstrates the arrangement of field components within a cubical grid.

To yield accurate results, the grid spacing δ in the finite difference simulation must be much less than the wavelength, usually less than $\frac{\lambda}{10}$. The stability condition relating the spatial and temporal step size is[117]

$$v_{\max}\Delta t = [\frac{1}{\Delta x^2} + \frac{1}{\Delta y^2} + \frac{1}{\Delta z^2}]^{-\frac{1}{2}} \tag{B5a}$$

where $v_{\max}$ is the maximum velocity of the wave. When the step size δ is the same in all directions, the stability condition is

$$\frac{v_{\max}\Delta t}{\delta} = \frac{1}{\sqrt{N}} \tag{B5b}$$

where N is the number of spatial dimensions in the problem.

Appendix C – **Metrology of Spherical Nanoparticles**

The statistics of the size and the number density of the particles can be obtained by analyzing SEM images scanned from the sample with image processing software developed in Java [118] Originating from the ImageJ module (NIH), it defined particle regions on images by convolution with a series of image processing matrixes, and analyzes particle spacing based on Voronoi's theorem.[119] This yielded statistics of particle distribution; more details are described below.

E. Rencs and S.-H. Guo have created an algorithm to extract statistics on particle average area, volume, center-to-center distance, and peak-to-peak distance based upon real AFM and SEM images.[118] We have used this analysis to correlate metal enhanced fluorescence with these geometrical parameters in a meaningful way, and to derive conditions for which the MEF is optimized. In the pre-processing step, the source image passes through a series of convolutions with different image processing matrixes and results in several intermediate images prepared for particle definition. In addition, it also allows users to subtract background for AFM images to accommodate piezo effect in tip scanning. In the particle definition step, we find the correlation in between those intermediate images from previous process, followed by morphological pruning and erosion plus dilation to eliminate sharp noises and close up the particle edges. After we determine the particle edges, we label every particle region and define territories by implementing the Vorinoi theorem.[119, 120] Finally, the program extracts particle statistic information and exports data after merging or deleting those non-particle territories selected by user.

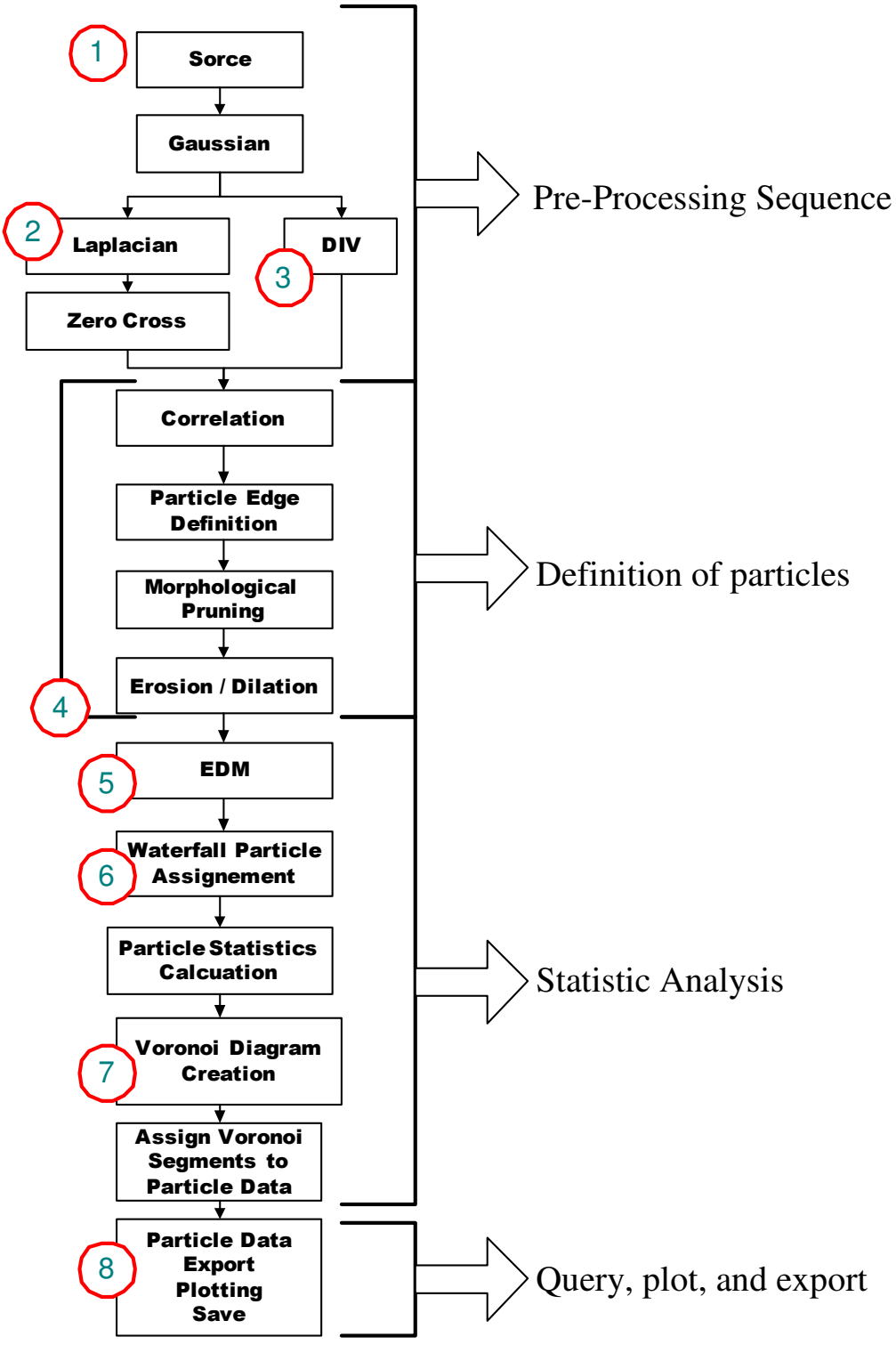

Figure C.1: Algorithm flow chart for Java software.

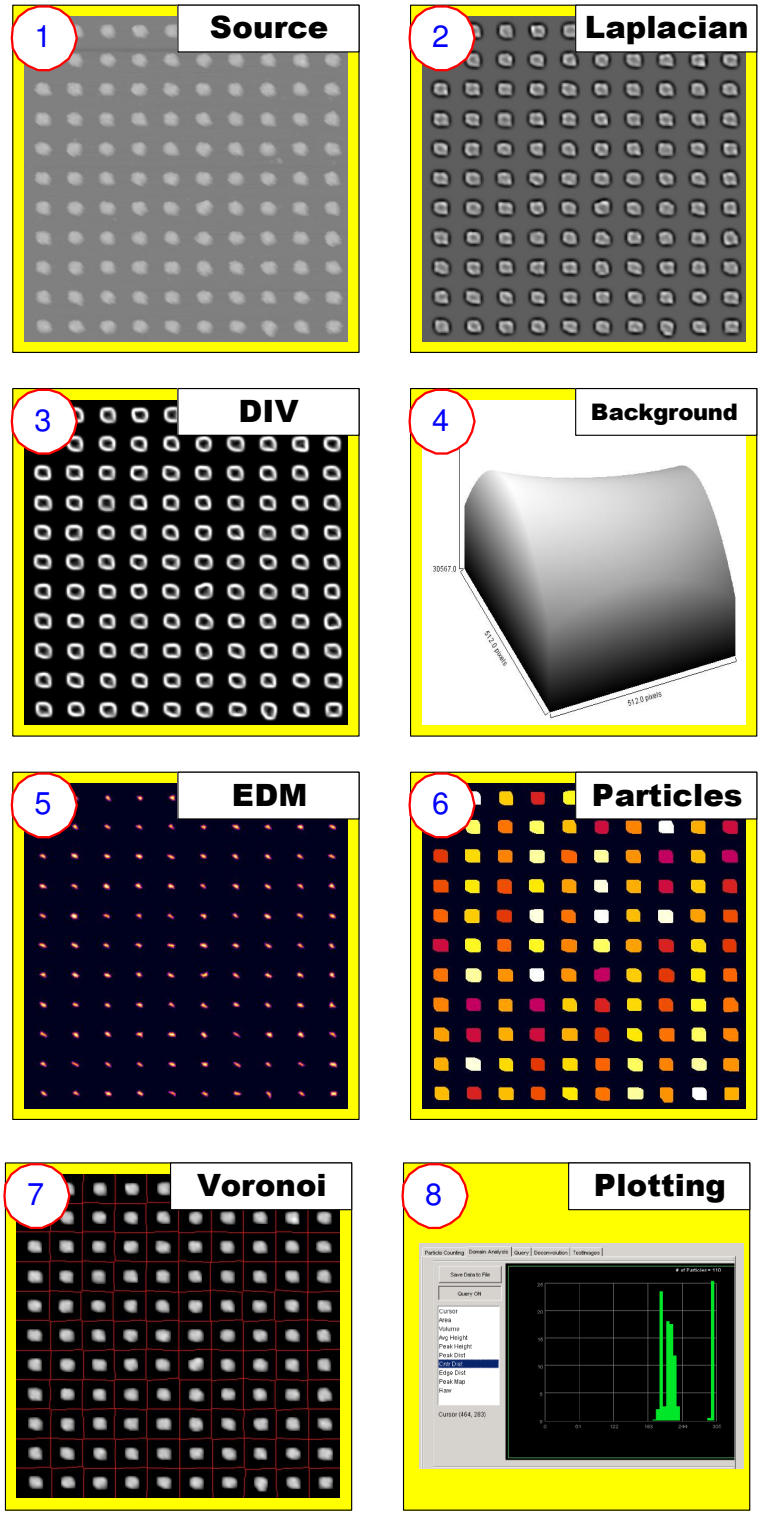

Figure C.2 Intermediate images or plots for steps labeled in Fig. C.1.

Appendix D – **Test of FDTD Software**

To test whether the FDTD software can work properly for a diffraction problem, we performed a two-dimensional FDTD simulation to solve a single slit diffraction case which we can easily compare the simulated results with theoretical value. Figure D.1 shows the geometry set up and the single-slit pattern obtained from the simulation and Formula of Fraunhofer approximation:

$$I(\theta) = I(0)(\sin\beta/\beta)^2 \qquad \text{(E1)}$$

, where $\beta = (b/\lambda)\sin\theta$ and b is the width of the slit.[121] Here the incident wavelength is 400 nm and slit width is 1600 nm.

The shapes of the pattern intensities taken from simulation and theory are in a good agreement.

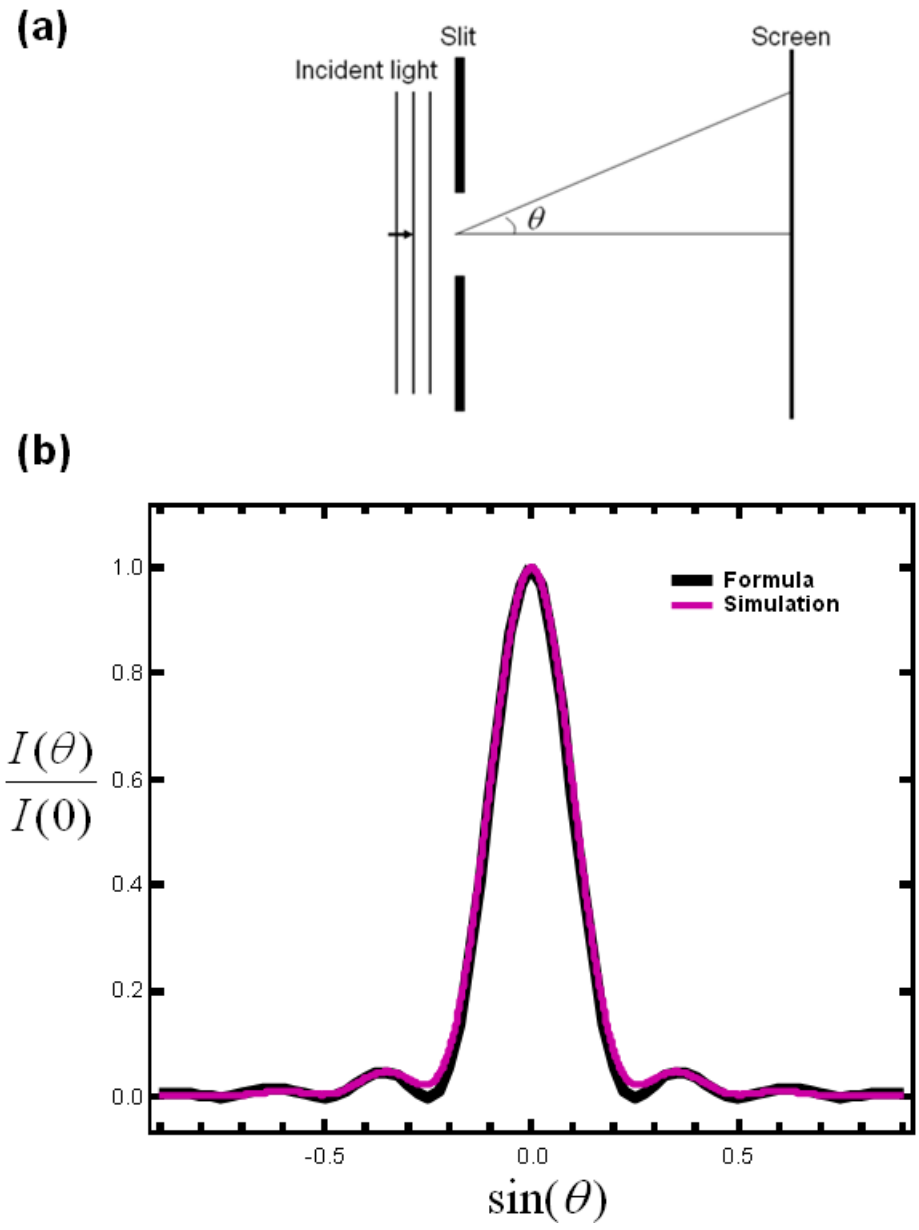

Figure D.1 (a) The single slit set up. (b) The single-slit pattern obtained from theoretical value (black) and from 2D-FDTD simulation (purple).

Appendix E – **Variable Angle Spectroscopic Ellipsometry**

Variable angle spectroscopic ellipsometry [122] uses a traditional rotating analyzer ellipsometer. It is very sensitive measurement technique for measurement of optical constants in the UV, visible, and IR wavelength ranges (230 nm-1700 nm). It measures a change in the polarization of light as it reflects or transmits from a material structure. It is used to characterize thin films, bulk, surfaces, and material microstructure. The polarization-change is represented as an amplitude ratio (Ψ) and a phase difference (Δ) at every wavelength/angle combination, which is dependent on optical properties and thickness of each material. When the angle of incidence is near the pseudo-Brewster angle the measured Δ values are near 90°, and this range of Δ values provides the most sensitive measurement of the sample for VASE. Thus, multi angle ellipsometry measurements allow us to ensure that for each wavelength, at least on pair of Ψ and Δ values is near the optimum measurement condition. The data produced from multi angle measurement reduces noise in the fitted parameters.

In this work we used a commercial VASE (J. A. Woollam Co., Inc). The instrument layout is shown in figure E1. The VASE is equipped with a Xenon lamp (190 nm ~ 2 μm) as light source. The wavelength is selected by a monochromator with a beam chopper placed at the output of the monochromator. The wavelength selected light is passed though a fixed polarizer before the sample. The beam reflected at the sample is passed though a continuously rotating analyzer, and reaches the detector. Silicon and InGaAs detectors were used spectral ranges of 300nm to 800nm and that of 800nm to 1700nm, respectively.

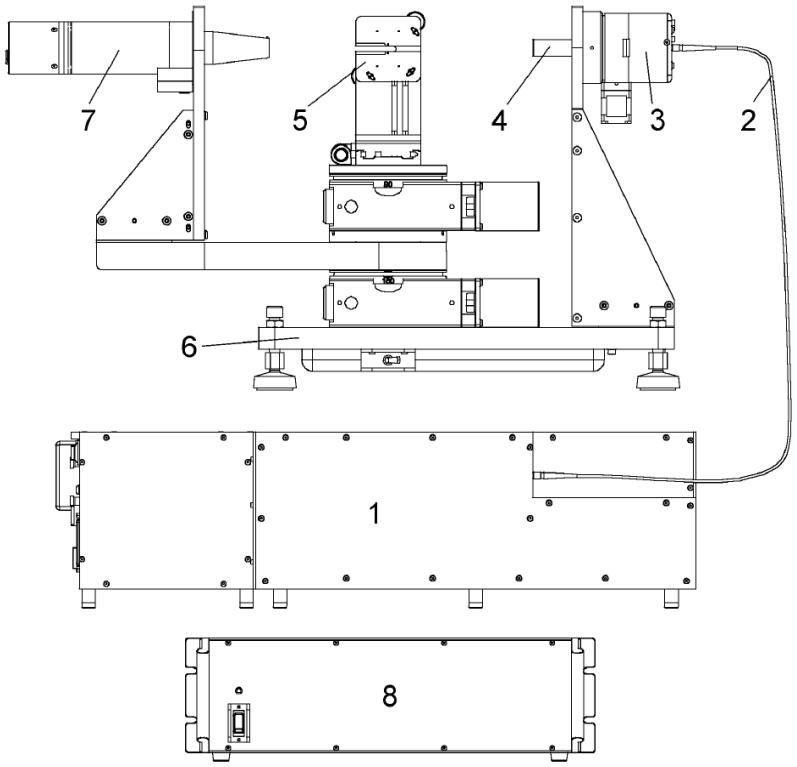

Figure E1 The Woollam Co. variable angle spectroscopic ellipsometer(VASE®). Components include: 1) monochromator, 2) fiber optic cable, 3) input unit with polarizer, 4) alignment detector, 5) sample stage, 6) goniometer base for automated angle control, 7) detector unit with rotating analyzer and solid state detectors, and 8) motor control box. The figure is taken from [122].

VASE doesn't directly measure the optical constants of the sample. It measures the Ψ and △values that correspond to the optical constants. After the Ψ and △values are obtained experimentally, we run a simulation to determine the Ψ and △values for trial values of film thickness and optical parameters, n and k, as illustrated in figure E2.

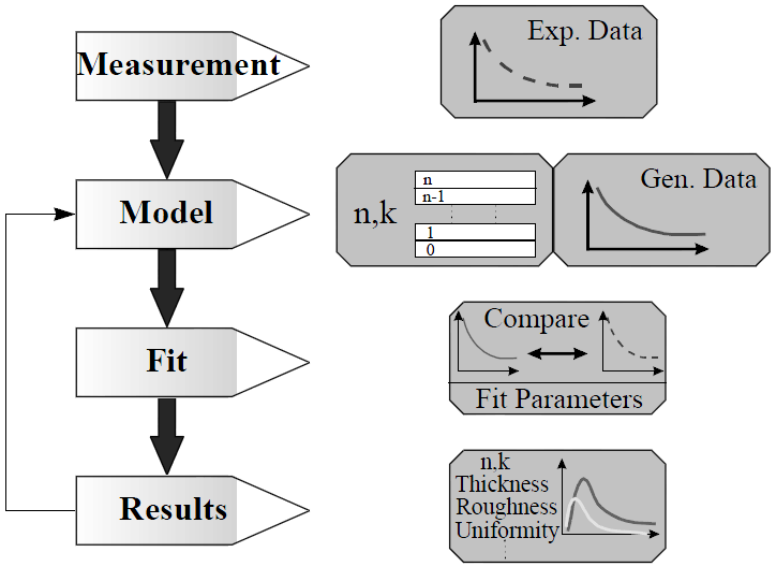

Figure E2 General procedure for ellipsometry measurement to determine optical properties of materials from experimental data [122].

For a general elliptical polarization the detected signal is a sinusoid with a DC offset of the form:

$$V(t) = V_{DC} + a \cdot \cos(2\omega t) + b \cdot \sin(2\omega t) \quad \text{(E1)}$$

The two important quantities measured by the ellipsometer are αand β, which are the normalized Fourier coefficients of the signal. They can be represented in terms of the Ψ and Δvalues for the sample and the (known) polarizer azimuthal angle as follows.

$$\alpha = \frac{a}{DC} = \frac{\tan^2 \Psi - \tan^2 P}{\tan^2 \Psi + \tan^2 P} \quad \text{(E2)}$$

$$\beta = \frac{b}{DC} = \frac{2 \tan \Psi \cos \Delta \tan P}{\tan^2 \Psi + \tan^2 P} \quad \text{(E3)}$$

, where P is the input polarizer azimuth with respect to the place of incidence. Thus, the Ψ and Δvalues cab be obtained:

$$\tan \Psi = \sqrt{\frac{1+\alpha}{1-\alpha}} \cdot \left| \tan P \right| \quad \text{(E4)}$$

$$\cos \Delta = \frac{\beta}{\sqrt{1-\alpha^2}} \cdot \frac{\tan P}{\left| \tan P \right|} \quad \text{(E5)}$$

On the other hand, the Ψ and Δ values can be obtain by the calculating the reflectance coefficients with given measurement geometry and optical constants of the materials. The multiple polarized reflections of the incident light beam that occur in the film for the case of a single film on an optically thick substrate are shown in Figure E3.

The total reflected beam for the single film system can be expressed as:

$$\tilde{R}_{p,s} \equiv \frac{\tilde{E}^r{}_{total}}{\tilde{E}_{incident}} = \frac{\tilde{r}_{p,s,01} + \tilde{r}_{p,s,12} e^{-i2\gamma}}{1 + \tilde{r}_{p,s,01} \tilde{r}_{p,s,12} e^{-i2\gamma}} \quad \text{(E6)}$$

, where γ is the "phase thickness" of the film, and can be calculated by

$$\gamma = 2\pi\tilde{n}_1 \frac{d}{\lambda}\cos\tilde{\phi}_1 = 2\pi\frac{d}{\lambda}\sqrt{\tilde{n}_1^{\,2} - \tilde{n}_0^{\,2}\sin^2\phi_0} \tag{E7}$$

,where d is the film thickness and λ is the incident wavelength. $\tilde{r}_{p,s,01}$ and $\tilde{r}_{p,s,12}$ are Fresnel p- or s-polarized reflection coefficients and are expressed as:

$$\tilde{r}_{p,s,01} = \frac{\tilde{n}_1\cos\phi_0 - \tilde{n}_0\cos\phi_1}{\tilde{n}_1\cos\phi_0 + \tilde{n}_0\cos\phi_1} \tag{E8}$$

$$\tilde{r}_{p,s,12} = \frac{\tilde{n}_2\cos\phi_1 - \tilde{n}_1\cos\phi_2}{\tilde{n}_2\cos\phi_1 + \tilde{n}_1\cos\phi_2} \tag{E9}$$

In the above expressions, ϕ_0 is the angle of the incident beam and the sample normal, $\tilde{\phi}_1$ and $\tilde{\phi}_2$ are the angles of the transmitted beam in the film and in the substrate, respectively. $\tilde{\phi}_1$ and $\tilde{\phi}_2$ can be calculated from Snell's law, $\tilde{n}_0\sin\phi_0 = \tilde{n}_1\sin\tilde{\phi}_1$. Finally, from the definition of the ellipsometric pametera, Ψ and Δ can be obtained by:

$$\tilde{\rho} \equiv \tan\Psi e^{i\Delta}\frac{\tilde{R}_p}{\tilde{R}_s} \tag{E10}$$

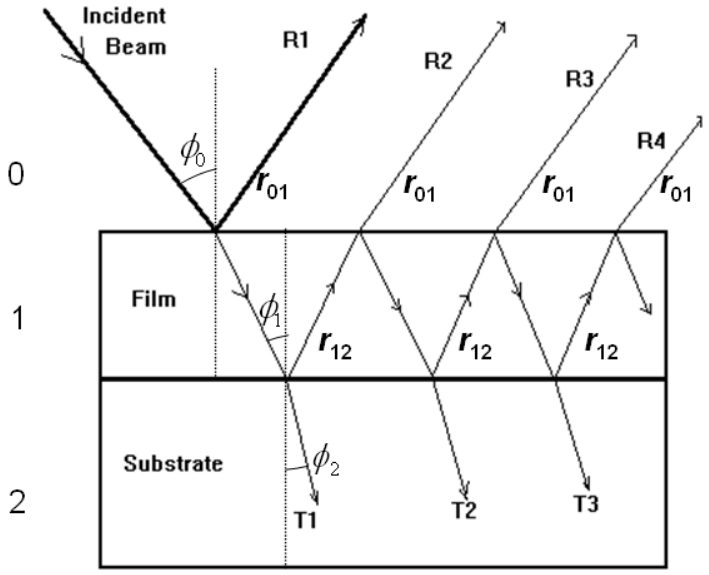

Figure E3 Multiple reflected and transmitted beams for a single film on an optically thick substrate.

The complex index of refraction $\tilde{n}$ can be determined from the complex dielectric function:

$$\tilde{n} = \sqrt{\tilde{\varepsilon}} = n + ik \tag{E11}$$

The dielectric constants of the materials obtained from Drude-Lorentz model[123] are used to fit the measured Ψ and Δ values. The complex dielectric function $\tilde{\varepsilon}(\omega)$ in the Drude-Lorentz model can be expressed as

$$\tilde{\varepsilon}(\omega) = \varepsilon_R + i\varepsilon_I = \varepsilon_\infty + \frac{f_0\omega_P^2}{-\omega^2 - i\omega\Gamma_0} + \sum_{k=1}^{n} \frac{f_k\omega_P^2}{(\omega_k^2 - \omega^2) - i\omega\Gamma_k} \tag{E12}$$

, where ω_p is the plasma frequency and n is the number of Lorentz oscillators with center frequencies (ω_k), strengths (f_k) and damping constants (Γ_k), ε_∞ is an additional offest term defined in the model. The first two terms result from intraband optical transitions (Drude model) and the third term represents interband transitions (Lorentz model). The number of Lorentz oscillators which must be included depends on the material.

To obtain the optical constants of the ITO and P3HT:PCBM, we measure the Ψ and Δ values on a ITO-coated glass substrate and a P3HT:PCBM film on a silicon wafer. From the number, wavelength, strength, and width of the peaks of the absorption spectra for the ITO and P3HT:PCBM obtained from the transmission measurement, we estimated the number, frequency, strength, and damping constant of the Lorentz oscillators, respectively. Combing in these with the film thickness obtained from profilometer measurements provides an initial guess values for the values in the fitting procedure for a single film on a substrate system.

Appendix F – **Effect of PEDOT:PSS on Nanopillars**

For the conventional BHJ OPV devices, a thin layer of PEDOT:PSS (~ 40 nm) are coating on the interface of ITO and active layer for reducing hole injection barrier. This layer add an spacing between NP and the active layer and expected to be reduce the enhanced near field in the active layer. For an oscillating dipole, the near field amplitude decays as ~ $1/r^3$, where r is the distance away from the dipole. The $|E|^2$ intensity is decay as $1/r^6$. On the other hand, in the section 5.1.4, we show that the near field would be suppressed as the imaginary part of the index of the absorbing layer is increased. We are interested to know whether this suppression can be avoided by introducing an spacing layer, PEDOT:PSS [109], with lower absorption materials in between nanopillars and the active layer. Therefore, we carried out the simulation to see how the absorbance would be look like by adding a 40 nm thick of PEDOT:PSS on the ITO/Au nanopillars surface.

Figure F (a) shows the absorbance of the Au NP-patterned device without (blue curve) and with 40 nm thick PEDOT:PSS (red curve), and the control device without PEDOT:PSS (black). The absorbance for the patterned device with PEDOT:PSS is lower than that for without especially at shorter wavelength region, which indicates that adding a thin layer of lossless material doesn't help to avoid the suppression of the field. The $|E|^2$ image (figure F (b) and (c)) show although there is higher field intensity on the surface of nanopillars with coating of PEDOT:PSS, the high field in PEDOT:PSS layer doesn't efficiently extend into the active layer. The results also indicate that to be able to take full advantage of the field from plasmon resonance but without sacrificing the charge collection efficiency, a thinner interface layer should be

introduced for the devices incorporating Au nanopillar arrays in vicinity to the P3HT:PCBM.

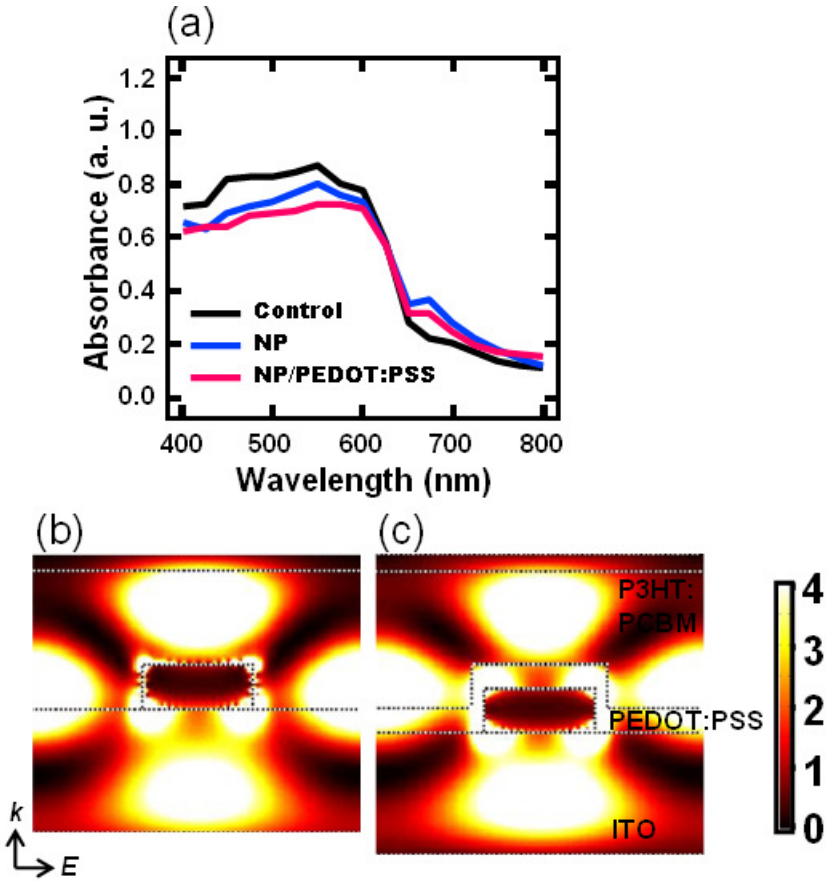

Figure F (a) Calculated absorbance of Au patterned cell with (red) and without (blue) coating a 40 nm thick of PEDOT:PSS, and control cell without NP and PEDOT:PSS (black). The width of nanopillar is 180 nm, height is 70 nm, and pitch is 540 nm. (b) and (c) are $|E|^2$ images cutting though the center of the nanopillar for the devices without and with a layer of PEDOT:PSS under the illumination at 675 nm wavelength, respectively.

References

[1] U. Kreibig and M. Vollmer, *Metal Clusters*. Germany: Springer-Verlag: Heidelberg, 1995.

[2] S. C.Street, C. Xu, and D. W. Goodman, *Annu. Rev. Phys. Chem.*, vol. 48, pp. 43-68, 1997.

[3] R. P. Andres, J. D. Bielefeld, J. I. Henderson, D. B. Janes, V. R. Kolagunta, C. P. Kubiak, W. J. Mahoney, and R. G. Osifchin, *Science*, vol. 273, pp. 1690-1693, 1996.

[4] J. G. Shi, S.; Babcock, K.; Awschalom, D. D., *Science*, vol. 271, pp. 937-941, 1996.

[5] M. Moskovits, *Reviews of Modern Physics*, vol. 57, pp. 783, 1985.

[6] J. R. Lakowicz, *Analytical Biochemistry*, vol. 298, 2001.

[7] Joseph R. Cole and N. J. Halas, "Optimized plasmonic nanoparticle distributions for solar spectrum harvesting," *Appl. Phys. Lett.*, vol. 89, pp. 153120, 2006.

[8] S. Nie and S. R. Emory, *Science*, vol. 275, pp. 1102, 1997.

[9] Kadir Aslan, Zoya Leonenko, Joseph R. Lakowicz, and C. D. Geddes, "Annealed Silver-Island Films for Applications in Metal-Enhanced Fluorescence: Interpretation in Terms of Radiating Plasmons," *Journal of Fluorescence*, vol. 15, pp. 643-654, 2005.

[10] H. A. Atwater and A. Polman, "Plasmonics for improved photovoltaic devices," *Nature Materials*, vol. 9, pp. 205-213, 2010.

[11] K. Lance Kelly, Eduardo Coronado, Lin Lin Zhao, and G. C. Schatz, "The Optical Properties of Metal Nanoparticles: The Influence of Size, Shape, and Dielectric Environment," *J. Phys. Chem. B*, vol. 107, pp. 668 -677, 2003.

[12] T. D. Corrigan, S. H. Guo, H. Szmacinski, and R. J. Phaneuf, "Systematic study of the size and spacing dependence of Ag nanoparticle enhanced fluorescence using electron-beam lithography," *Applied Physics Letters*, vol. 88, pp. 101112, 2006.

[13] S. H. Guo, S. J. Tsai, H. C. Kan, D. H. Tsai, M. R. Zachariah, and R. J. Phaneuf, "The effect of an active substrate on nanoparticle-enhanced fluorescence," *Advanced Materials*, vol. 20, pp. 1424-1428, 2008.

[14] George C. Schatz and R. P. V. Duyne, *Surface-enhanced Vibrational Spectroscopy*: Northwestern University, Evanton, IL, USA, 2002.

[15] T. C. Pluym, Q. H. Powell, A. S. Gurav, T. L. Ward, T. T. Kodas, L. M. Wang, and H. D. Glicksman, "Solid silver particle production by spray pyrolysis," *Journal of Aerosol Science*, vol. 24, pp. 383, 1993.

[16] D.-H. Tsai, S. H. Kim, T. D. Corrigan, R. J. Phaneuf, and M. R. Zachariah, "Electrostatic-directed deposition of nanoparticles on a field generating substrate," *Nanotechnology*, vol. 16, pp. 1856, 2005.

[17] H. J. Fissan, C. Helsper, and H. J. Thielen, "Determination of particle size distributions by means of an electrostatic classifier," *Journal of Aerosol Science*, vol. 14, pp. 354, 1983.

[18] George W. Crabtree and N. S. Lewis, "Solar energy conversion," *Physical Today*, vol. March, pp. 37, 2007.

[19] G. Li, V. Shrotriya, J. S. Huang, Y. Yao, T. Moriarty, K. Emery, and Y. Yang, "High-efficiency solution processable polymer photovoltaic cells by self-organization of polymer blends," *Nature Materials*, vol. 4, pp. 864-868, 2005.

[20] H. Y. Chen, J. H. Hou, S. Q. Zhang, Y. Y. Liang, G. W. Yang, Y. Yang, L. P. Yu, Y. Wu, and G. Li, "Polymer solar cells with enhanced open-circuit voltage and efficiency," *Nature Photonics*, vol. 3, pp. 649-653, 2009.

[21] D. J. Nash and J. R. Sambles, "Surface plasmon-polariton study of the optical dielectric function of silver," *Journal of Modern Optics*, vol. 43, pp. 81-91, 1996.

[22] U. Kreibig and M. Vollmer, "Optical Properties of Metal Clusters," *Springer*, 1995.

[23] H. Raether, "Surface Plasmons on Smooth and Rough Surfaces and on Gratings," *Springer-Verlag*, 1988.

[24] A. Otto, "Excitation of Nonradiative Surface Plasma Waves in Silver by Method of Frustrated Total Reflection," *Zeitschrift Fur Physik*, vol. 216, pp. 398-410, 1968.

[25] A. V. Zayats and Smolyaninov, II, "Near-field photonics: surface plasmon polaritons and localized surface plasmons," *Journal of Optics a-Pure and Applied Optics*, vol. 5, pp. S16-S50, 2003.

[26] U. Schro¨ter and D. Heitmann, "Surface-plasmon-enhanced transmission through metallic gratings," *PHYSICAL REVIEW B*, vol. 58, pp. 15419-15421, 1998.

[27] D. R. H. Craig F. Bohren, "Absorption and Scattering of Light by Small Particles," *WILEY-VCH*, 1998.

[28] R. H. Ritchie, "Plasma Losses by Fast Electrons in Thin Films," *Physical Review*, vol. 106, pp. 874-881, 1957.

[29] J. R. Cole, N. A. Mirin, M. W. Knight, G. P. Goodrich, and N. J. Halas, "Photothermal Efficiencies of Nanoshells and Nanorods for Clinical Therapeutic Applications," *Journal of Physical Chemistry C*, vol. 113, pp. 12090-12094, 2009.

[30] H. R. Stuart and D. G. Hall, "Island size effects in nanoparticle-enhanced photodetectors," *Applied Physics Letters*, vol. 73, pp. 3815-3817, 1998.

[31] Max Born and E. Wolf, *Principles of Optics: Electromagnetic Theory of Propagation, Interference, and Diffraction of Light*, vol. 7th (expanded) edition, Cambridge, 1999.

[32] T. Okamoto and I. Yamaguchi, "Optical absorption study of the surface plasmon resonance in gold nanoparticles immobilized onto a gold substrate by self-assembly technique," *Journal of Physical Chemistry B*, vol. 107, pp. 10321-10324, 2003.

[33] F. Le, N. Z. Lwin, J. M. Steele, M. Kall, N. J. Halas, and P. Nordlander, "Plasmons in the metallic nanoparticle - Film system as a tunable impurity problem," *Nano Letters*, vol. 5, pp. 2009-2013, 2005.

[34] S.-H. Guo, Tim Corrigan, Henryk Szmacinski, and R. Phaneuf, "Enhanced Fluorescence from Ag nanoRods: Is Particle Plasmon Resonance Alone Responsible?," 2006 (in processing).

[35] J. Frank, "Elementary processes of photochemical reactions," *Transactions of the Faraday Society*, vol. 21, pp. 536-542, 1926.

[36] Yongxia Zhang, Kadir Aslan, Michael J. R. Previte, and C. D. Geddes, "Metal-enhanced fluorescence: Surface plasmons can radiate a fluorophore's structured emission," *Applied Physics Letters*, vol. 90, pp. 053107, 2007.

[37] Joseph R. Lakowicza, Yibing Shena, Sabato D'Auriaa, Joanna Malickaa, Jiyu Fangb, Zygmunt Gryczynskia, and I. Gryczynskia, "Radiative Decay Engineering 2. Effects of Silver Island Films on Fluorescence Intensity, Lifetimes, and Resonance Energy Transfer," *Analytical Biochemistry*, vol. 301, pp. 261-277, 2002.

[38] F. R. Sebastian Gerber, Ulrich Hohenester, Thomas Schlagenhaufen, Joachim R. Krenn, and Alfred Leitner, "Tailoring light emission properties of fluorophores by coupling to resonance-tuned metallic nanostructures," *Phys. Rev. B*, vol. 75, pp. 073404, 2007.

[39] "Solar Cell Efficiency Chart," *http://www.observatorynano.eu/project/document/2016/*, 2010.

[40] A. C. Mayer, S. R. Scully, B. E. Hardin, M. W. Rowell, and M. D. McGehee, "Polymer-based solar cells," *Materials Today*, vol. 10, pp. 28-33, 2007.

[41] P. W. M. Blom, V. D. Mihailetchi, L. J. A. Koster, and D. E. Markov, "Device physics of polymer : fullerene bulk heterojunction solar cells," *Advanced Materials*, vol. 19, pp. 1551-1566, 2007.

[42] Y. Kim, "Novel Organic Polymeric and Molecular Thin-Film Devices for Photonic Applications," *Ph D. Dissertation, Department of Electrical and Computer Engineering, University of Maryland, College Park*, 2006.

[43] I. G. Hill, A. Kahn, Z. G. Soos, and R. A. Pascal, "Charge-separation energy in films of pi-conjugated organic molecules," *Chemical Physics Letters*, vol. 327, pp. 181-188, 2000.

[44] S. F. Alvarado, P. F. Seidler, D. G. Lidzey, and D. D. C. Bradley, "Direct determination of the exciton binding energy of conjugated polymers using a scanning tunneling microscope," *Physical Review Letters*, vol. 81, pp. 1082-1085, 1998.

[45] R. Kersting, U. Lemmer, M. Deussen, H. J. Bakker, R. F. Mahrt, H. Kurz, V. I. Arkhipov, H. Bassler, and E. O. Gobel, "Ultrafast Field-Induced Dissociation of Excitons in Conjugated Polymers," *Physical Review Letters*, vol. 73, pp. 1440-1443, 1994.

[46] A. Huijser, T. J. Savenije, A. Shalav, and L. D. A. Siebbeles, "An experimental study on the molecular organization and exciton diffusion in a bilayer of a porphyrin and poly(3-hexylthiophene)," *Journal of Applied Physics*, vol. 104, 2008.

[47] P. E. Shaw, A. Ruseckas, and I. D. W. Samuel, "Exciton diffusion measurements in poly(3-hexylthiophene)," *Advanced Materials*, vol. 20, pp. 3516-3520, 2008.

[48] C. J. Brabec, S. E. Shaheen, C. Winder, N. S. Sariciftci, and P. Denk, "Effect of LiF/metal electrodes on the performance of plastic solar cells," *Applied Physics Letters*, vol. 80, pp. 1288-1290, 2002.

[49] H. Hoppe, N. Arnold, D. Meissner, and N. S. Sariciftci, "Modeling of optical absorption in conjugated polymer/fullerene bulk-heterojunction plastic solar cells," *Thin Solid Films*, vol. 451, pp. 589-592, 2004.

[50] C. R. McNeill, A. Abrusci, J. Zaumseil, R. Wilson, M. J. McKiernan, J. H. Burroughes, J. J. M. Halls, N. C. Greenham, and R. H. Friend, "Dual electron donor/electron acceptor character of a conjugated polymer in efficient photovoltaic diodes," *Applied Physics Letters*, vol. 90, pp. 193506, 2007.

[51] B. de Boer, A. Hadipour, M. M. Mandoc, T. van Woudenbergh, and P. W. M. Blom, "Tuning of metal work functions with self-assembled monolayers," *Advanced Materials*, vol. 17, pp. 621, 2005.

[52] J. X. Tang, Y. Q. Li, L. R. Zheng, and L. S. Hung, "Anode/organic interface modification by plasma polymerized fluorocarbon films," *Journal of Applied Physics*, vol. 95, pp. 4397-4403, 2004.

[53] L. S. Hung, L. R. Zheng, and M. G. Mason, "Anode modification in organic light-emitting diodes by low-frequency plasma polymerization of CHF3," *Applied Physics Letters*, vol. 78, pp. 673-675, 2001.

[54] C. C. Hsiao, C. H. Chang, H. H. Lu, and S. A. Chen, "Fine tuning hole injection for high-performance polyfluorene-based blue emitting device by adjusting work function of anode via deposition of CFx layer with proper

ionization potential on indium tin oxide," *Organic Electronics*, vol. 8, pp. 343-348, 2007.

[55] G. Yu, J. Gao, J. C. Hummelen, F. Wudl, and A. J. Heeger, "POLYMER PHOTOVOLTAIC CELLS - ENHANCED EFFICIENCIES VIA A NETWORK OF INTERNAL DONOR-ACCEPTOR HETEROJUNCTIONS," vol. 270, pp. 1789-1791, 1995.

[56] D. Chirvase, J. Parisi, J. C. Hummelen, and V. Dyakonov, " Influence of nanomorphology on the photovoltaic action of polymer-fullerene composites.," *Nanotechnology*, vol. 15, pp. 1317–1323, 2004.

[57] C. Hagglund, M. Zach, and B. Kasemo, "Enhanced charge carrier generation in dye sensitized solar cells by nanoparticle plasmons," *Applied Physics Letters*, vol. 92, pp. 013113, 2008.

[58] C. Hagglund, M. Zach, G. Petersson, and B. Kasemo, "Electromagnetic coupling of light into a silicon solar cell by nanodisk plasmons," *Applied Physics Letters*, vol. 92, pp. 053110, 2008.

[59] V. E. Ferry, M. A. Verschuuren, H. Li, R. E. I. Schropp, H. A. Atwater, and A. Polman, "Improved red-response in thin film a-Si:H solar cells with soft-imprinted plasmonic back reflectors," *Applied Physics Letters*, vol. 95, pp. 183503, 2009.

[60] D. Derkacs, S. H. Lim, P. Matheu, W. Mar, and E. T. Yu, "Improved performance of amorphous silicon solar cells via scattering from surface plasmon polaritons in nearby metallic nanoparticles," *Applied Physics Letters*, vol. 89, pp. 093103, 2006.

[61] K. R. Catchpole and A. Polman, "Design principles for particle plasmon enhanced solar cells," *Applied Physics Letters*, vol. 93, pp. 191113, 2008.

[62] F. J. Beck, S. Mokkapati, A. Polman, and K. R. Catchpole, "Asymmetry in photocurrent enhancement by plasmonic nanoparticle arrays located on the front or on the rear of solar cells," *Applied Physics Letters*, vol. 96, pp. 033113, 2010.

[63] K. R. Catchpole and A. Polman, "Plasmonic solar cells," *Optics Express*, vol. 16, pp. 21793-21800, 2008.

[64] S. P. Sundararajan, N. K. Grady, N. Mirin, and N. J. Halas, "Nanoparticle-induced enhancement and suppression of photocurrent in a silicon photodiode," *Nano Letters*, vol. 8, pp. 624-630, 2008.

[65] S. Pillai, K. R. Catchpole, T. Trupke, and M. A. Green, "Surface plasmon enhanced silicon solar cells," *Journal of Applied Physics*, vol. 101, pp. 093105, 2007.

[66] R. A. Pala, J. White, E. Barnard, J. Liu, and M. L. Brongersma, "Design of Plasmonic Thin-Film Solar Cells with Broadband Absorption Enhancements," *Advanced Materials*, vol. 21, pp. 3504-3509, 2009.

[67] J. H. Lee, J. H. Park, J. S. Kim, D. Y. Lee, and K. Cho, "High efficiency polymer solar cells with wet deposited plasmonic gold nanodots," *Organic Electronics*, vol. 10, pp. 416-420, 2009.

[68] S. S. Kim, S. I. Na, J. Jo, D. Y. Kim, and Y. C. Nah, "Plasmon enhanced performance of organic solar cells using electrodeposited Ag nanoparticles," *Applied Physics Letters*, vol. 93, pp. 073307, 2008.

[69] A. J. Morfa, K. L. Rowlen, T. H. Reilly, M. J. Romero, and J. van de Lagemaat, "Plasmon-enhanced solar energy conversion in organic bulk heterojunction photovoltaics," *Applied Physics Letters*, vol. 92, pp. 013504, 2008.

[70] T. H. Reilly, J. van de Lagemaat, R. C. Tenent, A. J. Morfa, and K. L. Rowlen, "Surface-plasmon enhanced transparent electrodes in organic photovoltaics," *Applied Physics Letters*, vol. 92, pp. 243304, 2008.

[71] W. J. Yoon, K. Y. Jung, J. W. Liu, T. Duraisamy, R. Revur, F. L. Teixeira, S. Sengupta, and P. R. Berger, "Plasmon-enhanced optical absorption and photocurrent in organic bulk heterojunction photovoltaic devices using self-assembled layer of silver nanoparticles," *Solar Energy Materials and Solar Cells*, vol. 94, pp. 128-132, 2010.

[72] B. P. Rand, P. Peumans, and S. R. Forrest, "Long-range absorption enhancement in organic tandem thin-film solar cells containing silver nanoclusters," *Journal of Applied Physics*, vol. 96, pp. 7519-7526, 2004.

[73] M. Westphalen, U. Kreibig, J. Rostalski, H. Luth, and D. Meissner, "Metal cluster enhanced organic solar cells," *Solar Energy Materials and Solar Cells*, vol. 61, pp. 97-105, 2000.

[74] D. Duche, P. Torchio, L. Escoubas, F. Monestier, J. J. Simon, F. Flory, and G. Mathian, "Improving light absorption in organic solar cells by plasmonic contribution," *Solar Energy Materials and Solar Cells*, vol. 93, pp. 1377-1382, 2009.

[75] S. W. Tong, C. F. Zhang, C. Y. Jiang, G. Liu, Q. D. Ling, E. T. Kang, D. S. H. Chan, and C. X. Zhu, "Improvement in the hole collection of polymer solar cells by utilizing gold nanoparticle buffer layer," *Chemical Physics Letters*, vol. 453, pp. 73-76, 2008.

[76] A. O. Govorov, W. Zhang, T. Skeini, H. Richardson, J. Lee, and N. A. Kotov, "Gold nanoparticle ensembles as heaters and actuators: melting and collective plasmon resonances," *Nanoscale Research Letters*, vol. 1, pp. 84-90, 2006.

[77] A. O. Govorov and H. H. Richardson, "Generating heat with metal nanoparticles," *Nano Today*, vol. 2, pp. 30-38, 2007.

[78] H. H. Shen, P. Bienstman, and B. Maes, "Plasmonic absorption enhancement in organic solar cells with thin active layers," *Journal of Applied Physics*, vol. 106, pp. 073109, 2009.

[79] J. Simpson, H. D. Drew, S.-H. Guo, and R. J. Phaneuf, "Optical Properties of Ag Nano-particle Arrays: Tuning the Plasmon Resonance," *to be submitted to APL.*

[80] Bruce T. Draine and P. J. Flatau, "User Guide for the Discrete Dipole Approximation Code DDSCAT (version6.1)," 2004.

[81] E. Hao and G. C. Schatz, "Electromagnetic fields around silver nanoparticles and dimers," *Journal of Chemical Physics*, vol. 120, pp. 357-366, 2004.

[82] P. B. Johnson and R. W. Christy, "Optical-Constants of Noble-Metals," *Physical Review B*, vol. 6, pp. 4370-4379, 1972.

[83] G. M. Hale and M. R. Querry, *Applied Optics*, vol. 12, pp. 555, 1973.

[84] M. D. Malinsky, K. L. Kelly, G. C. Schatz, and R. P. Van Duyne, "Nanosphere lithography: Effect of substrate on the localized surface plasmon resonance spectrum of silver nanoparticles," *Journal of Physical Chemistry B*, vol. 105, pp. 2343-2350, 2001.

[85] H.-C. Kan, "We developed our own Fortran program to calculate the E-field distribution based on the dipole moments calcualted by the discrete dipole approximation method.."

[86] G. E. J. Jr., "Optical Functions of Silicon determined by two-channel polarization modulation ellipsometry," *Optical Materials*, vol. 1, pp. 41, 1992.

[87] D. A. Weitz, S. Garoff, J. I. Gersten, and A. Nitzan, "The Enhancement of Raman-Scattering, Resonance Raman-Scattering, and Fluorescence from Molecules Adsorbed on a Rough Silver Surface," *Journal of Chemical Physics*, vol. 78, pp. 5324-5338, 1983.

[88] A. Gadisa, W. D. Oosterbaan, K. Vandewal, J. C. Bolsee, S. Bertho, J. D'Haen, L. Lutsen, D. Vanderzande, and J. V. Manca, "Effect of Alkyl Side-Chain Length on Photovoltaic Properties of Poly(3-alkylthiophene)/PCBM Bulk Heterojunctions," *Advanced Functional Materials*, vol. 19, pp. 3300-3306, 2009.

[89] C. J. Brabec, N. S. Sariciftci, and J. C. Hummelen, "Plastic Solar Cells," *Advanced Functional Materials*, vol. 11, pp. 15-26, 2001.

[90] K. Lee, J. Y. Kim, S. H. Park, S. H. Kim, S. Cho, and A. J. Heeger, "Air-stable polymer electronic devices," *Advanced Materials*, vol. 19, pp. 2445-2449, 2007.

[91] E. Lioudakis, A. Othonos, I. Alexandrou, and Y. Hayashi, "Ultrafast carrier dynamics on conjugated poly(3-hexylthiophene)/ 6,6 -phenylC(61)-butyric acid methyl ester composites," *Applied Physics Letters*, vol. 91, pp. 111117, 2007.

[92] C. L. Haynes, A. D. McFarland, L. L. Zhao, R. P. Van Duyne, G. C. Schatz, L. Gunnarsson, J. Prikulis, B. Kasemo, and M. Kall, "Nanoparticle optics: The importance of radiative dipole coupling in two-dimensional nanoparticle arrays," *Journal of Physical Chemistry B*, vol. 107, pp. 7337-7342, 2003.

[93] R. C. Jin, Y. W. Cao, C. A. Mirkin, K. L. Kelly, G. C. Schatz, and J. G. Zheng, "Photoinduced conversion of silver nanospheres to nanoprisms," *Science*, vol. 294, pp. 1901-1903, 2001.

[94] L. L. Zhao, K. L. Kelly, and G. C. Schatz, "The extinction spectra of silver nanoparticle arrays: Influence of array structure on plasmon resonance wavelength and width," *Journal of Physical Chemistry B*, vol. 107, pp. 7343-7350, 2003.

[95] P. Schilinsky, C. Waldauf, and C. J. Brabec, "Recombination and loss analysis in polythiophene based bulk heterojunction photodetectors," *Applied Physics Letters*, vol. 81, pp. 3885-3887, 2002.

[96] I. Zudans, W. R. Heineman, and C. J. Seliskar, "In situ measurements of chemical sensor film dynamics by spectroscopic ellipsometry. Three case studies," *Thin Solid Films*, vol. 455, pp. 710-715, 2004.

[97] J. T. Rantala and A. H. O. Karkkainen, "Optical properties of spin-on deposited low temperature titanium oxide thin films," *Optics Express*, vol. 11, pp. 1406-1410, 2003.

[98] D. Y. Smith, E. Shiles, and M. Inokuti, "Handbook of Optical Constants of Solids," *Handbook of Optical Constants of Solids*, vol. E. D. Palik, Editor, Academic Press, pp. 369-406, 1985.

[99] A. Neureuther, *TEMPEST FDTD software developed by Univ. of California at Berkeley*.

[100] A. Taflove, "Application of the Finite-Difference Time-Domain Method to Sinusoidal Steady-State Electromagnetic-Penetration Problems," *Electromagnetic Compatibility, IEEE Transactions on*, vol. EMC-22, pp. 191-202, 1980.

[101] K. S. Yee, "Numerical solutions of initial boundary value problems involving Maxwell's equations in isotropic media," *IEEE Transactions on Antennas and Propagation*, vol. AP-14, pp. 302-307, 1966.

[102] Y. Kim, M. Ballarotto, D. Park, M. Du, W. Cao, C. H. Lee, W. N. Herman, and D. B. Romero, "Interface effects on the external quantum efficiency of organic bulk heterojunction photodetectors," *Applied Physics Letters*, vol. 91, pp. 193510, 2007.

[103] P. B. Johnson and R. W. Christy, "Optical-Constants of Transition-Metals - Ti, V, Cr, Mn, Fe, Co, Ni, and Pd," *Physical Review B*, vol. 9, pp. 5056-5070, 1974.

[104] K. J. K. Koerkamp, S. Enoch, F. B. Segerink, N. F. van Hulst, and L. Kuipers, "Strong influence of hole shape on extraordinary transmission through periodic arrays of subwavelength holes," *Physical Review Letters*, vol. 92, pp. 183901, 2004.

[105] H. Hoppe, S. Shokhovets, and G. Gobsch, "Inverse relation between photocurrent and absorption layer thickness in polymer solar cells," *Physica Status Solidi-Rapid Research Letters*, vol. 1, pp. R40-R42, 2007.

[106] J. Piris, T. E. Dykstra, A. A. Bakulin, P. H. M. van Loosdrecht, W. Knulst, M. T. Trinh, J. M. Schins, and L. D. A. Siebbeles, "Photogeneration and Ultrafast Dynamics of Excitons and Charges in P3HT/PCBM Blends," *Journal of Physical Chemistry C*, vol. 113, pp. 14500-14506, 2009.

[107] J. D. Jackson, "Classical Electrodynamics Third Edition," *John Wiley & Sons, Inc*, vol. 3rd ed., 1999.

[108] http://www.lightscattering.de/MieCalc/eindex.html.

[109] L. A. A. Pettersson, S. Ghosh, and O. Inganas, "Optical anisotropy in thin films of poly(3,4-ethylenedioxythiophene)-poly(4-styrenesulfonate)," *Organic Electronics*, vol. 3, pp. 143-148, 2002.

[110] G. Ghosh, "Dispersion-equation coefficients for the refractive index and birefringence of calcite and quartz crystals," *Optics Communications*, vol. 163, pp. 95-102, 1999.

[111] S. D'Agostino, P. P. Pompa, R. Chiuri, R. J. Phaneuf, D. G. Britti, R. Rinaldi, R. Cingolani, and F. Della Sala, "Enhanced fluorescence by metal

nanospheres on metal substrates," *Optics Letters*, vol. 34, pp. 2381-2383, 2009.

[112] C. Noguez, "Surface plasmons on metal nanoparticles: The influence of shape and physical environment," *Journal of Physical Chemistry C*, vol. 111, pp. 3806-3819, 2007.

[113] A. Taflove and S.C.Hagness, *Computational Electrodynamics: The Finite-Difference Time-Domain Method, Artech House, Boston-London*, 2000.

[114] J. Adhidjaja and G. Horhmann, *A Finite-Difference Algorithm for the Transient Electromagnetic Response of a Three-Dimensional Body. Geophysics J. Int.*, vol. 98, pp. 233-242, 1989.

[115] M. J. Piketmay, A. Taflove, and J. B. Troy, "Electrodynamics of Visible-Light Interactions with the Vertebrate Retinal Rod," *Optics Letters*, vol. 18, pp. 568-570, 1993.

[116] K. B. Crozier, A. Sundaramurthy, G. S. Kino, and C. F. Quate, "Optical antennas: Resonators for local field enhancement," *Journal of Applied Physics*, vol. 94, pp. 4632-4642, 2003.

[117] M. Sadiku, *Numerical Techniques in Electromagnetics, CRC Press*, 1992.

[118] E. Rencs and S.-H. Guo, *unpublished*, 2003.

[119] Gill Barequet, M. T. Dickerson, and M.T. Goodrich, *Voronoi diagrams for polygon-offset distance functions, Springer/Heidelberg,*, vol. 1272, 1997.

[120] D. Lavender, A. Bowyer, J. Davenport, A. Wallis, and J. Woodwark, "Voronoi Diagrams of Set-Theoretic Solid Models," *Ieee Computer Graphics and Applications*, vol. 12, pp. 69-77, 1992.

[121] E. Hecht, *Optics, Addison Wesley*, vol. 3th Edition, pp. 443, 1998.

[122] *The manual of VASE, J. A. Woollam Co., Inc.*

[123] A. D. Rakic, A. B. Djurisic, J. M. Elazar, and M. L. Majewski, "Optical properties of metallic films for vertical-cavity optoelectronic devices," *Applied Optics*, vol. 37, pp. 5271-5283, 1998.